

FUNDAMENTAL INVESTIGATION OF THE TRIBOLOGICAL AND MECHANICAL  
RESPONSES OF MATERIALS AND NANOSTRUCTURES

By

ERIC W. BUCHOLZ

A DISSERTATION PRESENTED TO THE GRADUATE SCHOOL  
OF THE UNIVERSITY OF FLORIDA IN PARTIAL FULFILLMENT  
OF THE REQUIREMENTS FOR THE DEGREE OF  
DOCTOR OF PHILOSOPHY

UNIVERSITY OF FLORIDA

2012

© 2012 Eric W. Bucholz

To my family and my fiancée with whom all things are possible

## ACKNOWLEDGMENTS

First and foremost, I would like to offer my sincerest appreciation to my advisor, Prof. Susan B. Sinnott, for welcoming me into her research group and introducing me to the fascinating world of computational materials science. Through her kindness and patience throughout my doctoral studies, I have been able to overcome numerous obstacles along the way to accomplishing my research goals. Also, I thank each member of my supervisory committee for offering their time and support. I have been blessed with a unique opportunity to have Prof. Simon R. Phillpot as a continual collaborator throughout my studies acting as a secondary advisor whenever this was needed. A special thanks to Prof. Scott S. Perry for acting as my experimental advisor offering advice and criticisms and providing me the opportunity to participate in his research group. I thank Prof. W. Gregory Sawyer for his helpful conversations and for exemplifying what it means to be a scientific researcher. My gratitude is also given to Prof. Youping Chen for her willingness to offer her time in serving on my supervisory committee.

I also thank each member of the Computational Materials Science Focus Group, both past and present, for all of the support they have given to me over the past five years. In particular, I am thankful to Drs. Peter Barry, Patrick Chiu, Tao Liang, Tsu-Ray Shan, Aleksandr Chernatynskiy, Travis Kemper, and Xueying Zhao for the numerous scientific discussions which were imperative in molding my research. I thank Drs. Krishna Rajan and Chang Sun Kong from Iowa State University for providing their expertise in statistical methodologies during our collaboration. Also, I thank Drs. Jean-Michel Martin and Lucile Joly-Pottuz from École Centrale de Lyon and INSA in Lyon, France, for granting me access to their laboratories and providing their collaborations.

I am especially grateful to my family for all of their love and guidance. My parents have provided invaluable support and unwavering belief in me throughout my studies, for which I am forever indebted. It is impossible to offer sufficient gratitude to my sister, Tracy, who has served as one of the most significant influences on my life and has always offered a helping hand during the most difficult of times. And finally, I am most thankful to my fiancée, Christy, for standing by my side and maintaining my sanity throughout my doctoral studies. Without her support, I would certainly be lost.

## TABLE OF CONTENTS

	<u>page</u>
ACKNOWLEDGMENTS.....	4
LIST OF TABLES.....	9
LIST OF FIGURES.....	10
ABSTRACT .....	13
CHAPTER	
1 INTRODUCTION TO TRIBOLOGY.....	15
Solid Lubrication .....	16
Liquid Lubrication and Nanoparticle Additives .....	19
Atomic Level Simulation and Experiment.....	21
Objectives and Direction .....	22
2 METHODOLOGY .....	25
Molecular Dynamics Simulations .....	25
Reactive Empirical Bond Order Potential .....	25
Tersoff-type Mo-S Potential.....	27
Lennard-Jones Potential.....	29
Predictor-Corrector Algorithm.....	30
Temperature Control .....	31
Langevin thermostat .....	32
Velocity rescaling .....	32
Periodic Boundary Conditions .....	33
Statistical Analysis of Forces for Determining Friction Coefficient.....	33
Atomic Force Microscopy Experiments.....	35
Measuring Tip/Sample Interactions .....	36
Calibration of AFM tips .....	37
Materials Informatics and Data Mining.....	37
Principle Component Analysis.....	38
Recursive Partitioning (Regression Tree).....	39
Variable Evaluation .....	40
3 TRIBOLOGICAL PROPERTIES AND LUBRICATION MECHANISMS OF CARBON NANO-ONIONS.....	44
Computational Details.....	46
Mechanical Response during Compression.....	48
Tribological Properties of Carbon Nano-onions .....	49
Formation of Interfacial Bonds during Friction .....	49

	Relationship between Interfacial Bonds and Measured Forces.....	50
	Discussion of Rolling and Sliding Behavior .....	52
	Relative Influence of Rolling and Sliding on Coefficient of Friction.....	54
	Summary .....	55
4	MECHANICAL AND TRIBOLOGICAL RESPONSES OF AMORPHOUS CARBON NANOPARTICLES .....	65
	Experimental Motivation.....	68
	Computational Details.....	69
	Mechanical Response during Compression.....	71
	Nanocompression Simulations .....	71
	Mechanisms in Elastic to Plastic Transition.....	72
	Tribological Properties .....	75
	Summary .....	77
5	STRUCTURAL INFLUENCE ON LUBRICATION MECHANISMS OF FULLERENE-LIKE MOLYBDENUM DISULFIDE NANOPARTICLES .....	90
	Computational Details.....	92
	Nanocompression Simulations .....	93
	Frictional Properties.....	96
	Rolling Behavior .....	97
	Comparison of Friction Coefficients.....	99
	Summary .....	99
6	EFFECT OF EDGES ON TRIBOLOGICAL PROPERTIES OF LAMELLAR MOLYBDENUM DISULFIDE AT CRYOGENIC AND ELEVATED TEMPERATURES .....	107
	Computational Details.....	108
	Predicted Tribological Properties .....	109
	Summary .....	111
7	MECHANICAL BEHAVIOR OF MOLYBDENUM DISULFIDE NANOTUBES UNDER COMPRESSION, TENSION, AND TORSION .....	116
	Inorganic Nanotubes.....	118
	Computational Details.....	118
	Compressive and Tensile Loading.....	120
	Young's Modulus.....	120
	Compressive Buckling Analysis.....	122
	Torsional Loading .....	125
	Torsional Shear Modulus.....	125
	Relationships between Length, Diameter, and Torsional Stiffness.....	126
	Torsional Buckling Analysis.....	127
	Summary .....	130

8	ATOMIC-SCALE FRICTION AND WEAR OF PYROPHYLLITE .....	142
	Experimental Details .....	144
	Surface Characterization .....	146
	Friction and Wear Analysis .....	147
	Atomic-Scale Friction .....	147
	Threshold for Interfacial Wear .....	149
	Discussion .....	150
	Summary .....	152
9	DATA-DRIVEN MODEL FOR ESTIMATION OF FRICTION COEFFICIENT .....	158
	Experimental Details .....	160
	Microtribometry .....	160
	Samples and Preparation .....	161
	Data Compilation .....	161
	Development of Predictive Model .....	163
	Principal Component Analysis .....	163
	Analysis of Variable Importance .....	165
	Recursive Partitioning .....	166
	Discussion of Predictive Model .....	167
	Summary .....	169
10	GENERAL CONCLUSIONS .....	179
	LIST OF REFERENCES .....	186
	BIOGRAPHICAL SKETCH .....	204

## LIST OF TABLES

<u>Table</u>		<u>page</u>
2-1	Lennard-Jones parameters for each element type included in the MD simulations discussed in this work.....	42
4-1	Composition and properties of amorphous carbon nanoparticles.....	80
6-1	Calculated friction coefficients from tribological simulations of lamellar MoS <sub>2</sub> systems at temperatures from 5 to 500 K.....	112
7-1	Calculated Young's moduli (in GPa) from compression simulations.....	132
7-2	Calculated Young's moduli (in GPa) from tension simulations .....	132
7-3	Calculated torsional shear moduli (in GPa) from torsion simulations.....	132
9-1	List of 24 minerals and their forms used in tribometer experiments.....	170
9-2	Material dataset with 16 properties and 38 materials used to develop predictive model for friction coefficient.....	171

## LIST OF FIGURES

<u>Figure</u>	<u>page</u>
2-1	Schematic representation of two-dimensional periodic boundary conditions illustrating the central primary supercell and the surrounding periodic images... 43
3-1	Snapshot of tribological system with four COs between DLC surfaces indicating regions of rigid and moving, fixed, thermostat, and active atoms ..... 57
3-2	Comparison of normal forces and percentage of fourfold coordination for COs and D-COs during uniaxial compression simulations ..... 58
3-3	Snapshots of COs simulations at different sliding distances, $d$ , during friction at apparent contact pressures of 1 and 5 GPa ..... 59
3-4	Snapshot of COs simulation with four nano-onions indicating strong interfacial bonding during sliding at 5 GPa contact pressure ..... 60
3-5	Frictional and normal forces for single CO sliding at 5 GPa compression with snapshots at various stages of simulation ..... 61
3-6	Frictional and normal forces during friction simulations with four COs at contact pressures of 1 GPa and 5 GPa ..... 62
3-7	Percentage of rolling and sliding for COs and D-COs during friction of the four nano-onion systems at 1, 2.5, and 5 GPa contact pressures ..... 63
3-8	Load ramp for MD simulations with four nano-onions illustrating friction coefficients for rolling and sliding behavior ..... 64
4-1	HRTEM images of ~150 nm diameter a-C nanoparticles during and after <i>in situ</i> compression experiments with elastic and plastic deformation..... 81
4-2	Snapshot of initial system showing 5 nm diameter and 0 at.% H a-C nanoparticle between H-terminated (111) diamond substrates ..... 82
4-3	Schematic of a-C nanoparticle compression illustrating definition of real contact radius, $r_c$ , and change in diameter, $d$ ..... 83
4-4	Evolution of compressive force and approximate contact stress as a function of percentage strain during nanoparticle compression ..... 84
4-5	Snapshot of strong interfacial bond formations during unloading of 3 nm diameter a-C nanoparticle with 0 at.% H from a maximum strain of ~37%..... 85
4-6	Final strain after nanoparticle relaxation and percentage of carbon atoms forming new C-C bonds as a function of strain during compression..... 86

4-7	Cross-sectional snapshots of compressed 4 nm diameter nanoparticles with 0, 25, and 50 at.% H indicating C atoms which formed new C-C bonds.....	87
4-8	Frictional and normal forces during friction simulations for 2 and 4 nm diameter a-C nanoparticles with 0, 25, and 50 at.% H.....	88
4-9	Load ramps from friction simulations for a-C nanoparticles with diameters of 2 and 4 nm.....	89
5-1	Snapshots of nested three layer IF-MoS <sub>2</sub> nanoparticles with ellipsoidal and nano-octahedral configurations .....	101
5-2	Evolution of contact pressure during compression of MoS <sub>2</sub> nano-octahedron with cross-sectional snapshots at various stages of simulation .....	102
5-3	Snapshot of rupture at facet edge of IF-MoS <sub>2</sub> nano-octahedron during compression .....	102
5-4	Evolution of contact pressure during compression of MoS <sub>2</sub> ellipsoid oriented on minor axis with cross-sectional snapshots at various stages of simulation..	103
5-5	Evolution of contact pressure during compression of MoS <sub>2</sub> ellipsoid oriented on major axis with cross-sectional snapshots at various stages of simulation..	103
5-6	Graphs of frictional and normal forces for ellipsoidal nanoparticle oriented along minor and major axes and nano-octahedron .....	104
5-7	Analysis of rolling behavior during friction of ellipsoidal nanoparticle oriented along major axis at an average normal force of 21.4 nN .....	105
5-8	Average angular and lateral displacements between slip events during friction of ellipsoidal nanoparticle oriented along major axis.....	106
5-9	Friction load ramps for IF-MoS <sub>2</sub> systems.....	106
6-1	Snapshots of initial MoS <sub>2</sub> systems with a 2-D periodic sheet and 1-D periodic ribbons between sulfur-terminated (110) BCC Mo substrates .....	113
6-2	Frictional and normal forces of lamellar MoS <sub>2</sub> systems as a function of sliding distance at temperatures of 5, 300, and 500 K.....	114
6-3	Friction load ramps from tribological simulations of lamellar MoS <sub>2</sub> systems at temperatures of 5 to 500 K .....	115
7-1	Hexagonal MoS <sub>2</sub> lattice indicating the a <sub>1</sub> and a <sub>2</sub> unit vectors and the directions for wrapping of armchair and zigzag nanotubes.....	133
7-2	Initial structure of 10 nm (27,27) SWINT showing regions of rigid and moving, thermostat, and active atoms for MD simulations.....	133

7-3	Stress versus strain during compression of armchair and zigzag SWINTS and DWINTS .....	134
7-4	Snapshots of compressed (27,27) armchair SWINTs after buckling at 0.08 strain with initial lengths of 10, 20, and 30 nm .....	135
7-5	Snapshots of compressed (71,0) zigzag SWINTs after buckling at 0.08 strain with initial lengths of 10, 20, and 30 nm.....	136
7-6	Comparison of critical stress and strain at the buckling point during compression of armchair and zigzag INTs .....	137
7-7	Torsional moment versus torsional angle of armchair and zigzag SWINTS and DWINTS during applied torsion .....	138
7-8	Relationship between torsional stiffness and diameter for armchair and zigzag INTs.....	139
7-9	Snapshots of INTs after torsional buckling .....	140
7-10	Critical buckling moment relative to the length and diameter of armchair and zigzag INTs.....	141
8-1	Schematic representation of the crystal structure for the aluminosilicate mineral pyrophyllite.....	153
8-2	XRD analysis of a cleaved pyrophyllite flake .....	154
8-3	3-D topographical AFM image of pyrophyllite illustrating the step-terrace nature of the surface observed on the nanometer scale.....	155
8-4	Topographical step height analysis for individual steps across the pyrophyllite surface.....	155
8-5	Friction load ramps and interfacial shear stresses for the sliding contact between a Si <sub>3</sub> N <sub>4</sub> probe tip and pyrophyllite and HOPG basal planes .....	156
8-6	AFM images of atomic-scale wearing of the pyrophyllite surface .....	157
9-1	Principal component analysis scores plot and loadings plot for PC1 versus PC2. ....	175
9-2	Variable importance and sum of squares analyses used to determine parameters to include in recursive partitioning .....	176
9-3	Dendrogram for estimation of friction coefficient from recursive partitioning ....	177
9-4	Predicted versus experimental friction coefficient from recursive partitioning...	178

Abstract of Dissertation Presented to the Graduate School  
of the University of Florida in Partial Fulfillment of the  
Requirements for the Degree of Doctor of Philosophy

FUNDAMENTAL INVESTIGATION OF THE TRIBOLOGICAL AND MECHANICAL  
RESPONSES OF MATERIALS AND NANOSTRUCTURES

By

Eric W. Bucholz

August 2012

Chair: Susan B. Sinnott

Major: Materials Science and Engineering

In the field of tribology, the ability to predict, and ultimately control, frictional performance is of critical importance for the optimization of tribological systems. As such, understanding the specific mechanisms involved in the lubrication processes for different materials is a fundamental step in tribological system design. In this work, a combination of computational and experimental methods that include classical molecular dynamics (MD) simulations, atomic force microscopy (AFM) experiments, and multivariate statistical analyses provides fundamental insight into the tribological and mechanical properties of carbon-based and inorganic nanostructures, lamellar materials, and inorganic ceramic compounds.

One class of materials of modern interest for tribological applications is nanoparticles, which can be employed either as solid lubricating films or as lubricant additives. In experimental systems, however, it is often challenging to attain the *in situ* observation of tribological interfaces necessary to identify the atomic-level mechanisms involved during lubrication and response to mechanical deformation. Here, classical MD simulations establish the mechanisms occurring during the friction and compression of several types of nanoparticles including carbon nano-onions, amorphous carbon

nanoparticles, and inorganic fullerene-like MoS<sub>2</sub> nanoparticles. Specifically, the effect of a nanoparticle's structural properties on the lubrication mechanisms of rolling, sliding, and lamellar exfoliation is indicated; the findings quantify the relative impact of each mechanism on the tribological and mechanical properties of these nanoparticles.

Beyond identifying the lubrication mechanisms of known lubricating materials, the continual advancement of modern technology necessitates the identification of new candidate materials for use in tribological applications. To this effect, atomic-scale AFM friction experiments on the aluminosilicate mineral pyrophyllite demonstrate that pyrophyllite provides a low friction coefficient and low shear stresses as well as a high threshold to interfacial wear; this suggests the potential for use of pyrophyllite as a lubricious material under specific conditions. Also, a robust and accurate model for estimating the friction coefficients of inorganic ceramic materials that is based on the fundamental relationships between material properties is presented, which was developed using multivariate data mining algorithms. These findings provide the tribological community with a new means of quickly identifying candidate materials that may provide specific frictional properties for desired applications.

## CHAPTER 1 INTRODUCTION TO TRIBOLOGY

Derived from the Greek word τριβος, or tribos, meaning “rubbing,” tribology is defined as “the science and technology of interacting surfaces in relative motion and of related subjects and practices” [1]. Involving rubbing surfaces, the field of tribology includes a wide range of disciplines such as lubrication, adhesion, friction, and wear of interfaces in mechanical systems [2]. During the 1960s, an increase in the number of reported failures resulting from friction and wear related issues made it evident that measures needed to be taken to counteract the financial toll caused by these problems [3]. In response to this economic impact, the term tribology was first introduced in 1966 in what is often referred to as *The Jost Report* [4] as a means of encompassing the interdisciplinary nature of tribology and the breadth of topics involved with interacting surfaces. To expand on this notion, the complexity of tribological interfaces merits knowledge in numerous disciplines including, but not limited to, physics, chemistry, solid and fluid mechanics, thermodynamics, heat transfer, materials science, lubrication, and machine design [1].

From an economic perspective, estimates have indicated that inadequate application of the sciences involved in tribology led to losses in the United States on the order of around \$200 billion in 1985 with three-quarters of that total resulting from wear [5]. Additionally, it has been suggested that friction in mechanical systems accounts for approximately one-third of the world’s total energy consumption [1]. From these significant financial losses, it is reasonable to assume that proper attention to tribology would result in large economic savings. One estimate by Jost [6] suggested that tribological research efforts could potentially lead to economic savings of 1.3 to

1.6% of the gross national product. Other estimates in the 1970s for possible financial savings in the United States ranged from \$16 billion to over \$40 billion per year [7, 8].

Since the industrial revolution, industrialized countries around the world have become dependent on technological advances requiring improved handling of tribological applications. This is particularly noteworthy for technologies that include a wide array of mechanical systems under a variety of environmental conditions. Some of these technologies include the automotive industry, manufacturing systems, and aerospace vehicles, each of which requires the specific selection and application of materials or fluids in order to obtain desirable performance. As such, through tribological research, the contributions to continued technological advancement include, for example, improved system lifetime, increased friction reduction leading to a decrease in energy consumption, and improved wear resistance.

### **Solid Lubrication**

A solid lubricant can be thought of as any material that gives wear and friction reduction at interfaces in relative motion [2]. Typically, a solid lubricant is used in applications where a liquid lubricant does not satisfy the requirements of the system. Some of the reasons why liquid lubricants are not selected for a given application include problems with applying the lubricant, sealing, weight, and environmental conditions such as high vacuum, high temperatures, cryogenic temperatures, and under radiation [2]. Appropriate solid lubricants are capable of extending the operating conditions of a mechanical system in these extreme environments. For instance, liquid lubricants are not applicable at cryogenic temperatures due to increased viscosity and at higher temperatures because they generally decompose. In addition, liquid lubricants are not suited for high vacuum applications such as occur at high altitudes and near-

earth orbits since they evaporate under these conditions; this not only makes the lubricant ineffective, but it can also potentially contaminate sensitive equipment elsewhere in the system [9].

The selection of solid lubricants for tribological applications includes a broad range of materials such as lamellar solids, amorphous carbon, nanostructures, polymers, and ceramics [10]. Lamellar solids have layered crystal structures that give rise to their increased lubricity. Structurally, they are characterized by strong covalent bonds within the layers and weaker long-range interactions between the layers. Along with this, these materials are characterized by low energies on the basal plane which allows for easy shearing and low friction forces along the basal planes at the tribological interface [11-16]. Two of the most common lamellar solids in tribological applications are graphite and the metal dichalcogenide, MoS<sub>2</sub>. Graphite provides low friction coefficients in humid air environments and has thermal stability to around 2273 K; however, in a practical sense, the temperature range for graphite is limited to about 873 K due to oxidation [10]. Limitations to the use of graphite, though, exist since the low friction behavior is reliant on the presence of adsorbed water vapors, so graphite is ineffective in dry or vacuum environments [17]. MoS<sub>2</sub>, on the contrary, is intrinsically lubricious in that the lamellar structure enables very low friction coefficients in vacuum and dry environments. In the case of MoS<sub>2</sub>, the presence of humidity contributes to a significant increase in interfacial friction and wear [12, 17, 18].

Amorphous carbon films such as diamond-like carbon (DLC) are capable of providing low wear rates, low friction coefficients, and chemical inertness in vacuum environments [19]. In practice, additional friction and wear reduction is achieved through

the partial hydrogenation of these amorphous films [20, 21]. Unlike other forms of carbon such as diamond and graphite which are characterized by an entirely  $sp^3$ - and  $sp^2$ -hybridized network, respectively, amorphous carbon films are comprised of  $sp^2$ - and  $sp^3$ -hybridized carbon atoms. The presence of the unsaturated carbon atoms near the tribological interface serves as initiation points for chemical interactions; the addition of hydrogen functions to pacify these carbon atoms limiting the interactions at the sliding interface [21, 22].

Nanostructures such as carbon nanotubes (CNTs), carbon nano-onions (COs), and inorganic fullerene-like (IFs) nanoparticles have closed-shell structures which provide additional structural stability and chemical inertness through the elimination of dangling bonds [23-25]. Their unique curved morphologies further give rise to interesting properties. Specifically, nanostructures can provide friction reduction through a variety of different qualitative behaviors including sliding and rolling of the nanoparticles at the interface as well as the exfoliation of lubricious sheets during friction [18, 25-28].

Polymeric materials such as polytetrafluoroethylene (PTFE) and polyethylene (PE) are also used in some tribological applications. PTFE is one of the most widely used polymers in aerospace applications [9, 29]. The inert structure of PTFE provides relatively low surface energies leading to improved tribological performance in vacuum and in humid environments. Some issues with polymers such as PTFE are low resistance to wear, low load-bearing capability, and poor thermal conductivity. As such, it is typical in aerospace applications to counter these problems through the use of polymer composites which incorporate different filler materials [29-31].

Some ceramic compounds such as  $\text{Al}_2\text{O}_3$ ,  $\text{Si}_3\text{N}_4$ ,  $\text{SiC}$ , and  $\text{ZrO}_2$  have been shown to provide friction and wear reduction under varying environmental conditions [17, 32]. The appeal of these ceramic materials originates from their specific mechanical and chemical properties along with their high thermal stability. Ceramic oxides are of particular interest for high temperature applications since other material choices can deteriorate from oxidation. In addition, the tribological properties of ceramics are complex since changes in environment, such as an increase in relative humidity, can result in a decrease in friction and wear for some ceramic compounds and an increase for others [17, 32].

For the work presented in this dissertation, the materials of focus include a variety of carbon-based and inorganic nanostructures, lamellar materials, and inorganic ceramic compounds.

### **Liquid Lubrication and Nanoparticle Additives**

The application of liquid lubrication in tribological systems exists in different forms. The most desirable of these forms is fluid film lubrication [2]. In fluid film lubrication, the lubricant film is sufficiently thick to fully separate the moving interfaces; because of this, the friction coefficients obtained are minimal since the surfaces do not come into physical contact meaning that the frictional forces are only a product of the shearing of the liquid lubricant film. The type of lubrication of interest in this dissertation is boundary lubrication. Under boundary lubrication, a thick fluid film is unable to form causing the load to be fully supported by physical contact between asperities on the moving interfaces [2, 33]. In this regime, the bulk viscosity of the liquid has little to no influence on the properties with the tribological responses being dominated by frictional contact between the asperities and by interactions between the surfaces and the lubricant film

leading to increases in interfacial friction and wear [33]. In these boundary lubrication conditions, the addition of lubricant additives is common in order to help reduce friction and wear during interfacial sliding. Research involving the friction modifier molybdenum dithiocarbamate (MoDTC) indicates that this additive reduces friction coefficient through a chemical reaction process producing lubricious MoS<sub>2</sub> sheets at the asperity contacts; however, the chemical reaction also results in the production of sulfur-containing radicals that are harmful to the environment [34]. As such, the identification of non-toxic, environmentally friendly friction reducing and anti-wear additives is of interest for boundary lubrication applications.

Nanoparticles such as fullerenes and nanotubes are candidates for use as lubricant additives [35-38]. The appeal of these nanoparticles is a result of their chemical inertness due to their closed-shell structure as well as their extremely small size which permits delivery to the tribological contacts. While different nanoparticles such as CNTs and IFs are able to provide both friction and wear reduction during boundary lubrication, the mechanisms involved during the tribological process are quite different. For instance, Raman spectroscopy analyses inside the contact during friction have shown that single-wall CNTs dispersed at 1 wt.% in a synthetic polyalphaolefin (PAO) base oil undergo amorphization during the tribological tests which leads to the reduction of friction and wear [39, 40]. On the other hand, images of IF-MoS<sub>2</sub> and IF-WS<sub>2</sub> before and after friction using high resolution transmission electron microscopy, as well as *in situ* Raman spectroscopy analyses during friction, have shown that the exceptional frictional properties of the IFs dispersed in PAO under severe conditions are due to the exfoliation of individual lamellar sheets of lubricant at the friction

interface [39, 41]. Furthermore, additional experiments with IF-WS<sub>2</sub> nanoparticles have suggested that the dominant mechanism at low loads is one of rolling and sliding of the IFs during friction since the initial structure of the nanoparticles was preserved [36]. Developing an understanding and identifying the mechanisms involved for different nanoparticles within a friction contact is important for optimizing their use in tribological applications; this is the aim of portions of this dissertation discussed in Chapters 3, 4, and 5.

### **Atomic Level Simulation and Experiment**

Computational and experimental techniques are the most effective when functioning together in order to further the knowledge of what is being studied and to apply it for the optimization of future material design [42]. In terms of computational efficiency, continual advancement of computational efficiency with regard to parallel processing, communication between computing nodes, and processing speed allows for enhanced capacity to provide atomic level details on systems such as interfacial mechanisms occurring during friction. Experimentally, modern technological advances such as atomic force microscopy (AFM) [43] have enabled atomic level experiments and simulations to reach a degree of overlap that has never before been seen. For instance, the use of AFM experiments along with atomistic molecular dynamics (MD) simulations have thoroughly investigated the various mechanisms that occur at single-asperity contacts [44]. Through these single-asperity tribological studies, significant comparisons between simulation and experiment can be made leading to a more complete understanding of friction between single asperities which will hopefully one day be used to better describe and predict the behavior of complex multi-asperity interfaces. One of the predominant strengths of atomistic MD simulations is the ability to

visualize the tribological interface at the atomic level and, thus, to identify mechanisms involved during friction which are unable to be observed through experimental methods. With regard to this, recent development of *in situ* electron microscopy techniques has helped to further bridge the gap between theory and experiments. One area where these methods have been successful is through the *in situ* manipulation of isolated nanoparticles [45-48]; these experiments have provided both quantitative and qualitative analyses of the deformation and fracture behaviors observed during applied compressive and frictional forces.

### **Objectives and Direction**

The primary focus of this dissertation is to provide fundamental insight into the tribological and mechanical properties of a variety of materials including carbon-based and inorganic nanostructures, lamellar materials, and inorganic ceramic compounds. This task is accomplished through the combination of computational and experimental methods including atomistic MD simulations, AFM experiments, and multivariate statistical analyses involving materials informatics methods. Using these techniques, the key mechanisms involved in the friction and mechanics of these different materials are reported.

The remainder of this dissertation is presented as follows. Chapter 2 provides the details of the computational, experimental, and statistical methods used throughout this work. Chapter 3 discusses MD simulations involving the friction of carbon nano-onions between hydrogen-terminated DLC substrates. These simulations investigate the qualitative behaviors involved during friction of the nano-onions and how these lubrication mechanisms impact the quantitative frictional response. In Chapter 4, atomistic MD simulations are covered involving amorphous carbon nanoparticles

positioned between hydrogen-terminated diamond surfaces. These simulations investigate the mechanical and frictional response of the nanoparticles as a function of diameter, normal load, and percentage of hydrogen content. In particular, the simulations indicate the mechanisms involved in the transition from elastic to plastic deformation during compression of individual nanoparticles. Chapter 5 discusses MD simulations probing the mechanical and frictional properties of inorganic fullerene-like MoS<sub>2</sub> nanoparticles. Specifically, these simulations characterize the effects of nanoparticle structure and orientation on the observed properties. In Chapter 6, atomistic MD simulations are reviewed that include the friction of lamellar MoS<sub>2</sub> systems both with and without exposed edges. These simulations investigate the influence of edge interactions on the tribological properties of lamellar MoS<sub>2</sub> at cryogenic temperatures.

The mechanical properties of MoS<sub>2</sub> nanotubes under compressive, tensile, and torsional loads are covered in Chapter 7 as determined from atomistic MD simulations. These simulations investigate the elastic properties and buckling behavior as a function of length, diameter, and nanotube type (i.e. armchair or zigzag). In Chapter 8, atomic force microscopy experiments involving mineralogical pyrophyllite samples are discussed. These experiments investigate the atomic level friction and wear performance of pyrophyllite as compared to other minerals and commonly used solid lubricants; the results highlight the fundamental properties of pyrophyllite that indicate its potential use as a tribological material. Chapter 9 presents a data-driven model for estimating the friction coefficients of a variety of inorganic ceramic compounds that was developed using materials informatics methods. The results not only identify the

influence of fundamental intrinsic properties on the friction coefficients of this class of materials but also indicate the promise for future use of these methods for the prediction and tailoring of materials with specific tribological properties. Finally, Chapter 10 provides a general summary of the conclusions from this dissertation.

## CHAPTER 2 METHODOLOGY

### Molecular Dynamics Simulations

Using empirical interatomic potentials, molecular dynamics (MD) simulations have been used, in recent years, to accurately model the mechanical properties and tribological behavior of many different materials and nanostructures [22, 44, 49-65]. In classical MD simulations, the evolution of a system of atoms is determined through the numerical integration of Newton's equation of motion as a function of time. According to Newton's second law, the force applied on a given atom is the product of the mass and acceleration as shown by:

$$\vec{F}_i = m_i \vec{a}_i = \frac{\partial E}{\partial \vec{r}_i} \quad (2-1)$$

where  $\vec{F}_i$  is the force vector,  $m_i$  is the mass,  $\vec{a}_i$  is the acceleration,  $E$  is the potential energy, and  $\vec{r}_i$  is the position vector of atom  $i$ . Through this numerical integration of Equation 2-1, the trajectory of the atoms is calculated which determines the positions, velocities, and accelerations at future times. From this information, the average properties of the system can be solved. All MD simulations performed in this work followed a canonical, or NVT, ensemble where the number of atoms (N), volume (V), and temperature (T) were kept constant while the total energy and pressure of the systems were permitted to fluctuate with time.

### Reactive Empirical Bond Order Potential

For the simulations described in detail in Chapters 3 and 4, the short-range covalent interactions were modeled using the second-generation reactive empirical bond order (REBO) potential for hydrocarbon systems developed by Brenner *et al.* [66].

Based on the bond order potential developed by Tersoff [67, 68], the REBO potential was developed to provide improved description of the bonding environments in hydrocarbon systems with the second-generation form providing improved descriptions of bond energies, bond lengths, and force constants for carbon-carbon bonds relative to the first-generation form of the potential [69]. In the REBO potential, the general form of the total binding energy is given by:

$$E_b = \sum_i \sum_{j>i} [V^R(r_{ij}) - b_{ij}V^A(r_{ij})] \quad (2-2)$$

where  $V^R(r_{ij})$  and  $V^A(r_{ij})$  represent all pair-wise interatomic core-core/electron-electron repulsive and core-electron attractive interactions, respectively. The term  $r_{ij}$  denotes the interatomic distance between atoms  $i$  and  $j$  which is the sole basis for these functions that have analytical forms given by:

$$V^R(r_{ij}) = f_c(r_{ij}) \cdot \left(1 + \frac{Q}{r_{ij}}\right) \cdot A \cdot e^{-\alpha \cdot r_{ij}} \quad (2-3)$$

$$V^A(r_{ij}) = f_c(r_{ij}) \cdot \sum_{n=1}^3 B_n \cdot e^{-\beta_n \cdot r_{ij}} \quad (2-4)$$

where  $A$ ,  $B$ ,  $Q$ ,  $\alpha$ , and  $\beta$  are two-body fitting parameters that are specific to a given type of atomic interaction. The term  $f_c(r_{ij})$  is a cutoff function that limits the radial distance for covalent interactions to only include nearest neighbors.

The bond order function,  $b_{ij}$ , in Equation 2-2 is a many-body term that represents the effect of an atom's local environment such as coordination number, bond angles, torsion angles, and conjugation on binding energy. The form of this function is given by:

$$b_{ij} = \frac{1}{2} [b_{ij}^{\sigma-\pi} + b_{ji}^{\sigma-\pi}] + b_{ij}^{\pi} \quad (2-5)$$

where  $b_{ij}^{\sigma-\pi}$  and  $b_{ji}^{\sigma-\pi}$  are determined by the local coordination and bond angles for atoms  $i$  and  $j$ , respectively. These functions are described as:

$$b_{ij}^{\sigma-\pi} = \left[ 1 + \sum_{k \neq i, j} f_c(r_{ik}) \cdot G(\cos(\theta_{ijk})) \cdot e^{\lambda_{ijk}} + P_{ij}(N_i^C, N_i^H) \right]^{-1/2} \quad (2-6)$$

where  $G(\cos(\theta_{ijk}))$  is a polynomial function that describes the contribution of the bond angle between atoms  $i$ ,  $j$ , and  $k$  on the bond order. The parameter  $\lambda_{ijk}$  is included in order to yield smooth potential energy surfaces for the three-body exchange reactions among hydrogen atoms. The term  $P_{ij}$  describes the local chemistry about atom  $i$  where  $N_i^C$  and  $N_i^H$  are the number of neighboring carbon and hydrogen atoms, respectively.

The function  $b_{ij}^{\pi}$  in Equation 2-5 is a sum of two terms and is given by:

$$b_{ij}^{\pi} = \Pi_{ij}^{RC} + \Pi_{ij}^{DH} \quad (2-7)$$

where  $\Pi_{ij}^{RC}$  is determined based on whether a bond between atoms  $i$  and  $j$  is radical in character or is part of a conjugated system, and  $\Pi_{ij}^{DH}$  is determined based on the dihedral angle for carbon-carbon double bonds.

### **Tersoff-type Mo-S Potential**

For the simulations discussed in Chapters 5, 6, and 7, the short-range covalent interactions were calculated using a Tersoff-type many body interatomic potential parameterized by Liang *et al.* for Mo-S systems [70]. This Mo-S potential is based on the same model as the second-generation REBO potential discussed previously [66]. Although the Mo-S potential was designed with principle interest in the structure and properties of MoS<sub>2</sub>, it has been shown to provide suitable agreement with the structure

and energetics of small Mo and S molecules and three-dimensional Mo crystals as well as binary Mo-S crystals. Since the Mo-S potential is based on the hydrocarbon REBO potential, many of the formalisms, as expected, are the same or similar between the two versions of this potential. The general form of the binding energy is the same as that of hydrocarbon REBO provided in Equation 2-2. Similarly, the function for the pair-wise interatomic repulsion is the same as in Equation 2-3.

Notable differences between the Mo-S and hydrocarbon REBO potentials begin with the expression for the pair-wise interatomic attraction which, for the Mo-S potential, is the same as for the original Tersoff bond order potential [67, 68]. The attractive term is simplified from the hydrocarbon REBO potential since it does not include the sum of exponentials shown in Equation 2-4; for Mo-S systems this term is given by:

$$V^A(r_{ij}) = f_c(r_{ij}) \cdot B \cdot e^{-\beta \cdot r_{ij}} \quad (2-8)$$

where  $r_{ij}$  is the interatomic distance between atoms  $i$  and  $j$ ,  $B$  and  $\beta$  are pair-wise fitting parameters, and  $f_c(r_{ij})$  is a radial cutoff function. The bond order function is made up of only two many-body terms, the bond angle term  $G$  and the coordination term  $P$ , and is expressed as:

$$b_{ij} = \left[ 1 + \sum_{k \neq i, j} f_c(r_{ik}) \cdot G(\cos(\theta_{ijk})) + P(N_i) \right]^{-1/2} \quad (2-9)$$

where  $\theta_{ijk}$  is the angle between atoms  $i$ ,  $j$ , and  $k$ . The term  $N_i$  is given as:

$$N_i = N_i^{Mo} + N_i^S \quad (2-10)$$

where  $N_i^{Mo}$  and  $N_i^S$  are the number of Mo and S neighbors for atom  $i$ , respectively.

## Lennard-Jones Potential

For each of the simulations performed in this work, a Lennard-Jones (LJ) 12-6 potential [71] was used to model the long-range van der Waals (vdW) interactions between atoms. The form of this potential is given as:

$$V^{vdW}(r_{ij}) = 4\varepsilon \left[ \left( \frac{\sigma}{r_{ij}} \right)^{12} - \left( \frac{\sigma}{r_{ij}} \right)^6 \right] \quad (2-11)$$

where  $V^{vdW}(r_{ij})$  is the cohesive energy, and  $r_{ij}$  is the interatomic distance between atoms  $i$  and  $j$ . The terms  $\sigma$  and  $\varepsilon$  are the LJ parameters for specific atom types that represent the radial distance at which the potential energy function is zero and the depth of the potential well, respectively. In the LJ 12-6 potential, the term  $r^{-12}$  relates to the short-range electrostatic repulsion where a rapid increase in energy occurs as electron clouds overlap, a phenomenon attributed to the Pauli Exclusion Principle. The term  $r^{-6}$  corresponds to the long-range attraction that results from vdW dipole-dipole interactions.

To reflect the interactions between different elemental types, the Lorentz-Berthelot mixing rules [71] were used to calculate the LJ parameters for these interactions. As such, if  $\sigma_{XX}$  and  $\varepsilon_{XX}$  represent the LJ parameters for atom type  $X$ , then the parameters for interactions between atom types  $X$  and  $Y$  are determined by:

$$\sigma_{XY} = \frac{1}{2}(\sigma_{XX} + \sigma_{YY}) \quad (2-12)$$

$$\varepsilon_{XY} = \sqrt{\varepsilon_{XX} \cdot \varepsilon_{YY}} \quad (2-13)$$

The different LJ parameters used for the elemental types included in these MD simulations are provided in Table 2-1.

## Predictor-Corrector Algorithm

For the MD simulations in this work, the evolution of the systems with time was controlled by a third order Nordsieck-Gear predictor-corrector algorithm [71]. If the initial atom positions, velocities, accelerations, and higher order derivatives of position are known at time  $t$ , the predictor-corrector algorithm allows for the estimation of these values at time  $t + \Delta t$  with reasonable accuracy by a Taylor expansion about time  $t$  under conditions of continuous trajectory. The forms of the predictor are given as:

$$\begin{aligned}\vec{r}^p(t + \Delta t) &= \vec{r}(t) + \vec{v}(t) \cdot \Delta t + \frac{1}{2} \vec{a}(t) \cdot \Delta t^2 + \frac{1}{6} \vec{b}(t) \cdot \Delta t^3 \\ \vec{v}^p(t + \Delta t) &= \vec{v}(t) + \vec{a}(t) \cdot \Delta t + \frac{1}{2} \vec{b}(t) \cdot \Delta t^2 \\ \vec{a}^p(t + \Delta t) &= \vec{a}(t) + \vec{b}(t) \cdot \Delta t \\ \vec{b}^p(t + \Delta t) &= \vec{b}(t)\end{aligned}\tag{2-14}$$

where  $\vec{r}^p$ ,  $\vec{v}^p$ ,  $\vec{a}^p$ , and  $\vec{b}^p$  are the predicted position, velocity, acceleration, and third derivative of position, respectively, of each atom with respect to time.

Next, the interatomic forces at time  $t + \Delta t$  are evaluated using the predicted positions which provide the corrected accelerations,  $\vec{a}^c(t + \Delta t)$ . The approximate size of the error from the prediction step is determined based on the difference between the corrected and predicted accelerations:

$$\Delta \vec{a}(t + \Delta t) = \vec{a}^c(t + \Delta t) - \vec{a}^p(t + \Delta t)\tag{2-15}$$

The predicted values from Equation 2-14 are now corrected using the size of the error from Equation 2-15 as given by:

$$\begin{aligned}
\vec{r}^c(t + \Delta t) &= \vec{r}^p(t + \Delta t) + \frac{1}{6} \Delta \vec{a}(t + \Delta t) \\
\vec{v}^c(t + \Delta t) &= \vec{v}^p(t + \Delta t) + \frac{5}{6} \Delta \vec{a}(t + \Delta t) \\
\vec{a}^c(t + \Delta t) &= \vec{a}^p(t + \Delta t) + \Delta \vec{a}(t + \Delta t) \\
\vec{b}^c(t + \Delta t) &= \vec{b}^p(t + \Delta t) + \frac{1}{3} \Delta \vec{a}(t + \Delta t)
\end{aligned}
\tag{2-16}$$

where the superscript <sup>c</sup> denotes the corrected values. Using these corrected values, the positions and derivatives for the next iteration are predicted.

The above steps in the predictor-corrector algorithm are repeated for every time step throughout the simulation. The accuracy of the predictor-corrector algorithm in determining the evolution of the system is dependent on both the size of the n<sup>th</sup> order Taylor expansion and the value of the time step  $\Delta t$ ; therefore, it is important to balance the accuracy of the calculation with the computational efficiency. For the MD simulations in this work, the Taylor expansion was truncated after the third derivate (as shown in Equation 2-14) and the time step was 0.2 fs. However, it should be noted that additional accuracy can be attained by using a smaller time step and/or by including higher order derivatives in the Taylor expansion.

### **Temperature Control**

Appropriate control of system temperature is an important aspect of MD simulations. This temperature control is typically achieved through the application of a thermostat which enables the constant temperatures that allow for the NVT ensemble in this work by dissipating the heat generated from the non-equilibrium MD simulations. Two different thermostats were utilized in this work, a Langevin thermostat and a velocity rescaling thermostat.

## Langevin thermostat

An atom to which a Langevin thermostat has been applied, rather than obeying Newton's equation of motion, follows the generalized Langevin equation of motion as given by [72]:

$$m \cdot \vec{a} = f(r) - \xi \cdot \vec{v} + f' \quad (2-17)$$

where  $m$  is the mass of the atom,  $\vec{a}$  is the atom's acceleration,  $f(r)$  is a conservative force acting on the atom,  $\xi$  is a frictional constant,  $\vec{v}$  is the velocity of the atom, and  $f'$  is a random force. The term  $\xi \cdot \vec{v}$  represents the frictional force resulting from frictional dragging between atoms and is always positive, thus removing energy and providing a decrease in system temperature. The random force is selected randomly from a Gaussian distribution to add kinetic energy to the atom. Through a balancing of the frictional force and the random force, the velocities of the thermostat atoms are adjusted to maintain the desired system temperature.

## Velocity rescaling

The velocity rescaling thermostat is a simpler temperature control method than the Langevin thermostats and is controlled by:

$$\vec{v}_{new} = \vec{v}_{old} \cdot \sqrt{\frac{T_0}{T_{ins}}} \quad (2-18)$$

where  $\vec{v}_{new}$  is the rescaled velocity of the atom,  $\vec{v}_{old}$  is the velocity before rescaling,  $T_0$  is the desired system temperature, and  $T_{ins}$  is the instantaneous temperature of the system. This velocity rescaling method works since the macroscopic temperature of a system is a function of the average kinetic energy. In this manner, the velocities of the

atoms are adjusted such that the instantaneous system temperature approaches the desired system temperature.

### **Periodic Boundary Conditions**

Atomistic MD simulations are performed in an effort to provide fundamental atomic-scale insight into the macroscopic properties of a material system. However, due to limitations in computational power, system sizes are restricted by the number of atomic interactions which will provide reasonable computational efficiency. As such, typical MD system sizes are on the order of nm containing several hundred up to a few million atoms. In order to accommodate these size limitations while also effectively mimicking bulk materials, periodic boundary conditions (PBCs) are applied in three dimensions. For modeling planar surfaces, PBCs are applied in the two dimensions parallel to the surface while the third dimension generally contains a vacuum region. In this manner, PBCs allow small systems of atoms to predict the behaviors of larger macroscopic systems.

An example of a two-dimensional system with PBCs is illustrated in Figure 2-1 where the primary central cell is repeated on all edges and corners imitating an infinite lattice. During the evolution of the system, the particles within the primary cell and each of the periodic cells move in an identical manner. Because of this system design, if a particle exits the primary cell through one of the boundaries, it simultaneously appears through the opposite boundary; as such, the number of particles is always conserved.

### **Statistical Analysis of Forces for Determining Friction Coefficient**

This section details the method used to analyze the friction simulations discussed in Chapters 3 through 6. For these friction simulations, sliding was performed for 20 nm at a rate of 10 m/s and a time step of 0.2 fs. Data from the simulations was written every

500 time steps which corresponds to a time of 100 fs and 1 pm of sliding. Through this approach, each 20 nm friction simulation resulted in 20,000 pairs of frictional and normal forces. Due to the large quantity of data, it was necessary to reduce the data in a manner that was both accurate and meaningful. To begin, a boxcar averaging of the frictional and normal force data was performed every 0.2 nm (200 data points) of sliding resulting in an average force,  $F_i$ , and standard deviation,  $\sigma_i$ , for each boxcar,  $i$ ; the value of 0.2 nm was used as it corresponds to the approximate spatial resolution of microscopic tribological experiments [73]. The uncertainty in each of the averaged boxcar forces was taken as the standard deviation of the mean:

$$\sigma_{mean} = \frac{\sigma_i}{\sqrt{N}} \quad (2-19)$$

where  $N$  is the number of data points in the boxcar data set.

The friction coefficients from the MD simulations were determined through the generation of friction load ramps as is common practice in atomic-scale friction simulations [58, 60, 74] and experiments [75-77]. In order to form a friction load ramp, the boxcar averaged forces and standard deviations must be reduced to a best representative frictional and normal force pair for each 20 nm sliding simulation. These best representative forces were calculated using a weighted average [78]:

$$F_{best} = \frac{\sum_{i=1}^N w_i F_i}{\sum_{i=1}^N w_i} \quad (2-20)$$

where  $w_i$  is the weight for boxcar  $i$  and was determined by:

$$w_i = \frac{1}{\sigma_i^2} \quad (2-21)$$

The uncertainty in  $F_{best}$  was calculated as:

$$\sigma_{best} = \left( \sum_{i=1}^N w_i \right)^{-1/2} \quad (2-22)$$

For these force calculations, at least the first 2 nm of friction were not included so as to avoid any potential negative influence from the initial stages of sliding; this was also done so that the analysis was always performed during steady-state force conditions. In order to calculate the friction coefficient for the systems in this work, sliding simulations were performed at varying applied normal loads. In the manner described above, the best representative frictional and normal forces for each applied normal load were plotted together as friction force versus normal force forming the desired friction load ramps. From these friction load ramps, the coefficient of friction for each system was then calculated as the linear fit of the friction versus normal force data.

### **Atomic Force Microscopy Experiments**

The experimental topographical and tribological measurements discussed in Chapter 8 were performed using atomic force microscopy (AFM). Specifically, the AFM used in this study was controlled with AFM 100 and SPM 1000 electronics and SPM32 software (RHK Technology, Troy, MI). In AFM, interfacial forces are measured between a tip and a surface in order to determine atomic positions. The tip utilized in this work was a triangular cantilever with a sharp silicon nitride ( $\text{Si}_3\text{N}_4$ ) tip (Digital Instruments) with a manufacturer's reported force constant of 0.58 N/m. In these experiments, the samples were positioned on a piezoelectric tube scanner and manipulated relative to the fixed AFM tip causing tip deflection from the resultant interfacial forces. The experiments performed in this work were carried out at ambient pressures and in a dry nitrogen environment with less than 3% relative humidity.

## Measuring Tip/Sample Interactions

In the AFM, tip deflection is measured by positioning a laser (light amplification by stimulated emission of radiation) to reflect from the top of the cantilever towards a four quadrant photodetector. Prior to any measurements, the laser spot is adjusted to be centered on the photodetector such that the spot intensity in each of the four quadrants is equal. In this manner, the normal and lateral signals can be determined from the displacement of the laser spot on the photodetector; the normal and lateral signals are defined as the difference between the spot intensities for the top and bottom quadrants and between the spot intensities for the left and right quadrants, respectively. By measuring the deflection of the cantilever and relating it to the manipulation of the piezoelectric tube scanner in three dimensions, it is possible to determine the sample topography and the frictional forces between the tip and sample.

The topographical imaging was performed in constant contact mode. In this mode, a feedback loop was enabled which adjusted the height of the sample on the piezoelectric tube scanner in order to maintain a constant normal deflection of the cantilever. From this method, the sample topography was determined based on the change in the voltage applied to the piezoelectric scanner. The friction measurements were performed in a different manner by measuring the lateral deflection of the cantilever. For these measurements, the feedback loop was disabled which allowed for changes in the normal deflection of the cantilever. Friction scans were collected over a length of 100 nm at a rate of 1  $\mu\text{m/s}$  at sequentially increasing normal loads through a stepwise addition of voltage to the piezoelectric tube scanner. By measuring the average friction force at each normal load and plotting the friction force versus normal

force, the friction coefficients were determined from the linear fit of these friction load ramps [75-77, 79, 80].

### **Calibration of AFM tips**

For the normal force calibration, the thermal fluctuation method was used, as described by Butt and Jaschke [81], which has been shown to be a good approach for triangular cantilevers [82]. In this non-contact calibration method, the resonance frequencies of the thermal vibration modes for the triangular cantilever were measured, allowing the normal force constant to be calculated. For the cantilever used in these AFM experiments, the force constant was determined to be 0.307 N/m rather than the manufacturer's reported value of 0.58 N/m. Calibration of the lateral forces was conducted using the wedge method described in detail by Ogletree *et al.* [83]. In this approach, the normal and lateral forces were recorded while sliding the tip along a surface with known tilt angles which, for this study, was a silicon wafer grating. The force calibration was determined from the measurement of the lateral force signal as a function of the applied load and tilt angle of the surface. The tip radius was measured by imaging the ridges between facets along the silicon surface using the same method as described by Carpick *et al.* for faceted SrTiO<sub>3</sub> (305) surfaces [84]. Through this approach, the tip used in the friction experiments was found to have an approximate radius of  $37.4 \pm 3.6$  nm.

### **Materials Informatics and Data Mining**

The materials informatics and data mining methods used in Chapter 9 are introduced in this section. Materials informatics is emerging as an essential tool for materials research; in this method, data mining, statistical inference, and materials science are combined in order to accelerate the rate of new material design and

discovery. Through the extraction of as yet unknown links between material properties, materials informatics provides useful strategies for the quick and accurate prediction of the desired properties of new materials [85-89]. In this manner, the conventional trial-and-error strategies of testing the unknown properties of new materials one at a time are avoided; as such, this data-driven method identifies the hidden relationships in a large collection of complex data and correlates them as predictive rules to develop new materials with specific desired properties. By identifying suitable candidate materials in this high-throughput manner, a materials space can be effectively searched for specific applications.

### **Principle Component Analysis**

One important tool used in materials informatics is the multivariate dimensionality reduction method termed principal component analysis (PCA). In this method, the dimension of an original, typically correlated, variable space for a large number of samples is transformed into an uncorrelated new, latent variable space referred to as principal components (PCs) which are independent linear combinations of the original variables [90]. Specifically, a data matrix  $X$ , which represents the original variable space, is decomposed into two orthogonal matrices  $U$  and  $V$  and is given by:

$$X = USV^T \quad (2-23)$$

where  $S$  is the diagonal matrix of the eigenvalues and the products  $US$  and  $V$  represent the score matrix and loading matrix, respectively. The PCs are the eigenvectors of the covariance matrix in which the covariance of each component demonstrates how the variables vary from the mean value relative to each other in the data matrix; the covariance between variables  $x$  and  $y$ ,  $\text{cov}(x, y)$ , is defined as:

$$\text{cov}(x, y) = (n-1)^{-1} \sum_{i=1}^n (x_i - \bar{x})(y_i - \bar{y}) \quad (2-24)$$

where  $\bar{x}$  and  $\bar{y}$  are the mean values of variables  $x$  and  $y$ , respectively.

The maximum variance (eigenvalue) in the original dataset is accounted for in the first PC, while the second PC is orthogonal (i.e. uncorrelated) to the first and accounts for the largest amount of the remaining variance. As such, each additional PC is orthogonal to the previous and represents the next highest variance; thus, the  $n^{\text{th}}$  PC is orthogonal to all others and has the  $n^{\text{th}}$  largest variance in the set of PCs. By transforming the original data to this new high dimension coordinate system, PCA enables the visualization and identification of the relationships between samples and variables in the reduced dimensional PC space while maintaining minimal information loss; this is accomplished by projecting the samples and variables onto a reduced dimensional hyperplane. In particular, the relationships in PC space between the samples, which are shown in scores plots, play a key role in the classification of the samples; the relationships between the variables, which are shown in loadings plots, allow for the selection of important variables by minimizing the redundancy among a large number of correlated variables.

### **Recursive Partitioning (Regression Tree)**

Another important method used in materials informatics, recursive partitioning, divides a feature space into a set of subgroups based on the relationships between different samples. The recursive partitioning method used in this work is called a regression tree since the primary goal is to predict an output value for each of the subgroups. The general idea of recursive partitioning is to reduce the feature space into smaller subsets by grouping members of the data matrix which have the highest

similarity. A regression tree is a graphical expression of the subgroup divisions according to the similarities between the samples, which is determined by the sum of squared deviations of the predictor variables from their average value. The error sum of squares,  $SS$ , is determined by:

$$SS = \sum_{i=1}^n (y_i - c)^2 \quad (2-25)$$

where  $y_i$  is the value of the predictor variable for sample  $i$  and  $c$  is the average value for the predictor variable. In order to determine the best splitting values among predictor variables for the subgroups, the following optimization condition is used:

$$\min_{j,k} \left[ \min_{c_1} \sum_{x_i \in R_1} (y_i - c_1)^2 + \min_{c_2} \sum_{x_i \in R_2} (y_i - c_2)^2 \right] \quad (2-26)$$

where  $R_1$  and  $R_2$  are the subsets given by:

$$R_1 = \{X \mid X_j \leq k\} \quad (2-27)$$

$$R_2 = \{X \mid X_j > k\} \quad (2-28)$$

where  $j$  and  $k$  are the splitting variable and the splitting value, respectively. Also,  $c_1$  and  $c_2$  are the average values in each partitioned subspace  $R_1$  and  $R_2$  as given by:

$$c_1 = \text{average}(y_i \mid x_i \in R_1) \quad (2-29)$$

$$c_2 = \text{average}(y_i \mid x_i \in R_2) \quad (2-30)$$

## Variable Evaluation

Since there is no single best method for the evaluation of important variables, the approach for the work described in Chapter 9 was to combine the suggestions of two different variable evaluation methods, variable importance in projection (VIP) and error sum of squares (SS); the variables identified as significant by both criteria were taken to

be the most important ones. In partial least squares regression, the relative significance of each variable is evaluated using the measure of VIP [91]. Assuming there are  $p$  latent variables ( $L_i$ ; where  $i = 1, 2, \dots, p$ ) selected from  $n$  independent variables ( $X_j$ ; where  $j = 1, 2, \dots, n$ ), the measure of VIP is determined by:

$$(VIP)^2 = \frac{\sum_{i=1}^p SS_i \cdot W_{ij}^2}{\sum_{i=1}^p SS_i} \quad (2-31)$$

where  $SS_i$  is the sum of squares which represents the variance explained by the latent variable  $L_i$ . The term  $W_{ij}$  is the loading vector between the latent variable  $L_i$  and the independent variable  $X_j$ . Equation 2-31 indicates that the ratio of the variance explained by  $X_j$  to the total variance describes the relative influence of each independent variable,  $X_j$ , on the total variance. Specifically, for the selection of significant variables, the cutoff value based on the VIP score is typically unity. In other words, a predictor variable is classified as important if the VIP value is greater than one since the mean value of  $(VIP)^2$  is equal to unity. Similarly, another measure of the contribution of individual variables is the error sum of squares (SS) which is described in Equation 2-25. As discussed previously, SS is the variable evaluation method used when generating a regression tree model; that is, the variation of the SS due to the subspace partitioning is determined for each individual variable, and the relative importance is compared for the variable selection.

Table 2-1. Lennard-Jones parameters for each element type included in the MD simulations discussed in this work.

Element type	$\sigma$ (Å)	$\epsilon/k_B$ (Kelvin)
C	3.35	51.2
H	2.81	15.0
Mo	4.20	6.8
S	3.13	80.4

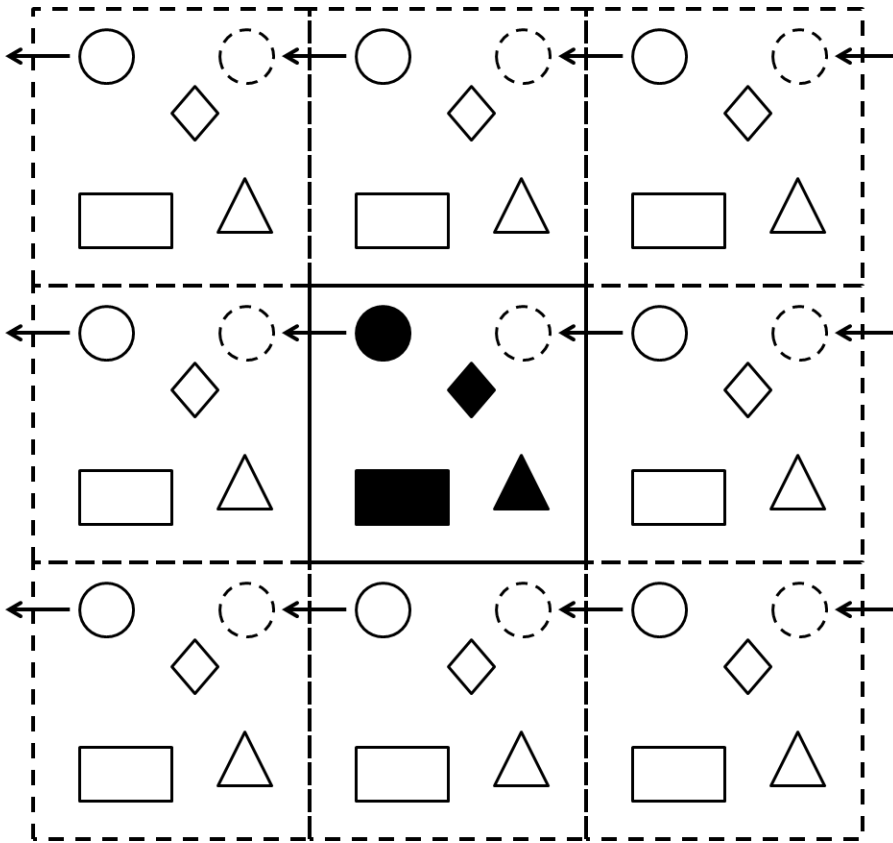


Figure 2-1. Schematic representation of two-dimensional periodic boundary conditions illustrating the central primary supercell along with the surrounding periodic images. Arrows indicate how particles enter and exit the central supercell.

### CHAPTER 3 TRIBOLOGICAL PROPERTIES AND LUBRICATION MECHANISMS OF CARBON NANO-ONIONS\*

Tribological interest in various inorganic and carbon fullerenes and nanotubes has grown continually since the discovery of carbon fullerenes in 1985 [93] and the discovery of carbon nanotubes (CNTs) in 1991 [94]. Another material of great potential importance for lubrication is the carbon nano-onion (CO), which was discovered by Ugarte in 1992 [24] and may be thought of as a spherical nested carbon structure. The desirable tribological performance of these and similar nanomaterials stems from their weak van der Waals (vdW) interactions with surrounding materials; also contributing to their tribological performance are the chemical inertness and structural stability provided by the elimination of dangling bonds through the formation of the closed-shell structure [24, 25, 95]. Additionally, the spherical morphology of fullerenes and COs along with the columnar morphology of nanotubes allow for the potential of rolling at the frictional interface, opening up the possibility of additional interesting properties [25, 96].

As was noted by Hirano and Shinjo [97], controlling friction is one of the most critical goals in the area of tribology; the first step to controlling friction is to develop an understanding of the mechanisms involved in the lubrication process [98]. With this in mind, a number of computational and experimental studies have been performed in recent years in an attempt to characterize and understand the frictional behavior and lubrication mechanism of many different lubricants including nanomaterials [39, 99-103]. Experiments under boundary lubrication conditions have shown that two types of nanomaterials, CNTs and inorganic fullerene-like (IF) MoS<sub>2</sub> and WS<sub>2</sub> nanoparticles,

---

\* Adapted from Bucholz, E.W., Phillpot, S.R., Sinnott, S.B.: Molecular dynamics investigation of the lubrication mechanism of carbon nano-onions. *Comput. Mater. Sci.* **54**, 91-96 (2012) [92]

provide friction reduction through different mechanisms when used as lubricant additives. Specifically, experiments involving single-wall CNTs showed that the amorphization of their structure led to friction reduction during the tribological tests [39, 40]. Conversely, experimental analyses of friction contacts containing IF nanoparticles demonstrated that the exfoliation of lubricious lamellar sheets of MoS<sub>2</sub> or WS<sub>2</sub> within the tribological interface was the primary source of friction reduction, especially under high uniaxial pressures [39, 41].

There are inherent structural similarities between COs and IFs in that both are spherical nested nanostructures. It is therefore reasonable to assume that the lubrication mechanism of COs will be similar to that of IFs, with graphitic exfoliation occurring at the sliding interface when subjected to compressive and frictional forces, especially at higher contact pressures. However, recent publications have demonstrated that, while providing excellent anti-wear and friction reducing properties, the COs remain intact during the friction experiments [103, 104]; no evidence is either predicted or observed for the exfoliation of the COs to form lubricious graphene sheets at the interface during friction. This suggests that the lubrication mechanism of COs is different than that of IF nanoparticles discussed previously.

Here, we use classical molecular dynamics (MD) simulations to investigate the tribological behavior of COs as they are subjected to friction between coupled, amorphous, hydrogen-terminated diamond-like carbon surfaces in a perfect ultra-high vacuum environment. From these simulations, we demonstrate that the frictional properties are controlled by a rolling/sliding lubrication mechanism. Through detailed analysis, we quantify the relative importance of rolling and sliding on the frictional

properties of COs as a function of the structure and conditions of these tribological simulations.

### **Computational Details**

For the MD simulations performed in this work, the forces acting on the atoms were calculated using the second-generation hydrocarbon reactive empirical bond order (REBO) interatomic potential [66] which was used for the short-range covalent interactions coupled with a Lennard-Jones (LJ) 12-6 potential [71] for the long-range vdW interactions. The REBO and LJ potentials for describing atomistic simulations have been used successfully in recent years for determining the mechanical [51, 53, 61, 62] and tribological [49, 50, 54, 57, 63] properties of carbon nanomaterials and other carbon-based systems [22, 59, 60, 64, 65]. In addition, it has been recently demonstrated that the REBO potential, while properly modeling covalent materials near equilibrium conditions, significantly underestimates the barriers to binding between atoms [105]. Unlike the REBO potential which uses a finite distance-based cut-off function to determine intra- and intermolecular interactions, a different hydrocarbon interatomic potential, the adaptive intermolecular REBO (AIREBO) potential [106], provides additional constraints through the implementation of a switching function which utilizes both distance-based and connectivity-based switching criteria allowing the potential to better determine the proper binding barriers between atoms [58]. However, it has further been demonstrated that the REBO potential yields qualitatively similar trends in the calculated forces [22] while also yielding quantitatively similar friction forces at given interfacial separation distances [74]. It is for each of these reasons and because of the significantly reduced computational expense of the REBO potential that led to its selection for these simulations.

Experimentally, COs can be synthesized through the high temperature annealing of diamond nanoparticles which results in the progressive graphitization from the periphery of the nanoparticles inward towards the center [107]. Also, it is known that the structure of the synthesized nano-onions is dependent on the conditions of the annealing [108] where the nano-onions obtained can be fully graphitized or can contain a residual diamond core. With this in mind, for the MD simulations presented in this study, two structures of nano-onions were considered: those that contained residual diamond cores (D-COs) and those with hollow cores (COs). In these MD simulations, a single layer of either four COs or four D-COs were compressed and submitted to friction between two hydrogen-terminated, amorphous diamond-like carbon (DLC) substrates that were 2 nm thick and consisted of 12480 atoms each as is shown in Figure 3-1. The DLC substrates modeled in these simulations had a  $sp^3$ -to- $sp^2$  carbon ratio of approximately 1:3. Also, the DLC contained no hydrogen within the substrate with hydrogen termination only for the carbon atoms nearest the sliding interface.

Regarding the nanoparticles, each of the COs was comprised of 840 atoms, was approximately 2.2 nm in diameter, and had three fullerene layers:  $C_{540}$  (outer layer),  $C_{240}$  (middle layer), and  $C_{60}$  (inner layer). Similarly, each of the D-COs was comprised of 815 atoms, was also around 2.2 nm in diameter, and had two layers:  $C_{540}$  (outer layer) and a 275-atom residual diamond core. With periodic boundaries being applied in the plane parallel to the DLC/CO interface, both the CO and D-CO systems were compressed at a rate of 10 m/s prior to the application of the lateral frictional forces. Contact pressures of between 1 and 5 GPa, for the given CO coverage, were then selected, with these pressures being determined using the apparent contact area of the

periodic substrates which was  $\sim 35 \text{ nm}^2$ . The tribological simulations of these systems were performed by sliding the outermost 0.3 nm of the DLC substrates which were rigid and not permitted to evolve during the MD simulations at a rate of 10 m/s for 20 nm at a temperature of 300 K. The sliding distance of 20 nm was used in these friction simulations since this distance was found to be sufficient to ensure that the measured frictional and normal forces reached steady state conditions. The temperature in these simulations was maintained using Langevin thermostats [71] positioned on the 0.3 nm of the DLC substrates nearest to the rigid atoms mentioned previously. For these simulations, the thermostats were not used in the direction of sliding in order to avoid influence on the friction forces due to Langevin dissipation as is commonplace in tribological simulations [65, 109].

### **Mechanical Response during Compression**

Prior to performing the tribological simulations in this study, the CO and D-CO systems were uniaxially compressed to approximately 40 GPa with the desired loads of 8 to 43 nN per nano-onion, which corresponds to 1 to 5 GPa for the given CO coverage, being selected for further simulation when subjected to frictional forces. The compression simulations showed that COs and D-COs mechanically respond similarly to increasing and decreasing compressive forces indicating a comparable elastic modulus for both nanoparticles (Figure 3-2A) with both the COs and D-COs exhibiting a transition from elastic to plastic deformation above a force of approximately 86 nN per nano-onion, which translates to 10 GPa for the coverage of COs at the interface, as the carbon atoms began to convert from threefold to fourfold coordination (Figure 3-2B). Despite assumptions that the presence of a diamond core should provide additional stiffness to the D-COs relative to COs, it was likely a result of the exceedingly small size

of the 275-atom diamond that both nanoparticles exhibited such similar mechanical properties. During the uniaxial compression of IFs, it has been experimentally demonstrated that the nanoparticles become exfoliated into lubricious lamellar sheets at contact pressures that vary from 1 to 2.5 GPa without being subjected to frictional forces [48]. However, as the MD results indicate, COs and D-COs exhibited no evidence of graphitic exfoliation during uniaxial compression up to contact pressures of ~40 GPa.

### **Tribological Properties of Carbon Nano-onions**

#### **Formation of Interfacial Bonds during Friction**

Through the four nano-onion MD simulations of friction with both COs and D-COs at 1 to 5 GPa, strong interfacial bonds were often developed between the individual nano-onions and the DLC interfaces, with the number of bond formations being largely dependent on the contact pressure of the system as is shown in Figure 3-3. For the COs, little or no structural change was observed during sliding at the lower contact pressures of less than 2.5 GPa, which corresponds to less than 21.5 nN per nano-onion. However, at higher pressures of 5 GPa, approximately 43 nN per nano-onion, numerous bonds formed between the nano-onions and the substrates; these numerous interfacial bonds are highlighted in Figure 3-4 for the COs sliding at 5 GPa. Likewise, we found that a large number of strong bonds formed during the D-CO simulations at all contact pressures considered. We have found that these interfacial bonds more readily formed in D-COs as a result of the dangling bonds at the periphery of the diamond core. When covalent bonds formed between the C<sub>540</sub> fullerene layer and the diamond core, localized strain was introduced to the fullerene in the surrounding region since the introduction of 4-fold coordinated atoms is a defect in the perfect 3-fold coordinated

structure of the fullerene. When this strain was added, the neighboring atoms were then more apt to form interfacial bonds as a means of strain reduction.

### **Relationship between Interfacial Bonds and Measured Forces**

In order to investigate the impact of interfacial bond formations on the tribological properties of nano-onions, we performed simulations of individual COs compressed between DLC substrates. We maintained comparable contact pressures and forces per nano-onion in order to directly relate the results of the single nano-onion simulations with those of the four nano-onion simulations. The results of the 5 GPa single nano-onion simulations indicated that the system displayed low friction prior to any bond formations when the CO was able to roll at the interface (Figure 3-5A). Due to the small apparent contact area ( $\sim 8.5$  and  $\sim 35$  nm<sup>2</sup> for the single and four CO systems, respectively), in the absence of chemical bonds, surface adhesion is expected to be negligible relative to the applied lateral and normal forces; thus, without interfacial bonds, the forces acting between the nano-onion and both substrates are determined by the LJ portion of the interatomic potential. These weak vdW forces provided the nano-onion with the necessary angular momentum for rolling to occur and were weak enough so as not to prevent rolling. However, when the CO became bonded with one or both of the DLC surfaces (Figure 3-5B), the CO transitioned to a sliding behavior at the interface, and the frictional force became noticeably larger, leading to a decrease in the lubricious behavior of the system. When numerous bonds formed between the substrates and the CO, the nano-onion was no longer able to slide across the interface. The presence of many interfacial bonds led to large fluctuations in the normal and frictional forces since the CO's inability to slide led to the stretching (Figure 3-5C) and eventual breaking (Figure 3-5D) of the interfacial bonds.

As with the single nano-onion simulations, the same influence of interfacial bond formations on measured friction forces was observed during the four nano-onion simulations. Figure 3-6A shows the evolution of normal and frictional forces during friction of COs at an apparent contact pressure of 1 GPa when no interfacial bond formations were observed throughout the tribological simulation (Figure 3-3). In these conditions, the four nano-onion system was characterized by very low friction forces throughout the simulation. In contrast, Figure 3-6B shows the measured normal and frictional forces during sliding of the four CO system at 5 GPa when numerous bonds were observed between the DLC substrates and the COs (Figure 3-4); here, the results showed a significant increase in the measured friction forces compared to Figure 3-6A.

The results of the single and four nano-onion MD simulations indicated that the presence of strong interfacial bonds had a significant impact on the COs' tribological performance. Recent tribological simulations involving diamond and DLC sliding contacts of varying degrees of hydrogenation have demonstrated a similar connection between increasing friction and the formation of interfacial covalent bonds [22, 58, 65, 74, 110, 111]. In these studies the presence of unsaturated sp- and sp<sup>2</sup>-hybridized carbon atoms near the sliding interface serve as initiation points for the formation of strong carbon-carbon bonds across the interface. It is further shown that the number of interfacial bonds goes up with increasing load, and that an increase in interfacial bonding results in a subsequent rise in predicted friction force since each of these bonds must stretch and break in order to continue sliding. This behavior results in a periodicity of friction force versus sliding distance due to the formation, stretching, and

breaking of these interfacial bonds [22]. As can be seen in Figure 3-5, this periodicity was also demonstrated for the single nano-onion simulations after 10 nm of sliding.

The results for the CO and D-CO simulations agree well with the literature findings mentioned above for diamond and DLC tribological systems. As expected, the existence of two- and threefold coordinated DLC atoms near the interface served as the initiation points for the formation of the observed interfacial bonds. In addition, the number of bonds that were formed increased as the contact pressure increased which was also related to an increase in the friction force. However, unlike the diamond and DLC findings, the increase in friction predicted here and illustrated in Figure 3-5 between 5 and 7 nm of sliding was not a result of the stretching and breaking of the interfacial bonds that were formed. Rather, there was a direct correlation between these observed frictional properties and the amount of rolling and/or sliding of the individual nanoparticles within the simulations.

### **Discussion of Rolling and Sliding Behavior**

Through analysis of the average angular velocities of the nano-onions relative to the displacement of the DLC substrate, the average percentage of rolling and/or sliding of the particles at each contact pressure for the four nano-onion simulations was quantified in Figure 3-7. The ability to quantify the relative percentage of rolling and sliding of the individual nano-onions is based on the 2:1 ratio between substrate displacement during friction and the displacement of a perfectly rolling sphere. Through this relationship along with the approximate circumference of the COs and D-COs where  $360^\circ$  of rotation equals one nano-onion circumference of displacement, it is possible to determine the necessary angular velocity which will correspond to the perfect rolling of the nano-onions; thus, the average percentage of rolling and/or sliding

is a calculation based on this relationship. As indicated in Figure 3-7A, the COs were characterized by a predominantly rolling behavior at lower contact pressures, with sliding occurring primarily at higher pressures. The D-COs, on the other hand, as illustrated in Figure 3-7B, predominantly slid at all pressures. It should be noted that the nano-onions, rather than being spherical, have a slightly faceted structure of the  $C_{540}$  outer walls of the COs and D-COs which resulted in alternating periods of smooth and abrupt rolling behavior. The presence of these abrupt rolling processes produced temporarily increased angular velocities with the resultant effect of short-term rolling percentages greater than 100% which was the source of much of the variance seen in Figure 3-7 at high amounts of rolling. The remaining fluctuation in these percent rolling calculations resulted from the averaging of the angular velocities of each of the four nano-onions which were moving independently of one another during the friction simulations.

In recent years, much experimental and computational work has characterized the motion of carbon nanotubes and fullerenes that are compressed and slid between substrates or displaced by an atomic force microscope (AFM) tip. Experimental studies carried out using an AFM tip to laterally manipulate CNTs on different surfaces have indicated that CNTs display preferential sliding when the hexagonal lattice is in incommensurate contact with the surface [112, 113]. Only when the lattices of the CNTs were in registry with the surface did the nanotubes begin to roll along the surface maintaining the commensurate contact. The results of the computational simulations by Buldum and Lu [27] and Schall and Brenner [114] agree with these experimental

findings. In particular, they demonstrated that during translation of CNTs across a graphite surface, a commensurate contact was necessary for the CNTs to roll.

Simulations have also been performed to examine C<sub>60</sub> fullerenes as nano ball bearings. In these studies, the C<sub>60</sub> fullerenes were intercalated between graphite sheets [115, 116] and nanotube layers [57]. The findings indicated that the fullerenes provide lower frictional forces due to their ability to roll within the interface. Unlike these previous experimental and computational studies of CNTs and fullerenes, the results reported here predict the existence of rolling motion for the COs and D-COs between incommensurate DLC surfaces. Although a commensurate contact was reported to be necessary for CNT rolling to commence, these findings were reported for CNTs that were only subjected to lateral forces and no compressive forces. Furthermore, the studies of C<sub>60</sub> fullerenes did not provide a comparison of commensurate and incommensurate contacts for rolling to be observed. Our results for COs and D-COs agree well with similar MD simulations performed by Heo *et al.* [54] which showed that CNTs are displaced via a combined rolling and sliding behavior when compressed and slid between DLC substrates. Our results along with this previous literature finding make it evident that when subjected to compressive forces, commensurability is no longer required for nanomaterials such as CNTs and COs to roll.

### **Relative Influence of Rolling and Sliding on Coefficient of Friction**

Through analysis of the steady state forces during each of the CO and D-CO four nano-onion simulations, we generated a friction load ramp in the same manner as described in detail in Chapter 2 where the friction coefficient is taken to be the linear fit of the data for friction force versus normal force. The friction load ramp from these four nano-onion simulations is shown in Figure 3-8 relative to the predominant rolling or

sliding behavior observed during the friction simulations. As can be seen, the presence of rolling versus sliding at the interface for these nano-onion systems results in friction coefficients differing by an order of magnitude:  $\mu \sim 0.029$  and  $0.151$ , respectively. Since rolling of the nano-onions was the lubrication mechanism during these simulations before the formation of interfacial bonds and sliding was the mechanism after bonds form, it is possible that further friction beyond 20 nm could indicate that rolling is only a temporary phenomenon with sliding being the end behavior at each contact pressure. However, since steady state forces were maintained during these simulations, there is too much unnecessary computational expense to continue these friction simulations beyond 20 nm. Due to the steady state nature of these simulations, it is a reasonable assumption that rolling is not a short-term behavior but rather a mechanism for achieving low friction coefficients under appropriate tribological conditions. Therefore, these results indicate that carbon nano-onions have the potential to provide optimal lubrication for tribological applications in systems where the conditions will allow for rolling of the nano-onions at the interface since the tribological performance begins to break down once sliding of the nanoparticles commences.

### **Summary**

Through the performance of atomistic MD simulations of carbon nano-onions sliding between DLC surfaces, the work presented here demonstrated the ability of nano-onions to roll within a tribological interface and discussed the conditions during which rolling was found to be possible. Furthermore, the results quantified the influence of rolling and/or sliding on the tribological properties of COs and D-COs. The results showed that the relative proportion of rolling and sliding behavior was governed by the formation of interfacial bonds during friction. In particular, the COs exhibited a transition

from rolling to sliding as the compressive loads increased from 21.5 to 43 nN per nano-onion, corresponding to pressures of 2.5 to 5 GPa for the given CO coverage. By contrast, D-COs displayed a prevalence for sliding behavior at all investigated contact pressures which was a result of the presence of the residual diamond core. These simulations further indicated that the transition from rolling to sliding behavior was accompanied by an order of magnitude increase in the coefficient of friction, from  $\mu \sim 0.029$  to 0.151, respectively.

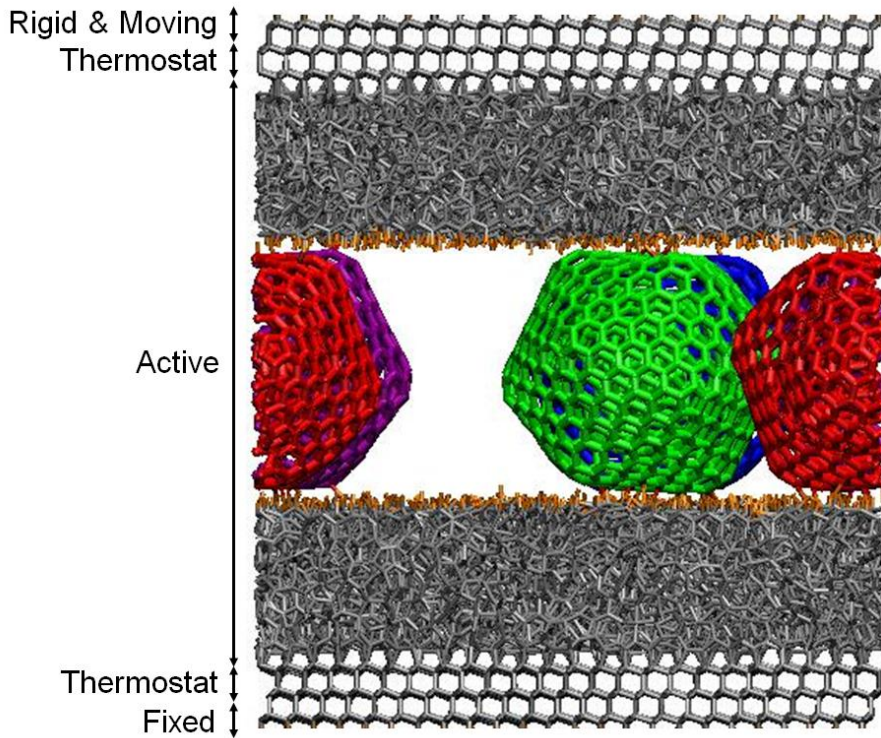


Figure 3-1. Snapshot of tribological system with four COs between DLC surfaces indicating regions of rigid and moving, fixed, thermostat, and active atoms. Colors are only intended to aid in discerning the different nano-onions within the system.

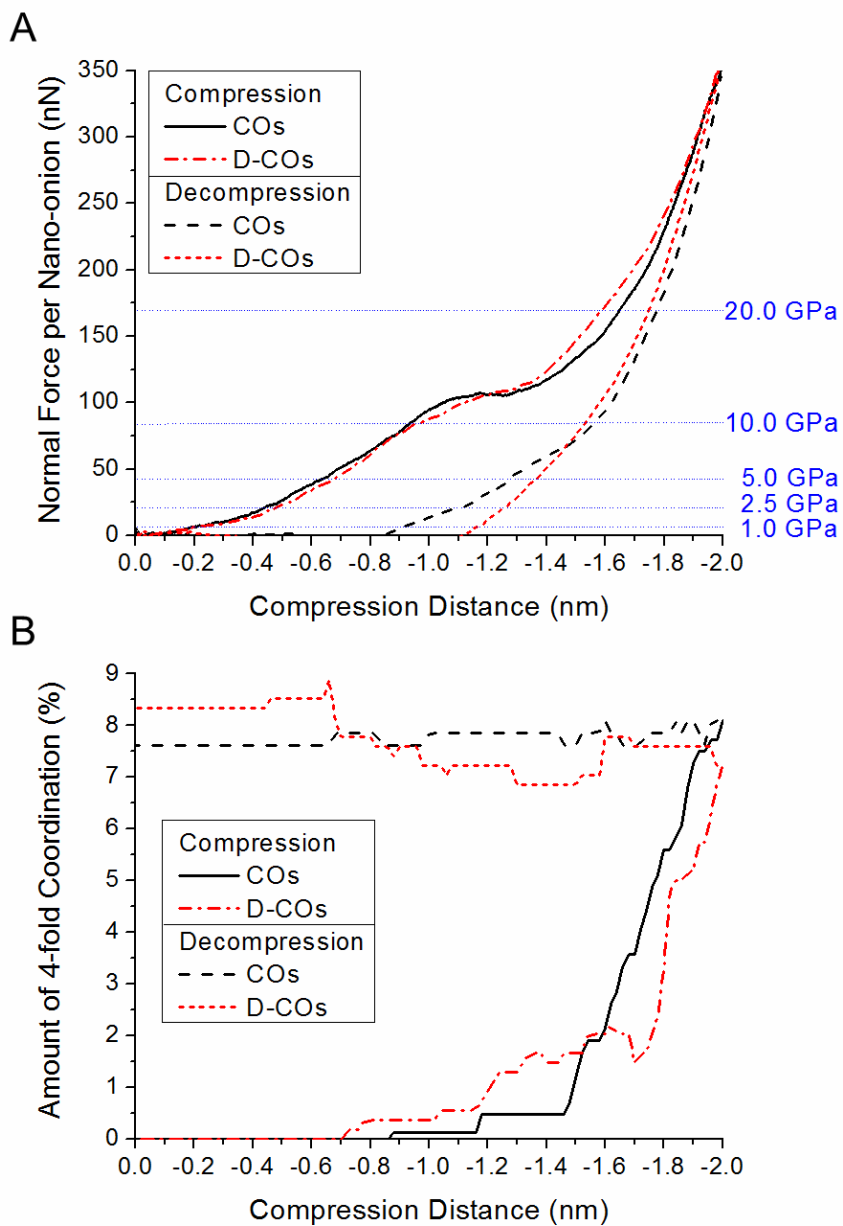


Figure 3-2. Comparison of A) normal forces and B) percentage of fourfold coordination for COs and D-COs during uniaxial compression simulations.

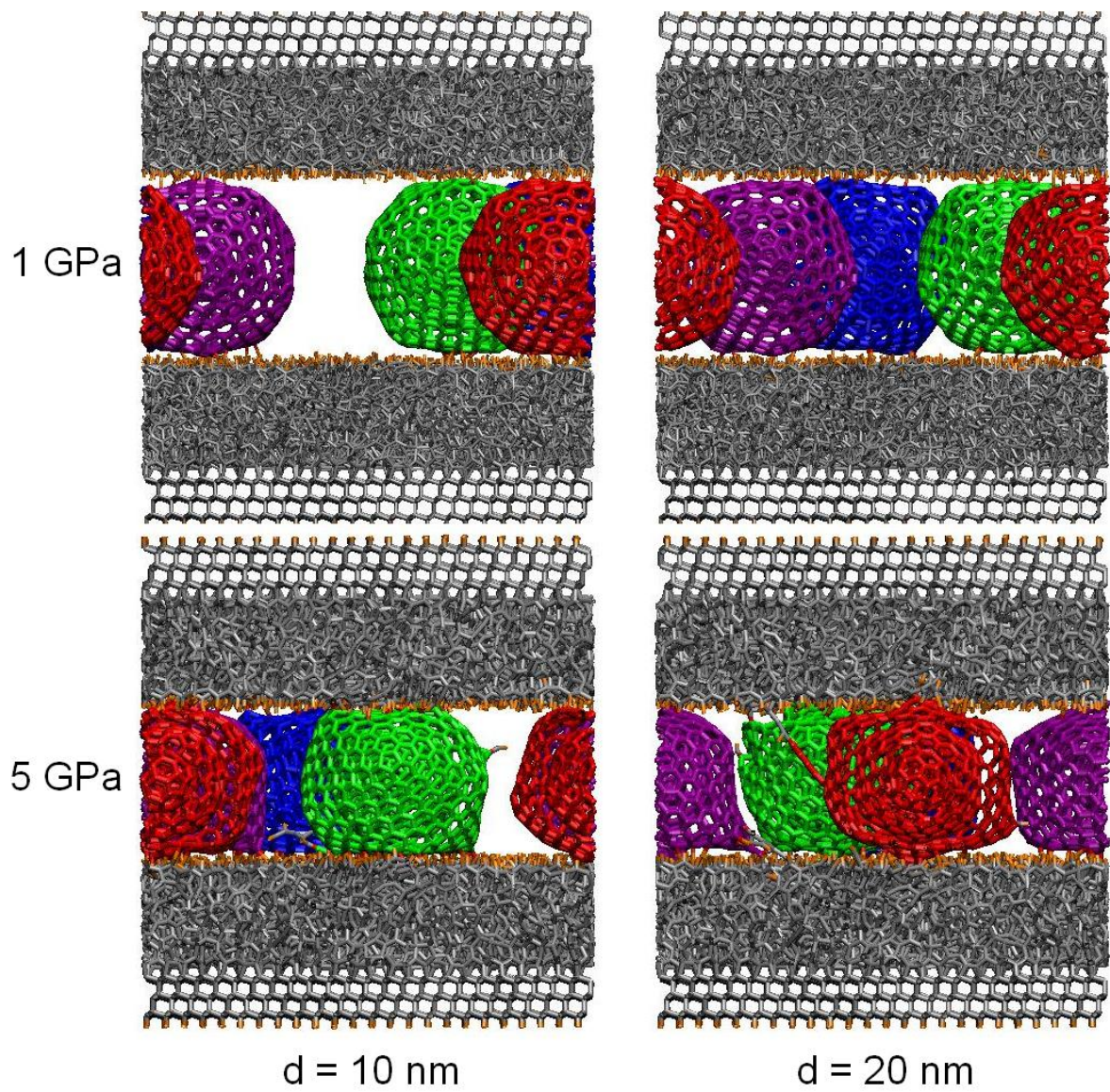


Figure 3-3. Snapshots of COs simulations at different sliding distances,  $d$ , during friction at apparent contact pressures of 1 and 5 GPa.

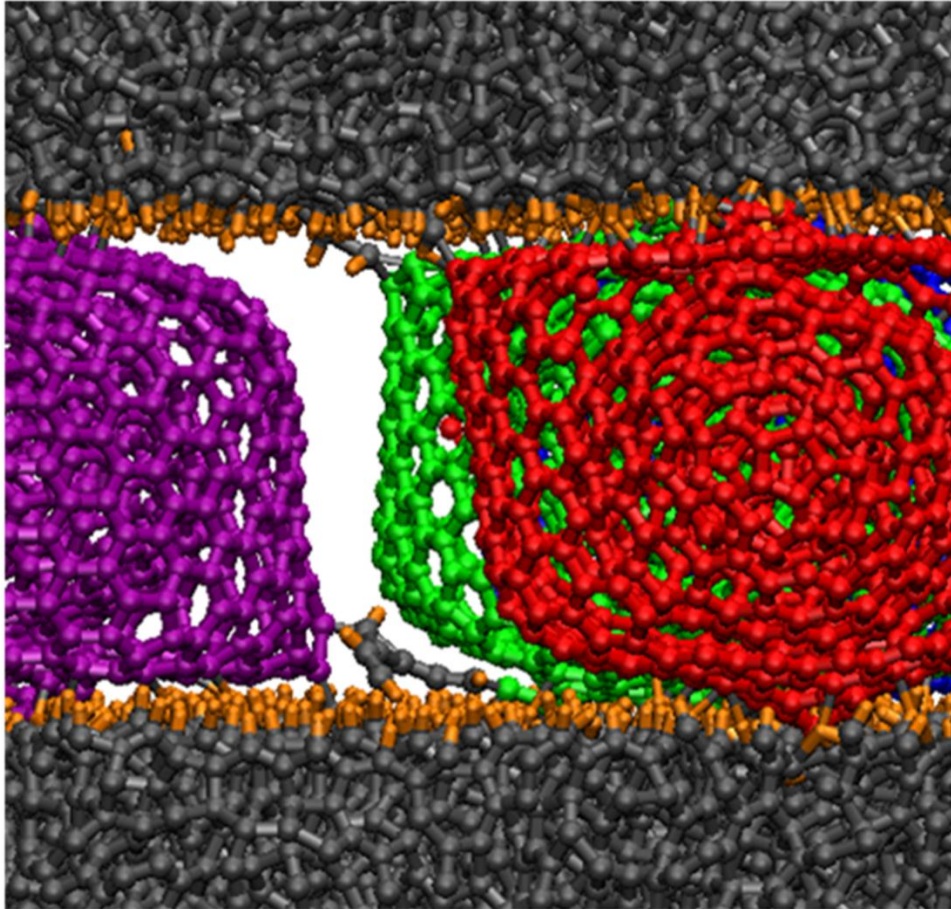


Figure 3-4. Snapshot of COs simulation with four nano-onions indicating strong interfacial bonding during sliding at 5 GPa contact pressure.

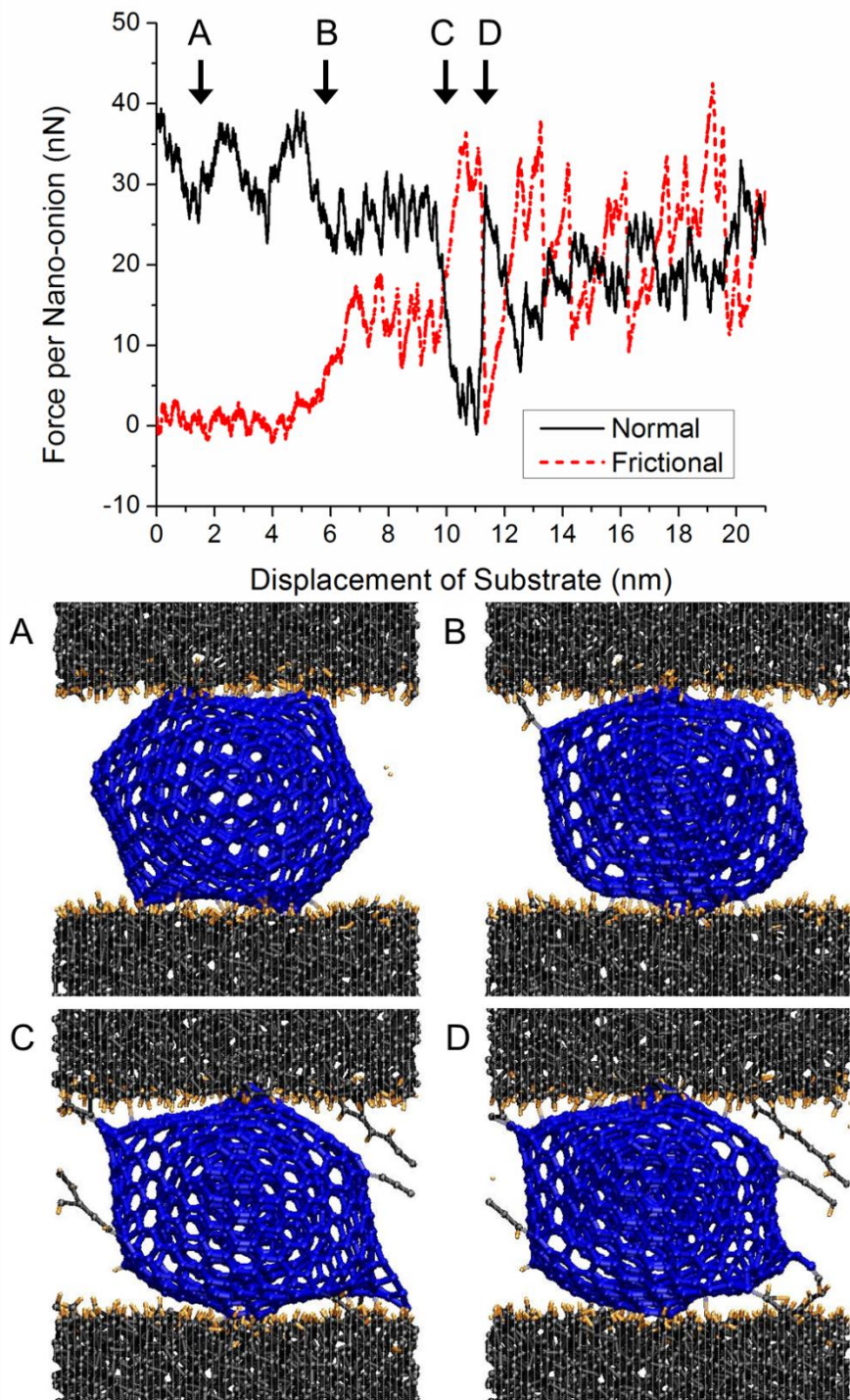


Figure 3-5. Frictional and normal forces for single CO sliding at 5 GPa compression. Images illustrate the force fluctuations observed when CO is A) inert and rolling, B) sliding because bonded with one DLC substrate, C) unable to slide when bonded with both DLC substrates, and D) resuming sliding as some interfacial bonds break.

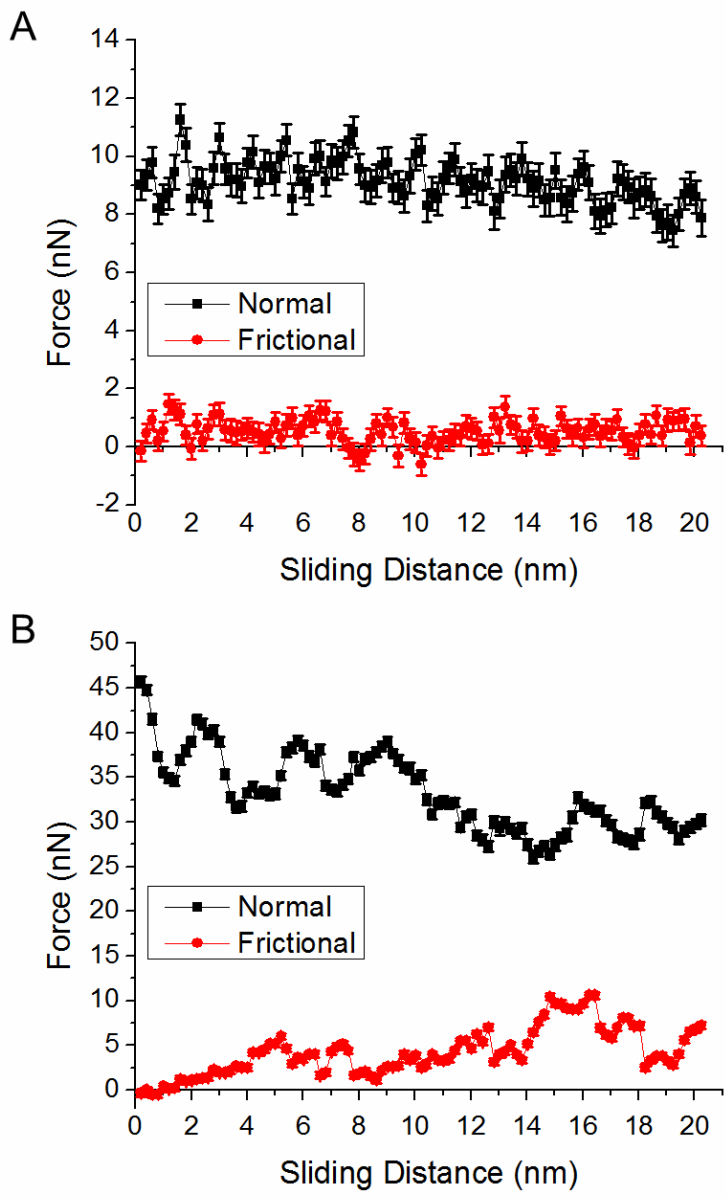


Figure 3-6. Frictional and normal forces during friction simulations with four COs at contact pressures of A) 1 GPa and B) 5 GPa.

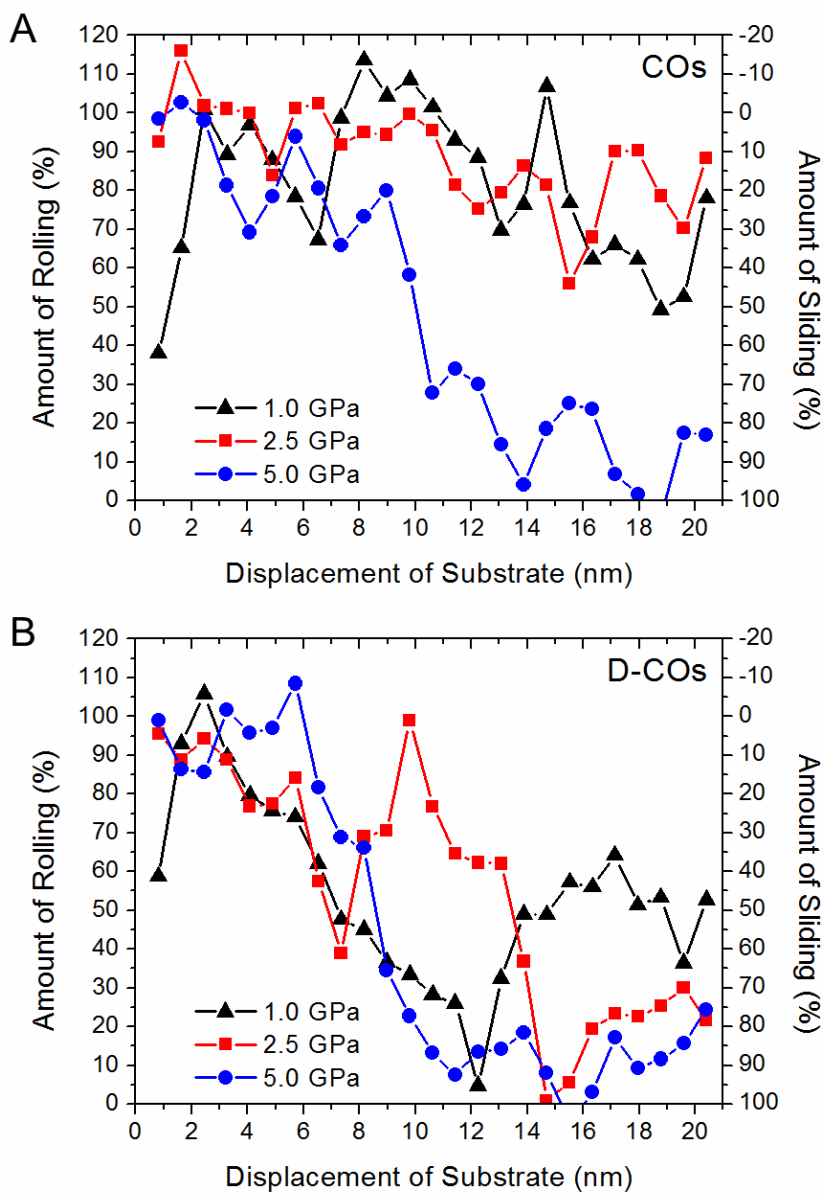


Figure 3-7. Percentage of rolling and sliding for A) COs and B) D-COs during friction of the four nano-union systems at 1, 2.5, and 5 GPa contact pressures.

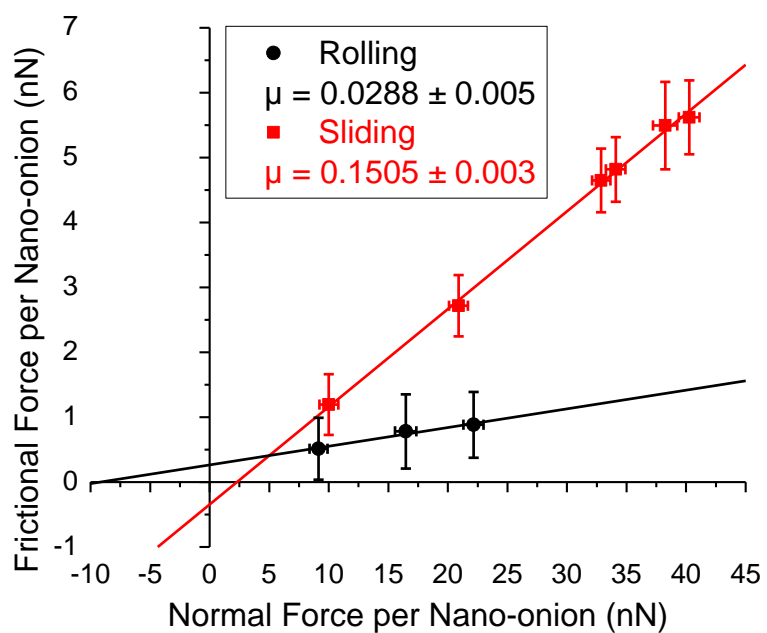


Figure 3-8. Load ramp for MD simulations with four nano-onions illustrating friction coefficients for rolling and sliding behavior.

## CHAPTER 4 MECHANICAL AND TRIBOLOGICAL RESPONSES OF AMORPHOUS CARBON NANOPARTICLES

Amorphous carbon (a-C) films, as a result of their unique mechanical and tribological properties, have attracted significant scientific and industrial interest for many applications, such as solid lubricants and wear-resistant coatings, over the past few decades [20, 117-120]. Different from the two crystalline phases of carbon, diamond and graphite, which are characterized by a  $sp^3$ - and  $sp^2$ -hybridized lattice, respectively, a-C materials are comprised of a mixture of predominantly  $sp^3$ - and  $sp^2$ -bonded carbon atoms as well as possible small amounts of  $sp$ -bonded carbons. Amorphous carbon films can be produced through a wide variety of deposition methods [121] which result in a-C materials with many different structural properties that can contain a range of hydrogenations from hydrogen-free up to about 60 atomic percent hydrogen (at.% H) [120, 122, 123]. For instance, a-C formed through the sputtering of graphite results in films that are mostly  $sp^2$ -hybridized (graphite-like); conversely, a-C made by mass-selected ion beam deposition results in films that are mainly  $sp^3$ -hybridized (diamond-like) [124]. As would be expected, the specific mechanical and tribological properties of individual a-C films varies greatly depending on the relative structural information, especially the  $sp^2:sp^3$  ratio and percentage of hydrogen content within the film [20-22, 120].

The mechanical properties of a-C films, such as hardness and elastic modulus, are dependent on the strength of the C-C bonds that comprise the network; as such, the hardness and moduli of a-C films are lower than those of diamond films due to the presence of  $sp^2$ -hybridized carbon and hydrogen within the structure [20]. Amorphous carbon films that contain high percentages of  $sp^3$ -hybridized carbon, typically referred to

as tetrahedral amorphous carbon (ta-C), exhibit higher density, hardness, and Young's modulus compared to other hydrogenated amorphous carbon (a-C:H) films. For example, one study by Ferrari *et al.* [125] indicated that a ta-C film with 88% sp<sup>3</sup>-hybridized carbon had a density and Young's modulus of 3.26 g/cc and 757 GPa, respectively; the same study also showed that a hydrogenated ta-C film with 70% sp<sup>3</sup>-hybridized carbon and 30 at.% H had a density of 2.35 g/cc and a Young's modulus of 300 GPa. Other a-C:H films with higher percentages of sp<sup>2</sup>-bonded carbon are less hard than ta-C films and have densities that vary from ~1.2 to 2.2 g/cc depending on the sp<sup>2</sup>:sp<sup>3</sup> ratio and the at.% H content [121].

The friction and wear performance of a-C:H films is affected not only by the sp<sup>2</sup>:sp<sup>3</sup> carbon ratio and hydrogen content but also by the conditions of the tribological system such as sliding speed, contact pressure, sliding distance, temperature, counterface material, and presence of water and oxygen in the test environment [21, 22, 119, 126]. As a result, it is not surprising that the range of friction coefficients for different a-C films that have been reported over the years is quite broad at ~0.001-0.7 [119]. In an inert or vacuum environment, a study by Erdemir [21] showed that highly hydrogenated a-C:H films had very low friction coefficients of ~0.003 while non-hydrogenated a-C films had high friction coefficients of ~0.65. The differences in the observed friction are generally attributed to the hydrogen passivation of unsaturated carbon atoms near the tribological interface which limits their ability to form strong bonds across the interface, which effectively reduces adhesion and friction [21, 22].

In a humid atmosphere, the study by Erdemir [21] demonstrated that the presence of humidity affected hydrogenated and non-hydrogenated a-C films differently.

Specifically, the friction coefficient obtained for the highly hydrogenated films increased from 0.003 to 0.06, whereas the non-hydrogenated films showed a decrease in coefficient of friction from 0.65 to 0.25. Experimental findings have further demonstrated that friction coefficients of less than 0.01 can be obtained for a-C:H films by producing atomically smooth films that reduces asperity-asperity interactions and by maximizing the chemical inertness of the interface, which limits adhesion and prevents the formation of chemical bonds across the tribological interface [119].

Another class of materials that has seen increasing interest for use in tribological systems as both solid films and as lubricant additives to base oils is nanoparticles [23, 25, 26, 35, 38, 103, 127, 128]. Nanoparticles, such as carbon nano-onions and inorganic fullerene-like nanoparticles which are discussed in detail in Chapters 3 and 5, respectively, are of interest in tribological applications because of their high degree of structural stability and chemical inertness; additionally, different types of nanoparticles have been shown to provide friction and wear reduction to contacting interfaces through a variety of mechanisms including rolling and sliding at the interface [25, 96, 104] as well as through the exfoliation of lubricious lamellar material within the contact [35, 41]. As lubricant additives, the small size of nanoparticles further enables them to be delivered directly to the sliding contact [46, 129], which is important for providing effective friction and wear reduction throughout the tribological process.

Considering the properties of nanoparticles that make them of interest for use in tribological systems, one question that remains to be answered is how the mechanical and tribological properties observed for a-C:H films translate to those of amorphous carbon nanoparticles. Here, we address this question through the use of classical

molecular dynamics (MD) simulations to investigate the mechanical and tribological responses of individual a-C nanoparticles as a function of nanoparticle size and percentage hydrogenation as they are subjected to compression and friction between hydrogen-terminated diamond surfaces in a perfect ultra-high vacuum environment.

### **Experimental Motivation**

Qualitative *in situ* nanocompression experiments were performed on individual a-C nanoparticles using a JEOL 2010F high resolution transmission electron microscope (HRTEM) fitted with a TEM-NanoIndenter from Nanofactory Instruments. These *in situ* HRTEM experiments were performed under the guidance of Dr. Lucile Joly-Pottuz and her graduate student, Emilie Calvié, at the Institut National des Sciences Appliquées de Lyon (INSA) in Lyon, France. The a-C nanoparticles used in the *in situ* experiments had diameters of approximately 150 nm and were synthesized during the plasma-assisted chemical vapor deposition of diamond-like carbon films. In these experiments, the a-C nanoparticles were deposited on a silicon substrate and subjected to compressive loads against a truncated diamond nanoindenter tip with a width of  $\sim 0.6 \mu\text{m}$ . During compression, it was observed that the a-C nanoparticles deformed in an entirely elastic/plastic manner with no abrupt fracture events occurring up to very high compressions. Figures 4-1A and 4-1B illustrate the behavior during and after loading, respectively, of an a-C nanoparticle that exhibited elastic deformation with no noticeable plastic deformation. Figure 4-1C, on the other hand, depicts the compression of an a-C nanoparticle to a much higher strain which resulted in clearly evident plastic deformation after unloading as is shown in Figure 4-1D. Since analysis of these *in situ* HRTEM experiments was performed qualitatively, MD simulations are presented here in order to

quantify the extent of elastic deformation during a-C nanoparticle compression as well as to determine the mechanisms involved in the observed elastic-to-plastic transition.

### **Computational Details**

For the MD simulations performed here, the short-range covalent and long-range van der Waals (vdW) interactions were calculated using the second-generation reactive empirical bond order (REBO) hydrocarbon potential [66] and a Lennard-Jones (LJ) 12-6 potential [71], respectively. In order to accurately simulate the amorphous character of a-C nanoparticles, we first heated a large, periodic system of crystalline diamond to a temperature of 8000 K. After allowing the system to become fully disordered, the system was rapidly quenched to 300 K at a rate of 100 K/ps; from this periodic amorphous carbon structure, spheres with diameters of 2, 3, 4, and 5 nm were extracted. In addition to these non-hydrogenated nanoparticles, partially hydrogenated nanoparticles were also formed. Since hydrogenated a-C:H films typically contain around 20-60 at.% H [22, 119, 120], we made hydrogenated a-C nanoparticles containing 25 and 50 at.% H with the same range of diameters as for the non-hydrogenated nanoparticles. Specifically, the hydrogenated nanoparticles were generated through the random distribution of hydrogen atoms to the unsaturated carbon atoms within the amorphous carbon structure until the desired 25 or 50 at.% H condition was met. After equilibration of each of these 0, 25, and 50 at.% H nanoparticles with diameters of 2, 3, 4, and 5 nm at 300 K, the composition and properties (i.e. carbon hybridization, diameter, and density) of the nanoparticles was determined and is indicated in Table 4-1; the densities for the nanoparticles were calculated assuming a perfectly spherical structure.

The mechanical and tribological properties of the a-C nanoparticles were investigated by performing compression and friction simulations with individual a-C nanoparticles positioned between hydrogen-terminated (111) diamond substrates as is shown in Figure 4-2. Each of the simulations involved periodic boundaries applied in the plane parallel to the a-C/diamond interface and was controlled by the rigid displacement of the outermost ~8% of each of the diamond substrates; temperatures were maintained at 300 K by applying a Langevin thermostat [71] to the carbon atoms within the ~11% of each substrate nearest to the rigid atoms. The remaining atoms within each system were permitted to evolve freely according to Newton's equations of motion.

For each a-C nanoparticle diameter and hydrogenation considered, the compression simulations were carried out at a compressive rate of 10 m/s. During compression, the evolution of normal load was determined as a function of nanoparticle strain which was calculated relative to the change in nanoparticle diameter,  $\Delta d$ , as is illustrated in Figure 4-3. In order to calculate the stress as a function of strain, a circular a-C/diamond contact was assumed. The real contact radius,  $r_c$  (Figure 4-3), was approximated by determining which nanoparticle atoms were within 0.34 nm of the diamond substrate atoms. Since most of the atoms along the surface of the nanoparticles were no more than  $sp^2$ -hybridized, the value of 0.34 nm was used since it is the approximate layer separation in  $sp^2$ -graphite [130].

Friction simulations were performed with the 2 and 4 nm diameter nanoparticles at each hydrogenation considered in order to determine the influence of nanoparticle size and hydrogen content on tribological performance. From the compression simulations, apparent contact pressures of between about 1 and 2.5 GPa were selected for the

tribological simulations which were performed at a rate of 10 m/s for a distance of 20 nm. The contact pressures were determined from the apparent contact area of the periodic diamond substrates, which was  $\sim 9.25$  and  $\sim 37$  nm<sup>2</sup> for the 2 and 4 nm diameter nanoparticles, respectively.

## **Mechanical Response during Compression**

### **Nanocompression Simulations**

During the uniaxial compression of the individual a-C nanoparticles, it was observed that the evolution of compressive force with increasing strain was relatively unaffected by the presence of hydrogen within the nanoparticles as is demonstrated in Figure 4-4A. In order to quantitatively compare the mechanical properties of the a-C nanoparticles with different diameters, we measured the approximate contact area as a means of determining the contact stress as a function of strain during the compression of each a-C nanoparticle; the results of this analysis are shown in Figure 4-4B. Since the slope of the stress versus strain curves at low percentages of strain represent the combined elastic modulus of the (111) diamond/a-C nanoparticle system, it was found that the a-C nanoparticles had comparable elastic moduli at all diameters and hydrogenations considered here. The fluctuations in the measured contact stresses during the compression simulations, as depicted in Figure 4-4B, were largely a result of the approximation of the real contact area. Due to the small size, amorphous character, and not perfectly spherical shape of the a-C nanoparticles, the geometry of the real contact area at any given point during the simulations was, rather than being truly circular, continually changing throughout the compression. As such, the measurement of the real contact area while assuming a circular contact resulted in regions of both over- and under-approximations of the true contact areas during compression.

This finding that the mechanical properties of the a-C nanoparticles were unaffected by the addition of partial hydrogenation (Figure 4-4) was in agreement with expectations since the mechanical properties of amorphous carbon materials depend on the strength of their individual bonds [20]. Although C-H bonds are strong, they do not impact the mechanical response of the a-C nanoparticles since the bonding network is terminated at the C-H bond [120]. If the hydrogen atoms were neglected, the internal C-C network of the a-C nanoparticles with 0, 25, and 50 at.% H were structurally similar; specifically, the ratio of carbon atoms with three and four carbon neighbors were nearly the same. Therefore, since the properties of the C-C network control the measured mechanical properties, the a-C nanoparticles were found to display mechanical behaviors that were relatively independent of diameter and hydrogenation over the range included in this work.

### **Mechanisms in Elastic to Plastic Transition**

In order to determine the elastic or plastic nature of the nanoparticles during compression, the compression simulations were reversed and unloaded at a rate of 10 m/s; however, at higher percentages of strain, strong interfacial bonds were formed between the (111) diamond substrates and the a-C nanoparticles as is illustrated in Figure 4-5 for the 3 nm diameter nanoparticle with 0 at.% H during unloading after a maximum strain of ~37%. Since the formation of these strong covalent bonds affected the ability to quantify the amount of plasticity that occurred during each nanoparticle compression, a new method of nanoparticle relaxation was required. This was accomplished by removing the (111) diamond substrates and allowing each nanoparticle to relax in full vacuum for sufficient time such that the nanoparticle's diameter (Figure 4-3) was no longer changing. In this manner, each a-C nanoparticle

was relaxed at numerous percentages of strain ranging from ~10 to 55% in order to determine the onset of plastic deformation in the a-C nanoparticle compression simulations.

Figure 4-6A illustrates the percentage strain of the a-C nanoparticles after relaxation relative to the maximum strain prior to relaxation. From this analysis, it was observed that the a-C nanoparticles demonstrated roughly the same elastic/plastic response despite changes in diameter and hydrogenation. In particular, the a-C nanoparticles were found to recover elastically up to strains of between ~18 to 22% for most of the nanoparticles considered here. This relatively high elasticity is in good agreement with previous simulations involving the REBO potential to investigate the nanoindentation of an a-C:H film [124]; this study showed that the a-C:H film recovered elastically and exhibited minimal change in the internal bonding character after a maximum indentation depth of 20% of the total a-C:H film thickness. For the a-C nanoparticles above ~18 to 22% strain, noticeable plastic deformation was observed as is indicated by the steep rise in final strain with increasing initial strain in Figure 4-6A. It should be noted that the fluctuations and spread in Figure 4-6A is primarily a result of difficulties in determining the exact strain of these small nanoparticles during the compression and relaxation simulations; for instance, a change of 1% strain for a 2 nm and 5 nm diameter nanoparticle is equivalent to a diameter change of only 0.02 and 0.05 nm, respectively.

To determine the source of the transition from elastic to plastic deformation demonstrated in Figure 4-6A, the changes in the internal C-C bonding network were analyzed by quantifying the number of carbon atoms which form new C-C bonds during

compression; the formation of new C-C bonds was determined by using a radial interatomic distance cutoff of 0.185 nm. From this analysis, it was found that the onset of plastic deformation corresponded with a simultaneous increase in the formation of new C-C bonds as is indicated in Figure 4-6B. It was determined that the nanoparticles showed close to the same percentage increase in C-C bond formations for a given hydrogen content for all the diameters considered here. In addition, increasing the at.% H content of the a-C nanoparticles resulted in a higher percentage of initial strain being necessary to obtain equivalent increases in C-C bond formations as lesser hydrogenated nanoparticles; this was because the presence of C-H bonds within the nanoparticles led to fewer available carbon sites for C-C bonds to form. These C-C bond formations during compression are illustrated in Figure 4-7 which shows cross-sectional snapshots of the 4 nm diameter nanoparticles at each hydrogenation considered and at increasing initial strains. In these images, the increase in the number of carbon atoms which form new C-C bonds, particularly with increasing plastic deformation, is clearly visible. As stated previously, the mechanical properties of amorphous carbon materials are dependent on the strength of the bonds that make up the internal network [20]. To this effect, it is not surprising that the formation of new C-C bonds within the a-C nanoparticles during compression coincided with an increase in plastic deformation after relaxation. Since the formation of new C-C bonds results in an increase in the cross-linking between the carbon atoms that comprise the internal network, the compressed a-C nanoparticles were unable to fully recover when new C-C cross-links were formed.

## Tribological Properties

Classical MD simulations of friction of the 2 and 4 nm diameter a-C nanoparticles predicted that the tribological behavior was significantly affected by the amount of hydrogen present in the nanoparticle as is indicated in Figure 4-8. For each nanoparticle with 0 at.% H, the presence of large numbers of under-coordinated carbon atoms along the periphery of the nanoparticle resulted in numerous interfacial bond formations between the nanoparticle and the (111) diamond substrates which led to very high friction forces as is evident in Figure 4-8A. The presence of 25 and 50 at.% H in the a-C nanoparticles served to passivate many of the unsaturated surface carbon atoms which led to fewer initiation points for interfacial covalent bonding to occur during friction; this reduction in interfacial bonding resulted in the lower friction forces indicated in Figures 4-8B and 4-8C.

The friction load ramps for each of the a-C nanoparticle systems were generated through analysis of the normal and frictional forces during the tribological simulations and are shown in Figure 4-9. From this analysis, some differences in the tribological behavior resulting from changes in the nanoparticle diameter (2 and 4 nm) were predicted, in addition to the effect of hydrogenation; it should be noted here that the tribological simulations of a-C nanoparticles with 0 at.% H during which significant interfacial bonding occurred were omitted from the friction load ramps in Figure 4-9 since the fluctuation in the normal and frictional forces (Figure 4-8A) were too severe to accurately measure a coefficient of friction. For the 2 nm diameter nanoparticles, the presence of 25 and 50 at.% H resulted in no interfacial bond formations during friction in all but one of the simulations that were performed. The absence of interfacial bonds enabled the a-C nanoparticles to roll within the interface providing a very low friction

coefficient of  $\sim 0.019$  as is shown in Figure 4-9A. Regarding the two data points indicated in Figure 4-9A at lower normal forces, interfacial covalent bonds were formed during these simulations which forced the nanoparticles to slide along the interface resulting in an increase in the friction forces relative to the other systems where rolling occurred; this observation of an increase in friction when the tribological behavior transitioned from rolling to sliding is the same as previously discussed in Chapter 3 during the friction of carbon nano-onions.

For the 4 nm diameter nanoparticles, the addition of 25 and 50 at.% H significantly reduced the formation of interfacial bonds during friction, but some covalent bonds still formed resulting from the larger surface area of the nanoparticles and, subsequently, higher number of potential initiation points for bonding relative to the 2 nm diameter nanoparticles. The presence of interfacial covalent bonding during friction of the 4 nm diameter a-C nanoparticles limited the amount of rolling behavior and, as is illustrated in Figure 4-9B, led to an increase in coefficient of friction, as compared to the 2 nm diameter nanoparticles in Figure 4-9A. In particular, more interfacial bonds were formed between the (111) diamond substrates and the 4 nm diameter a-C nanoparticles in the 25 at.% H systems than in the 50 at.% H systems. As such, the friction forces in the 25 at.% H systems (Figure 4-8B) were generally higher than the friction forces in the 50 at.% H systems (Figure 4-8C). In the 25 at.% H systems, the more frequent occurrence of interfacial bonding caused the a-C nanoparticles to predominantly slide within the interface with some regions of rolling occurring as well, which resulted in a higher friction coefficient of  $\sim 0.088$  as is shown in Figure 4-9B. On the other hand, the lesser interfacial bonding in the 50 at.% H systems enabled the a-C nanoparticles to

exhibit more rolling behavior than in the previous case resulting in a lower coefficient of friction of  $\sim 0.045$ .

The observed influence of hydrogenation on the tribological properties of the a-C nanoparticles is in good agreement with experimental [21, 126] and theoretical [22, 65, 111] findings for various a-C films. As discussed previously, it has been experimentally demonstrated that chemical interactions between sliding a-C interfaces, such as covalent bonding between unoccupied  $\sigma$ -bonds near the interface, significantly influences friction leading to large variations in the coefficient of friction for different types of a-C:H films ranging from  $\sim 0.001$  to 0.7 [119]. Tribological MD simulations of a-C:H films with different hydrogenations have shown that hydrogen passivates the unsaturated sp- and sp<sup>2</sup>-bonded carbon atoms at the sliding interface providing a reduction of friction [22, 65, 111]. In these studies, the unsaturated carbon atoms provide the initiation points for interfacial bonding to occur during friction; subsequently, an increase in interfacial bonding between the a-C:H films was shown to result in an increase in the measured friction, which is the same observation for the a-C nanoparticles presented here. The lowest friction coefficient for the a-C nanoparticles was found to be  $\sim 0.019$  for the 2 nm diameter nanoparticles with 25 and 50 at.% H when no interfacial bonding occurred, while the highest friction coefficient was  $\sim 0.088$  for the 4 nm diameter nanoparticles with 25 at.% H which indicated the largest number of interfacial bond formations during friction for the partially hydrogenated nanoparticles considered here.

### **Summary**

The classical MD simulations presented here investigated the mechanical and tribological responses of individual a-C nanoparticles with varying diameters and

hydrogenations when subjected to externally applied forces between (111) diamond surfaces. The results of nanocompression simulations indicated that changes in diameter and/or at.% H content had no discernible effect on the mechanical response since only the C-C bonds, and not the C-H bonds, contributed to the mechanical properties of the nanoparticles. After relaxation of the nanoparticles at strains ranging from ~10 to 55%, it was shown that the nanoparticles exhibited a transition from elastic to plastic behavior brought about by the formation of new, cross-linking C-C bonds within the nanoparticles.

Friction simulations indicated that the tribological properties of the a-C nanoparticles were dependent on both the diameter and hydrogen content. Specifically, increased hydrogenation provided passivation for the unsaturated carbon atoms at the surface of the nanoparticles which limited covalent bond formations between the nanoparticles and the (111) diamond substrates during friction. Numerous interfacial bond formations for the non-hydrogenated nanoparticles resulted in very high friction forces, whereas the 2 nm diameter nanoparticles with 25 and 50 at.% H had a low friction coefficient of ~0.019 in the absence of interfacial bonding. The 4 nm diameter nanoparticle systems displayed more interfacial bond formations than the 2 nm diameter nanoparticles resulting from the larger surface area and higher number of unsaturated carbon atoms; this resulted in an increase in coefficient of friction for the 4 nm diameter nanoparticles at ~0.045 for the 50 at.% H nanoparticles and ~0.088 for the 25 at.% H nanoparticles. These results indicate the ability for a-C nanoparticles to provide low friction coefficients in tribological systems; however, since the formation of interfacial covalent bonds causes an increase in measured friction, a high degree of

chemical passivation of the nanoparticle's surface is necessary for optimal tribological conditions to be obtained.

Table 4-1. Composition and properties of amorphous carbon nanoparticles.

At.% H content	Total C	Total H	Diameter (nm)	Density (g/cc)	sp (%)	sp <sup>2</sup> (%)	sp <sup>3</sup> (%)	sp <sup>2</sup> :sp <sup>3</sup> ratio
0	735	0	1.98	2.82	15.65	66.12	18.23	3.63:1
25	735	180	2.18	2.20	11.84	54.83	33.33	1.64:1
50	735	368	2.19	2.22	7.89	44.08	48.03	0.92:1
0	2492	0	3.03	2.90	11.76	69.46	18.78	3.70:1
25	2492	621	3.22	2.49	9.83	55.62	34.55	1.61:1
50	2492	1238	3.38	2.21	5.58	40.01	54.41	0.74:1
0	5914	0	4.03	3.04	7.70	72.30	20.00	3.61:1
25	5914	1473	4.29	2.59	6.99	53.91	39.10	1.34:1
50	5914	2935	4.34	2.56	4.19	39.86	55.95	0.71:1
0	11534	0	5.05	3.09	6.50	73.14	20.36	3.59:1
25	11534	2877	5.28	2.77	5.65	54.52	39.83	1.37:1
50	11534	5737	5.49	2.52	3.72	39.48	56.80	0.70:1

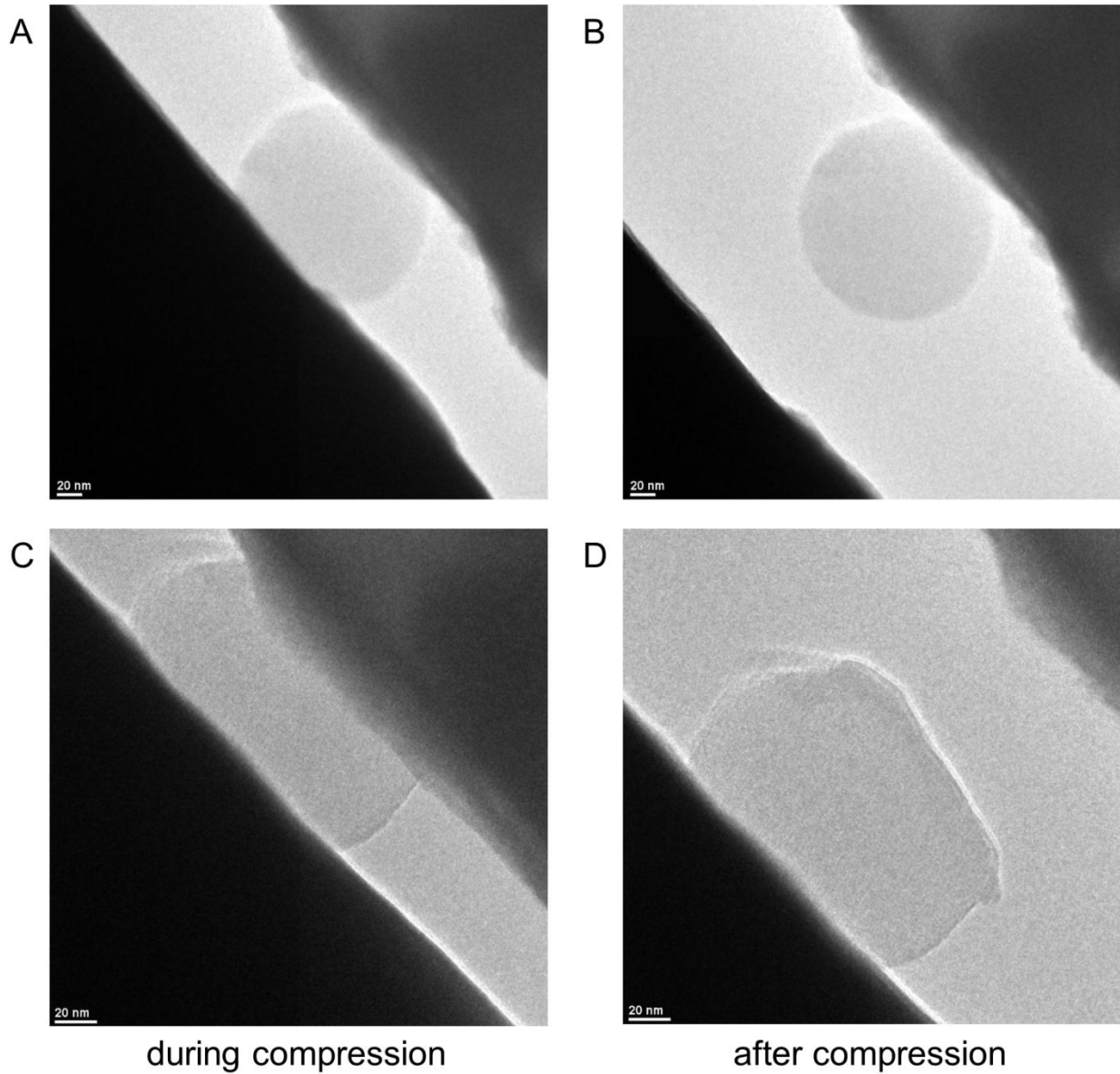


Figure 4-1. HRTEM images of ~150 nm diameter a-C nanoparticles from *in situ* experiments A) during and B) after compression with elastic deformation and C) during and D) after compression with plastic deformation. Scale bars are 20 nm.

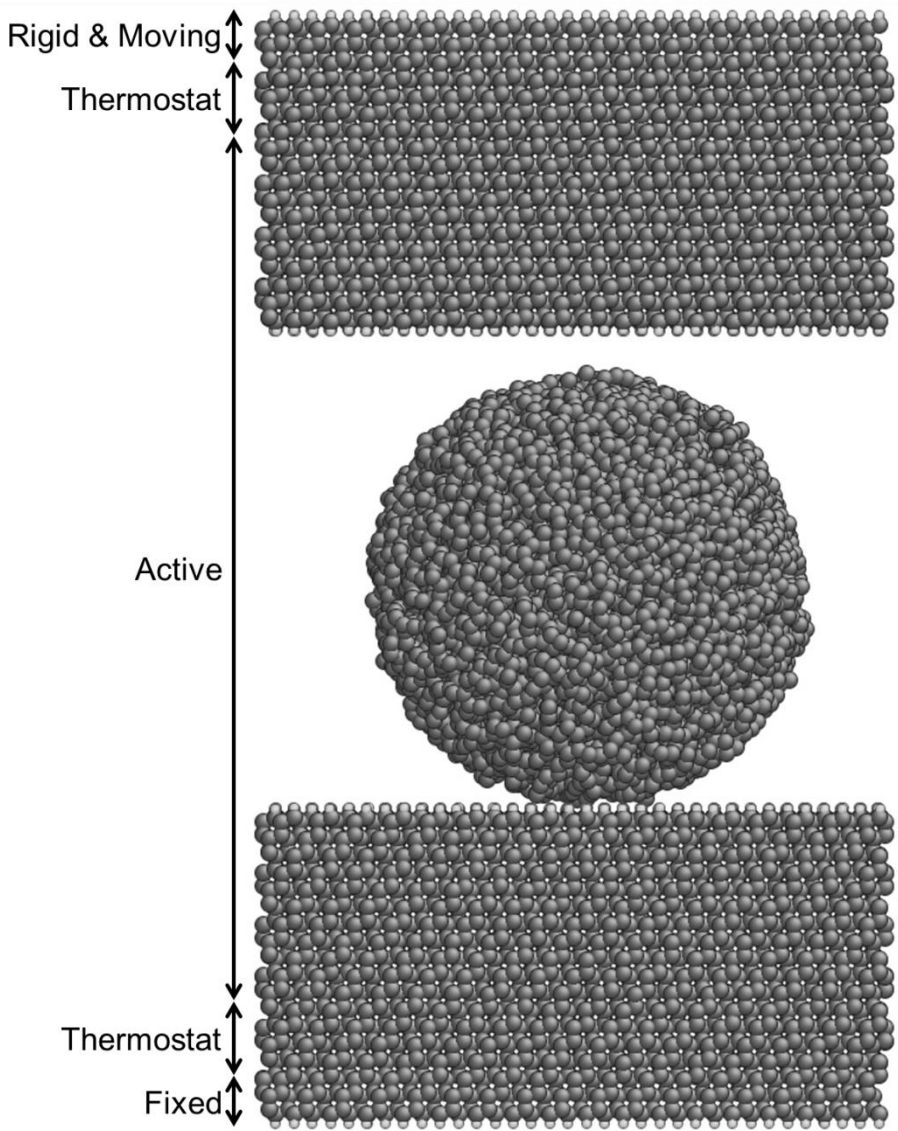


Figure 4-2. Snapshot of initial system showing 5 nm diameter and 0 at.% H a-C nanoparticle between H-terminated (111) diamond substrates. Regions of rigid and moving, fixed, thermostat, and active atoms are indicated. Dark atoms are C and light atoms are H.

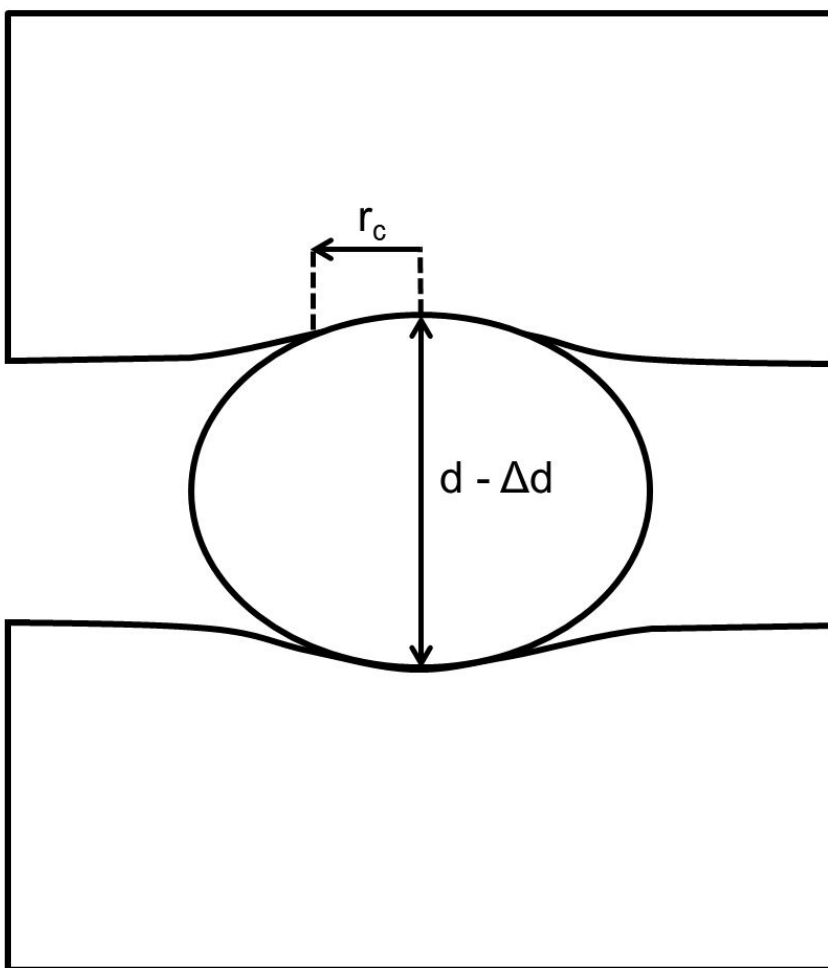


Figure 4-3. Schematic of a-C nanoparticle compression illustrating definition of real contact radius,  $r_c$ , and change in diameter,  $d$ .

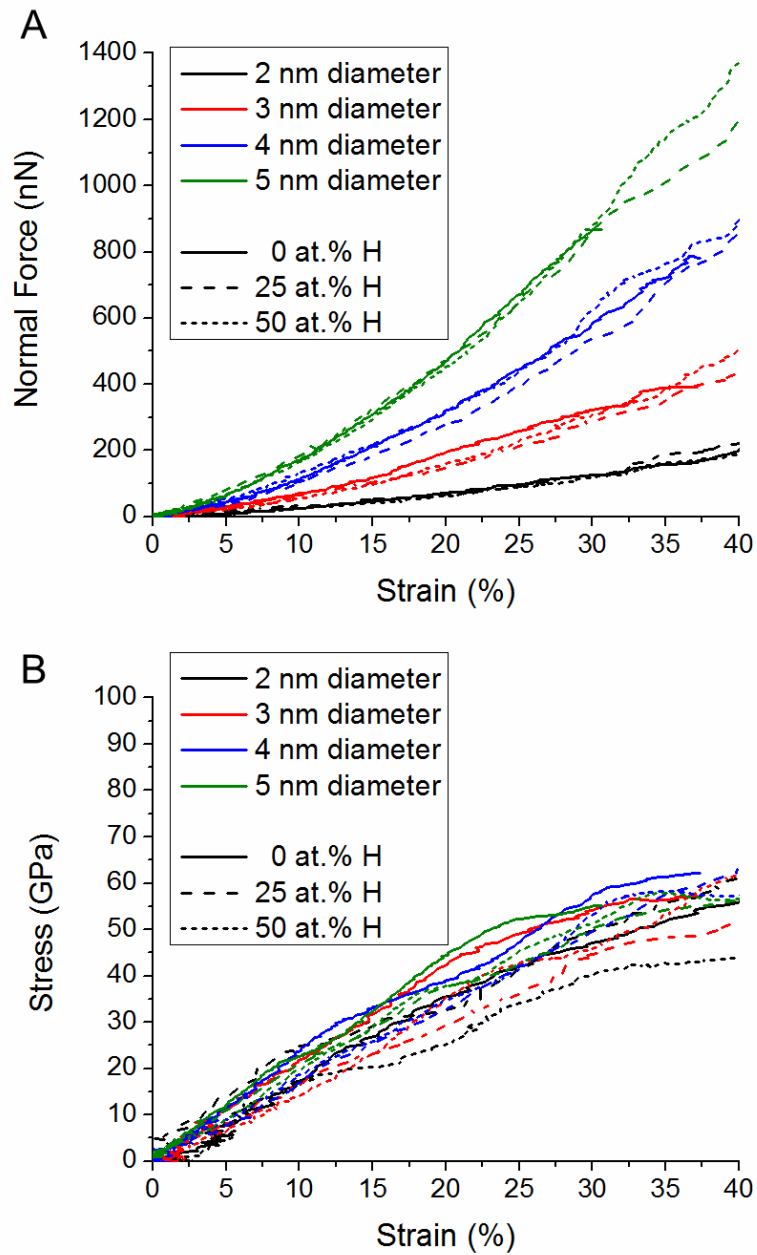


Figure 4-4. Evolution of A) compressive force and B) approximate contact stress as a function of percentage strain during nanoparticle compression.

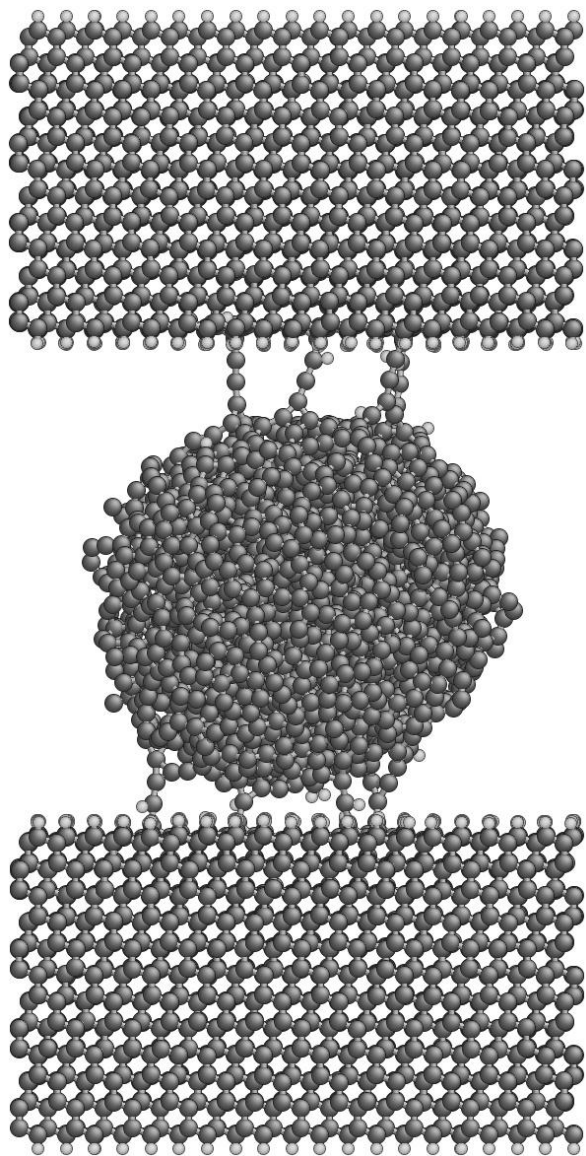


Figure 4-5. Snapshot of strong interfacial bond formations during unloading of 3 nm diameter a-C nanoparticle with 0 at.% H from a maximum strain of ~37%.

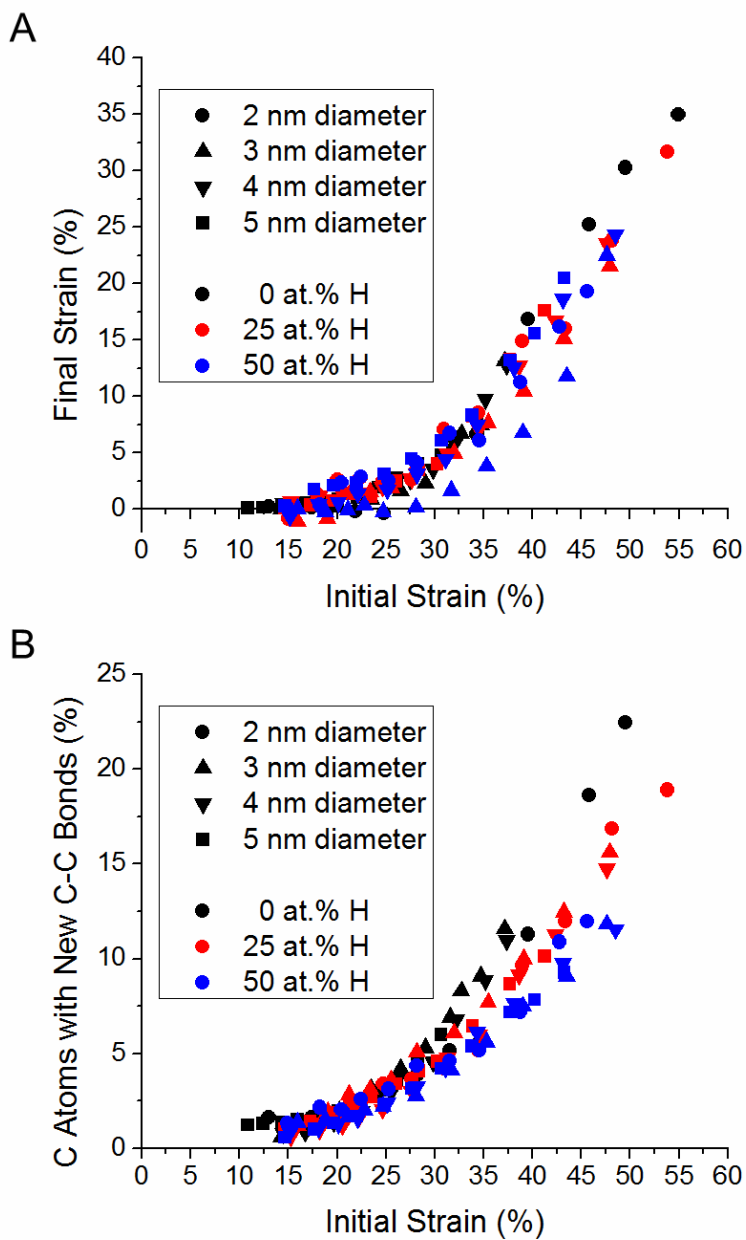


Figure 4-6. Analysis of nanoparticle deformation indicating A) final strain after nanoparticle relaxation and B) percentage of carbon atoms forming new C-C bonds as a function of percentage strain during nanoparticle compression.

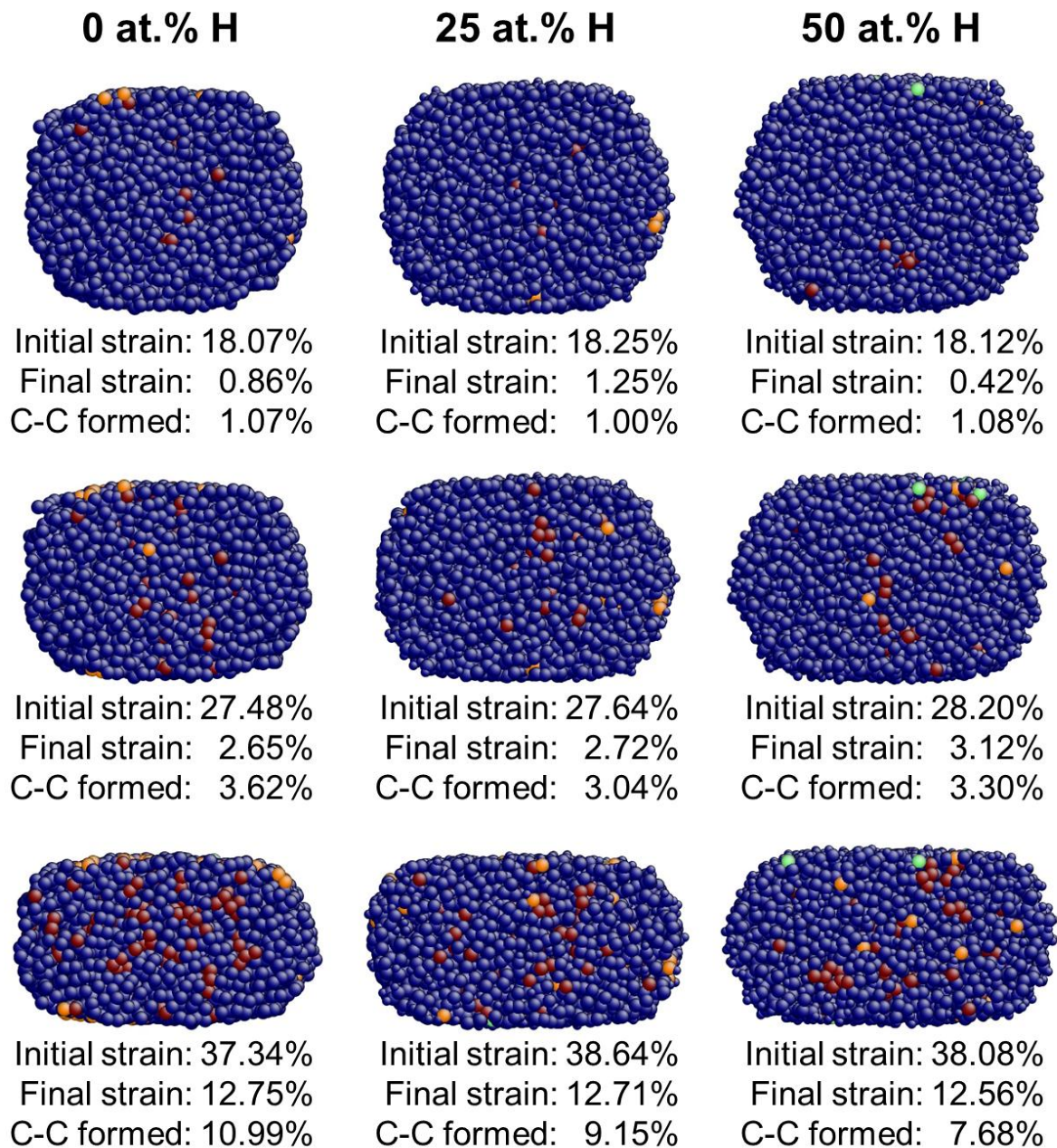


Figure 4-7. Cross-sectional snapshots of compressed 4 nm diameter nanoparticles with 0, 25, and 50 at.% H indicating the percent strain before and after relaxation as well as the percentage of C atoms which formed new C-C bonds during compression. Blue atoms are C which did not form new C-C bonds. Other colors represent C atoms which formed new C-C bonds where red atoms have 4 C neighbors, orange atoms have 3 C neighbors, and green atoms have 2 C neighbors.

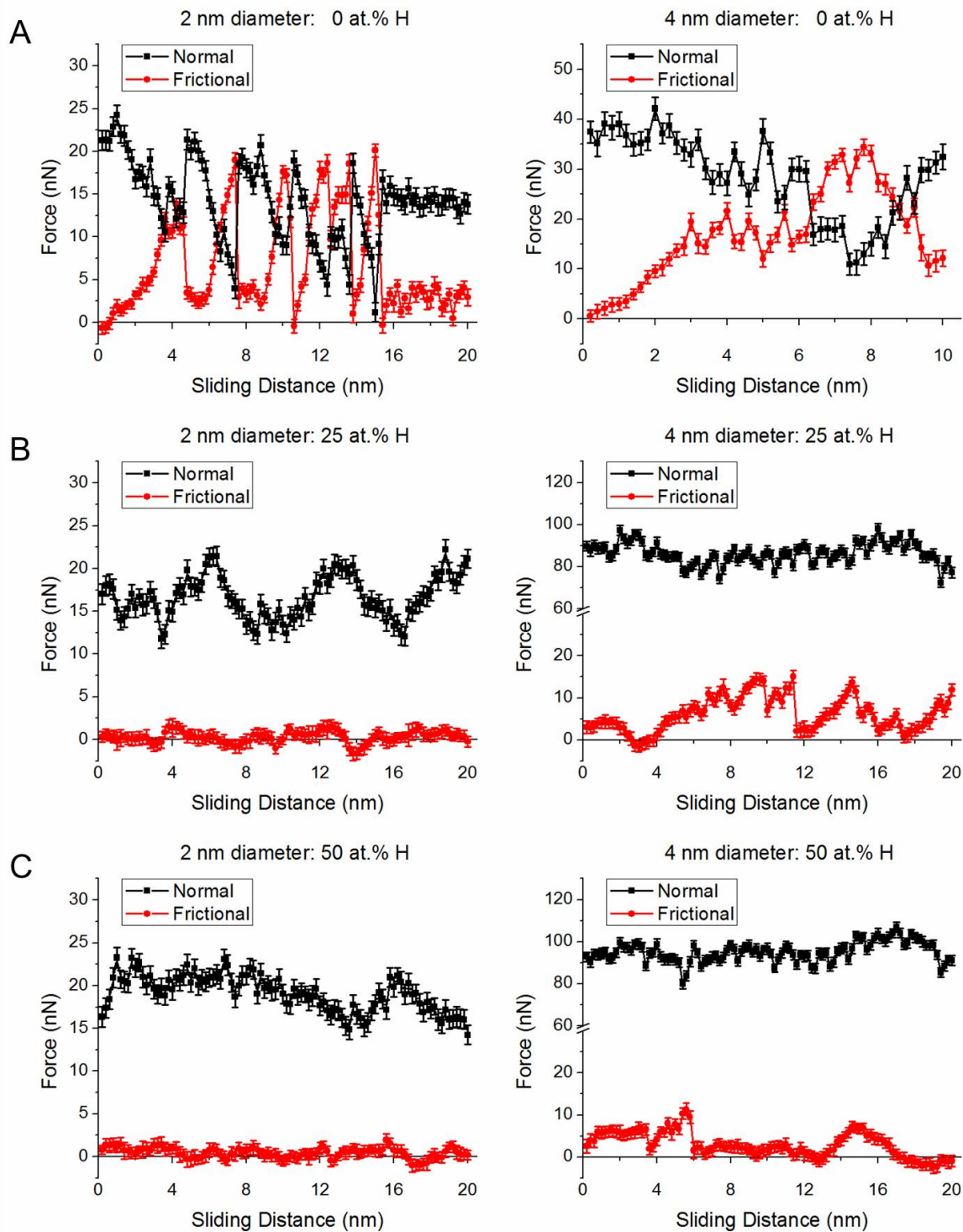


Figure 4-8. Frictional and normal forces during friction simulations for 2 and 4 nm diameter a-C nanoparticles with A) 0 at.% H, B) 25 at.% H, and C) 50 at.% H.

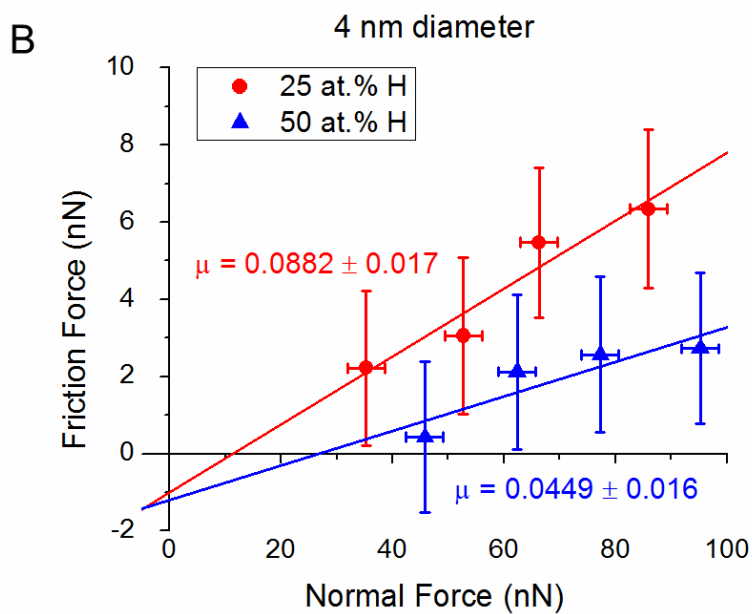
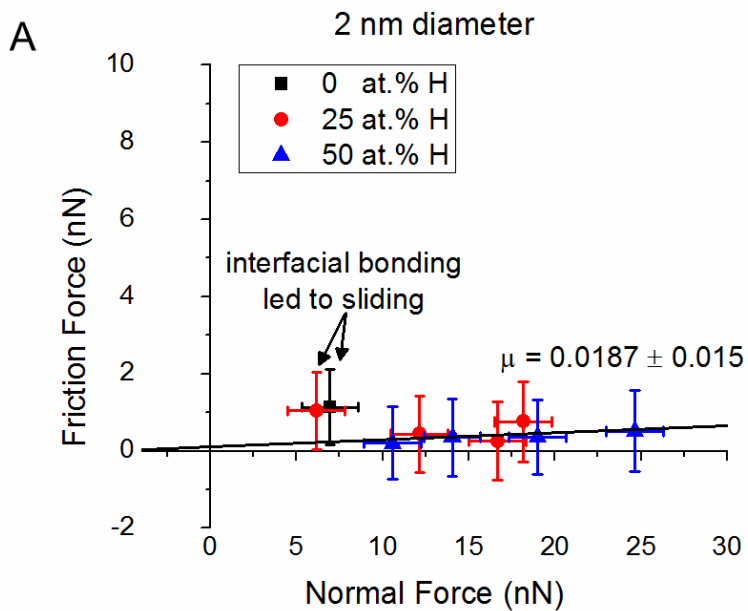


Figure 4-9. Load ramps from friction simulations for a-C nanoparticles with diameters of A) 2 nm and B) 4 nm.

## CHAPTER 5 STRUCTURAL INFLUENCE ON LUBRICATION MECHANISMS OF FULLERENE-LIKE MOLYBDENUM DISULFIDE NANOPARTICLES

The synthesis of inorganic fullerene-like (IF) nanoparticles made of metal dichalcogenide,  $WS_2$ , was first reported by Tenne *et al.* in 1992 [131]. These IF-like nanoparticles, predominantly  $WS_2$  and  $MoS_2$ , have been successfully shown to provide good friction and wear reduction when used either as solid lubricants [23, 128] or as lubricant additives to base oils [35, 129]. Under boundary lubrication conditions, studies using polished AISI 52100 steel counterfaces have indicated that only 1 wt.% of IF- $WS_2$  or IF- $MoS_2$  nanoparticles added to a polyalphaolefin (PAO) base oil is necessary for a reduction of friction coefficient between 40 and 70% relative to PAO without any additive [129, 132]. These IF additives are efficient in these applications since their small size and chemically inert closed-shell structure enables them to be delivered directly to the moving interface to provide effective friction reducing and anti-wear properties from the beginning of the tribological process.

The friction and wear reducing properties of IF nanoparticles are typically ascribed to the exfoliation of the external sheets of the nanoparticles during friction and uniaxial pressures resulting in the transfer of these lubricious sheets to the contacting surface asperities [35, 41, 133]. However, further studies have indicated that the observed friction and wear performance varies depending on the structural properties of the IF nanoparticles such as their size, shape, and degree of crystallinity. For instance, it has been observed that IF nanoparticles with lower crystallinity have improved lubricating properties [132, 134]. From this finding, it was proposed that the amorphous nature of these less crystalline nanoparticles results in a large number of point defects and grain boundaries leading to easier exfoliation during friction. Other proposed lubrication

mechanisms have suggested that, even if the lamellar exfoliation is the predominant mechanism during friction, a rolling process could be involved for well-crystallized and more spherical nanoparticles [135].

To better understand and quantify the mechanisms that occur when IF nanoparticles are in tribological contact with sliding surfaces, it is necessary to visualize the behavior of individual nanoparticles in real time while they are undergoing externally applied forces. Modern advancements in *in situ* electron microscopy have made these real time observations possible. Tevet *et al.* [48] reported on the stiffness and failure strengths of individual IF nanoparticles during *in situ* nanocompression studies within a high resolution scanning electron microscope (HRSEM). The findings showed that the stiffness and compression failure strength of these nanoparticles are highly variable depending on the size and faceted nature of each individual particle. However, due to their small size and layered morphology, the IF nanoparticles were able to withstand very high elastic stress with compression failure strengths ranging between 1 and 2.5 GPa. More recently, Lahouij *et al.* [46, 136] visualized the *in situ* behavior of individual IF-MoS<sub>2</sub> nanoparticles using a transmission electron microscope (TEM) and a high resolution TEM. In these studies, the authors concluded that the IF-MoS<sub>2</sub> nanoparticles can exhibit a rolling friction process at low contact pressures of less than ~100 MPa. As contact pressures increased, sliding became the dominant mechanism along with the beginnings of friction induced exfoliation of the external MoS<sub>2</sub> sheets. Even higher contact pressures of at least 1 GPa were necessary for the complete delamination of the nanoparticles. Despite these sophisticated experimental studies, the very small sizes of IF nanoparticles make distinguishing the specific structural

properties that impact the lubrication mechanism a difficult task; thus, a computational approach provides complementary insights since it allows the effect of specific structural changes on the observed mechanisms to be predicted.

Here, MD simulations were used to investigate the mechanical and tribological properties of individual IF-MoS<sub>2</sub> nanoparticles with either curved or faceted structures. The effect of structural and orientation changes on the observed rolling, sliding, and exfoliation of IF-MoS<sub>2</sub> nanoparticles when subjected to external compression and shear forces is investigated.

### **Computational Details**

For the classical MD simulations performed in this study, the short-range interactions and the long-range vdW interactions were calculated using a Tersoff-type Mo-S potential [70] and a Lennard-Jones (LJ) 12-6 potential [71], respectively, which are described in detail in Chapter 2. Two configurations of IF-MoS<sub>2</sub> nanoparticles with three nested layers each were used for the simulations carried out here. The first structure was a curved, ellipsoidal nanoparticle made up of 14365 atoms with major and minor diameters of about 9.5 and 6.3 nm, respectively, as is illustrated in Figure 5-1A. The second nanoparticle was a fully faceted nano-octahedron with 8856 atoms and edge lengths of around 6.2 nm, as is illustrated in Figure 5-1B. Although these structures are smaller than typical nanoparticles observed experimentally, their geometries balance realistic representation of experimental systems with computational efficiency. Additionally, the nano-octahedron was selected for the faceted configuration based on experimental observations of three-layer MoS<sub>2</sub> nano-octahedra with comparable dimensions [96].

In these simulations, the IF-MoS<sub>2</sub> nanoparticles were individually subjected to compressive and friction forces between sulfur-terminated (110) BCC molybdenum substrates. Furthermore, the ellipsoidal particle was positioned on both its major and minor axes in order to demonstrate the effects of nanoparticle orientation on the observed mechanical and tribological responses. With periodic boundaries applied in the plane parallel to the interface, the IF-MoS<sub>2</sub> systems were compressed at a rate of 10 m/s and at a temperature of 300 K. During the simulations, the evolution of the percentage of compression was analyzed with respect to the contact pressure which was approximated using the areas of the periodic substrates of ~128 nm<sup>2</sup> and ~162 nm<sup>2</sup> for the ellipsoid on its major and minor axis orientations, respectively, and ~110 nm<sup>2</sup> for the nano-octahedron. Contact pressures of up to approximately 2 GPa were then selected for the friction simulations which were done at a sliding rate of 10 m/s for a distance of 20 nm. Specifically, each simulation was controlled by the rigid displacement of the outermost 0.45 nm of the BCC Mo substrates with the temperatures maintained using Langevin thermostats [71] positioned on the 0.9 nm of the BCC Mo substrates nearest to the rigid atoms.

### **Nanocompression Simulations**

The progression of the uniaxial compression for each of the IF-MoS<sub>2</sub> nanoparticle systems is provided in Figures 5-2 through 5-5. For the nano-octahedron, the near-vertical orientation of the MoS<sub>2</sub> walls at the interface, as is shown in Figure 5-2A, resulted in a very high stiffness; the evolution of percent compression with apparent contact pressure is illustrated in Figure 5-2F. With this orientation, the sharp increase in contact pressure during compression is expected due to the large  $c_{11}$  for MoS<sub>2</sub> relative to the  $c_{33}$ , 238 and 52 GPa [137], respectively. During the early stages of compression,

the nano-octahedron resisted deformation while maintaining its initial structure (Figures 5-2B and 5-2C). At ~8% compression, as shown in Figure 5-2B, the contact pressure was ~0.8 GPa. When the compression increased to ~15% in Figure 5-2C, the contact pressure increased to ~2.0 GPa. Above this point, the nano-octahedron began to collapse during increasing compression; this process is demonstrated in Figure 5-2D which corresponds to ~30% compression and a contact pressure of ~2.3 GPa. As shown in Figure 5-2E, the contact pressure at ~40% compression decreased from the previous value to ~1.8 GPa. This decrease in contact pressure during additional compression (Figure 5-2F) is a result of rupturing of the facet edges which is illustrated in Figure 5-3. Above 40% compression, the hollow center of the nano-octahedron had collapsed resulting in a steep increase in contact pressure on additional loading.

The behavior of the MoS<sub>2</sub> ellipsoidal nanoparticle oriented along its minor axis during compression (Figure 5-4) was significantly different than that of the octahedral nanoparticle. When compressed along its minor diameter, the ellipsoidal nanoparticle displayed a very low stiffness resulting from the gradual size reduction of the hollow center during loading as is illustrated in Figures 5-4B through 5-4D. Figure 5-4B corresponds to ~20% compression at a contact pressure of ~0.25 GPa according to Figure 5-4F. From here, increasing the compression to ~30%, as is indicated in Figure 5-4C, only increased the contact pressure to ~0.37 GPa. At a contact pressure of ~0.65 GPa and ~43% compression (Figure 5-4D), the upper and lower MoS<sub>2</sub> layers came into contact causing the hollow core to disappear. Since the MoS<sub>2</sub> layers were in contact, further compression resulted in only a gradual increase in the percentage of compression, but there was also a substantial increase in pressure, as indicated in

Figure 5-4E, which corresponds to ~50% compression and a contact pressure of ~6 GPa. This predicted behavior is consistent with the sharp increase in contact pressure observed at the end of the nano-octahedron compression (Figure 5-2F). From the compression of the ellipsoidal nanoparticle along its minor axis, it was predicted that structural integrity was maintained throughout with no localized failure occurring.

The compression of the ellipsoidal nanoparticle oriented along its major axis is illustrated in Figure 5-5. During these simulations, the 90° rotation of the nanoparticle relative to the compression along the minor diameter resulted in an increase in stiffness, as is illustrated in Figure 5-5F. Initially, this orientation was characterized by a strong curvature of the MoS<sub>2</sub> walls at the upper and lower portions of the nanoparticle, which is shown in Figure 5-5A. The early stages of compression were characterized by the flattening of these upper and lower areas along with the gradual expansion of the minor axis; this behavior is demonstrated in Figure 5-5B, which corresponds to ~15% compression and a contact pressure of ~0.75 GPa. At a compression of ~25%, which corresponds to a contact pressure of ~1.3 GPa (Figure 5-5C), it was predicted that the major and minor diameters of the nanoparticle were nearly equivalent. At ~37% compression at a contact pressure of ~2.1 GPa, which is shown in Figure 5-5D, the internal structure of the nanoparticle had collapsed resembling a dumbbell configuration with two hollow cores on each side of the nanoparticle. Figure 5-5E corresponds to a compression of ~45% and a contact pressure of ~2.2 GPa. At this point, a rupturing of the outer wall occurred causing a decrease in the applied contact pressure that is similar to the observations during compression of the nano-octahedron shown in Figure 5-2F.

The nanocompression simulations results indicate that changes in both the structure and orientation of IF-MoS<sub>2</sub> nanoparticles within a contact cause significant changes in the mechanical response. For the ellipsoidal nanoparticle oriented along the minor axis, it can be concluded that this system exhibited the lowest stiffness until the nanoparticle walls became a layered stacking of MoS<sub>2</sub>. Alternatively, the highest observed stiffness belonged to the nano-octahedron which is consistent with the differences in compression of lamellar MoS<sub>2</sub> in directions perpendicular and parallel to the layers, respectively. Furthermore, the absence of localized failure during the compression of the ellipsoidal nanoparticle oriented on its minor axis along with the presence of rupturing at the facet edges in the nano-octahedron indicates that IF-MoS<sub>2</sub> nanoparticles preferentially exfoliate at grain boundaries and other similar defect locations at the periphery of the individual nanoparticles. Although rupturing of the outer wall was predicted during compression of the ellipsoidal nanoparticle aligned along its major axis, this particular orientation is unlikely within a real tribological contact since the nanoparticle will realign on its minor axis under externally applied compressive or shear forces; this axial realignment has been observed experimentally within a HRTEM [46].

### **Frictional Properties**

Classical MD simulations predict that very low friction forces were maintained throughout the tribological simulations at each contact pressure considered. Representative examples of the measured normal and lateral forces during the sliding simulations are shown for the ellipsoidal nanoparticle oriented on its minor axis (Figure 5-6A), the ellipsoidal nanoparticle oriented on its major axis (Figure 5-6B), and the nanooctahedron (Figure 5-6C); these graphs correspond to apparent contact pressures

of about 1.25, 1.0, and 0.9 GPa, respectively. Contrary to experimental TEM observations [46, 136], the MD simulations did not predict friction-induced exfoliation for any of the IF-MoS<sub>2</sub> nanoparticle systems considered. The most likely explanation for this result is the presence of little to no adhesion at the interface between the nanoparticle and the sliding surfaces during friction. *In situ* TEM studies showed that, frequently, the IF-MoS<sub>2</sub> nanoparticles adhered strongly to the sliding counterfaces during the experiments [46]. Another theoretical study by Schwarz *et al.* [138] indicated that there is strong adhesion between IF nanoparticles and substrates due to vdW interactions which favors the exfoliation of the outer layers onto the contacting surfaces. The findings further indicated that delamination is primarily induced by pressure and that the contribution of vdW adhesion to the exfoliation process scales with an increase in the ratio between nanoparticle diameter and the thickness of the IF walls. As such, the influence of adhesion on exfoliation is greatest when the IF nanoparticles have large diameters and a large hollow core, factors that are not present in the MD simulations as a result of computational limitations of the system sizes that could be considered.

### **Rolling Behavior**

Qualitatively, the ellipsoidal MoS<sub>2</sub> nanoparticle aligned along its major axis presents interesting opportunities during friction since the circular orientation in the direction of sliding allows the potential for rolling to occur. To assess this, an analysis of the rolling behavior during the friction simulations was performed. Figure 5-7 illustrates the results of this analysis for the ellipsoidal nanoparticle on its major axis during friction at a normal load of ~21.4 nN, which corresponds to an apparent contact pressure of around 170 MPa. Figure 5-7A depicts the angular displacement of the nanoparticle as a function of sliding distance. This graph shows that the nanoparticle's behavior was

characterized by alternating regions of positive and negative slopes. To elaborate, the positive slopes in Figure 5-7A correspond to nanoparticle rolling until a critical point when the nanoparticle slips at the interface resulting in the observed negative slopes. By analyzing the average angular velocities of the atoms within the nanoparticle, the percentage of rolling was quantified in the same manner as discussed previously for carbon nano-onions in Chapter 3. The percentage of rolling for the first 5 nm of the friction simulation is shown in Figure 5-7B; this graph supports the previous statement by illustrating that the nanoparticle experienced regions of 100% rolling behavior followed by slipping before commencing rolling again.

In order to determine the rolling behavior of the ellipsoidal nanoparticle as a function of normal load, the average angular and lateral displacements of the nanoparticle during rolling events were analyzed. The angular and lateral displacements refer to the magnitude of the vertical and horizontal vectors, respectively, of the positive slopes in Figure 5-7A; larger displacements indicate a greater propensity for rolling during the simulations than sliding. The results of this analysis are shown in Figure 5-8 which indicates that below  $\sim 48$  nN, corresponding to around 380 MPa, there is a significant increase in the average angular and lateral displacement of the nanoparticle signifying a transition from sliding to rolling behavior at lower loads. This load dependent rolling behavior agrees with the experimental TEM and HRTEM results discussed previously which showed that rolling of IF-MoS<sub>2</sub> nanoparticles was possible at lower contact pressures of  $\sim 100$  MPa while sliding and exfoliation became the preferred mechanism as contact pressures increased [46, 136]. Furthermore, a recent *in situ* HRSEM study by Tevet *et al.* [139] demonstrated that rolling was an important

mechanism for more spherical IF-WS<sub>2</sub> nanoparticles within the pressure range of 0.96 ± 0.38 GPa. Above this threshold, sliding became the dominant mechanism since the interfacial separation was no longer sufficient to allow nanoparticle rolling. The authors concluded that the rolling mechanism for IF nanoparticles could be improved through the use of nanoparticles with a spherical structure, better deagglomeration of the nanoparticles, more uniform size distribution, and smoother tribological contacts.

### **Comparison of Friction Coefficients**

Through analysis of the steady state forces during friction, the friction load ramp for each of the IF-MoS<sub>2</sub> systems was generated as is shown in Figure 5-9. From this graph, it is shown that changes in the structure and orientation of the MoS<sub>2</sub> nanoparticles resulted in friction coefficients that varied up to a factor of 4. The highest calculated friction coefficient was for the ellipsoidal nanoparticle aligned on the major axis at ~0.016 followed by the nano-octahedron at ~0.007. The lowest friction coefficient was for the ellipsoidal nanoparticle oriented along the minor axis at ~0.004. Despite this variation in friction coefficient for nanoparticles with different structures and/or orientations, the calculated coefficients of friction for the sliding of each of these nanoparticles was found to be very low and in good agreement with lamellar MoS<sub>2</sub> which, in ultra-high vacuum environments, can provide friction coefficients on the order of 0.002 [12].

### **Summary**

Through classical MD simulations of IF-MoS<sub>2</sub> nanoparticles between sulfur-terminated (110) BCC Mo substrates, this work indicated that the nanoparticles exhibit both structure and orientation dependent properties during both externally applied compressive and friction forces. The stiffness during compression was found to be the

lowest for the ellipsoidal nanoparticle aligned on its minor axis resulting from the presence of the large hollow core while the highest stiffness was observed for the nano-octahedron due to the vertical orientation of the MoS<sub>2</sub> walls at the interface. In addition, the IF-MoS<sub>2</sub> nanoparticles exhibited preferential exfoliation at the facet edges during compression of the nano-octahedron; no localized failure was observed for the ellipsoidal nanoparticle oriented along its minor axis. Regarding the tribological behavior, the results demonstrated that the friction coefficients varied up to a factor of 4 for the three systems considered ranging from 0.004 for the ellipsoidal nanoparticle oriented along its minor axis to 0.016 for the ellipsoidal nanoparticle on its major axis. Contrary to the purely sliding behavior of the nano-octahedron and the ellipsoidal nanoparticle aligned on its minor axis, a transition from a sliding to a rolling mechanism below ~380 MPa was observed for the ellipsoidal nanoparticle on its major axis resulting from the circular orientation in the direction of sliding. The results from this work provide insight into the influence of structure and orientation on the lubrication mechanisms involved during the compression and friction of IF nanoparticles.

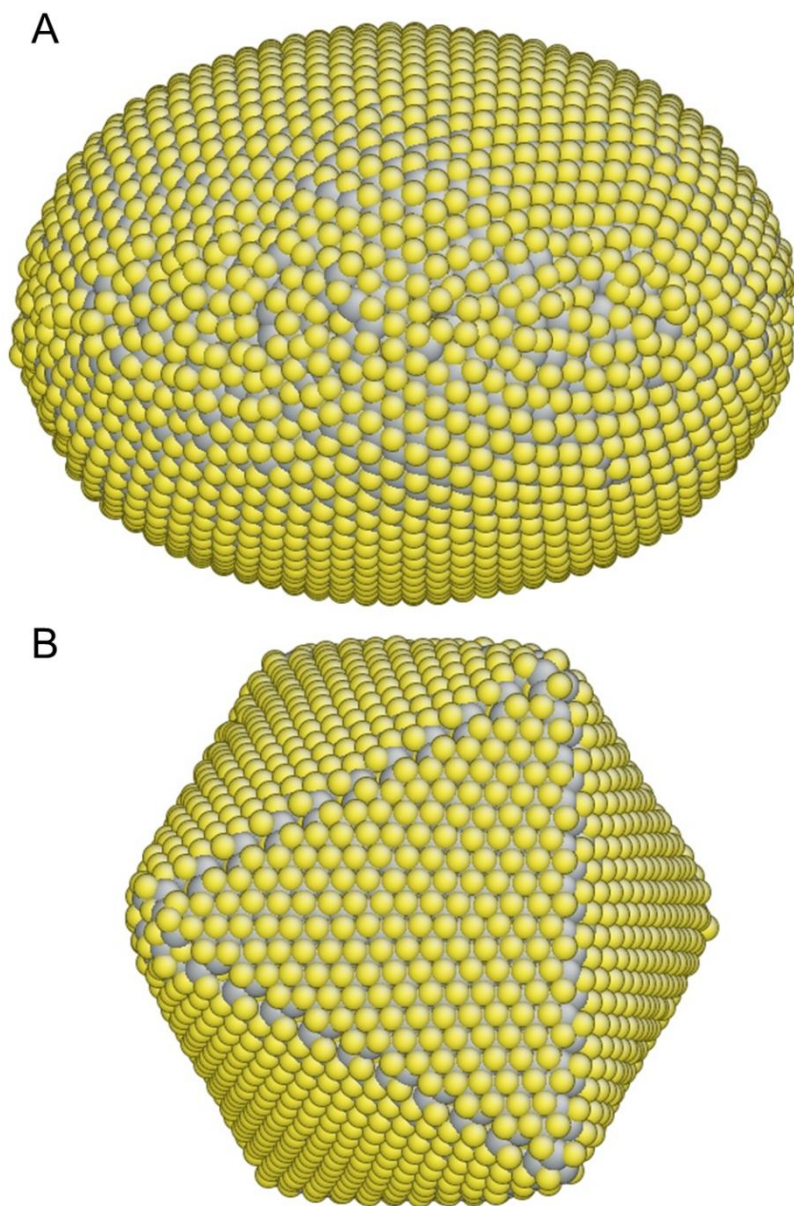


Figure 5-1. Snapshots of nested three layer IF-MoS<sub>2</sub> nanoparticles. A) Curved, ellipsoidal nanoparticle with major and minor diameters of ~9.5 and 6.3 nm, respectively, and B) faceted nano-octahedron with ~6.2 nm long edges. Yellow atoms are S and grey atoms are Mo.

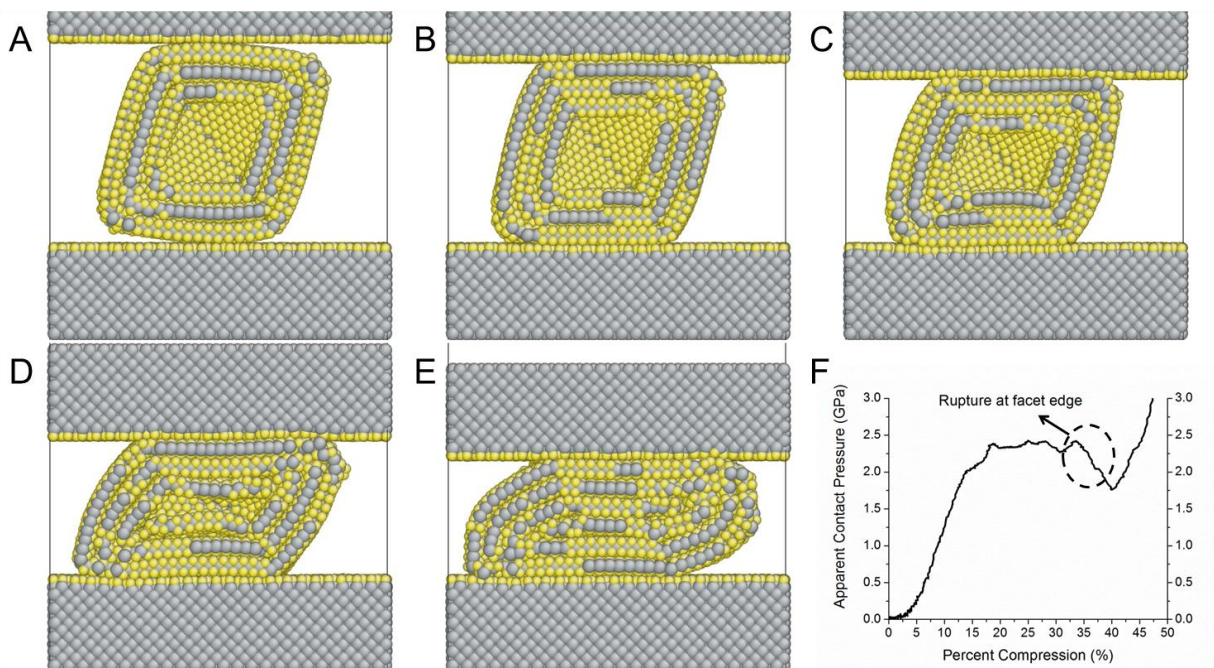


Figure 5-2. Cross-sectional snapshots of nano-octahedron at various stages during compression, A) initial, B) 8%, C) 15%, D) 30%, and E) 40%. F) Evolution of contact pressure during compression.

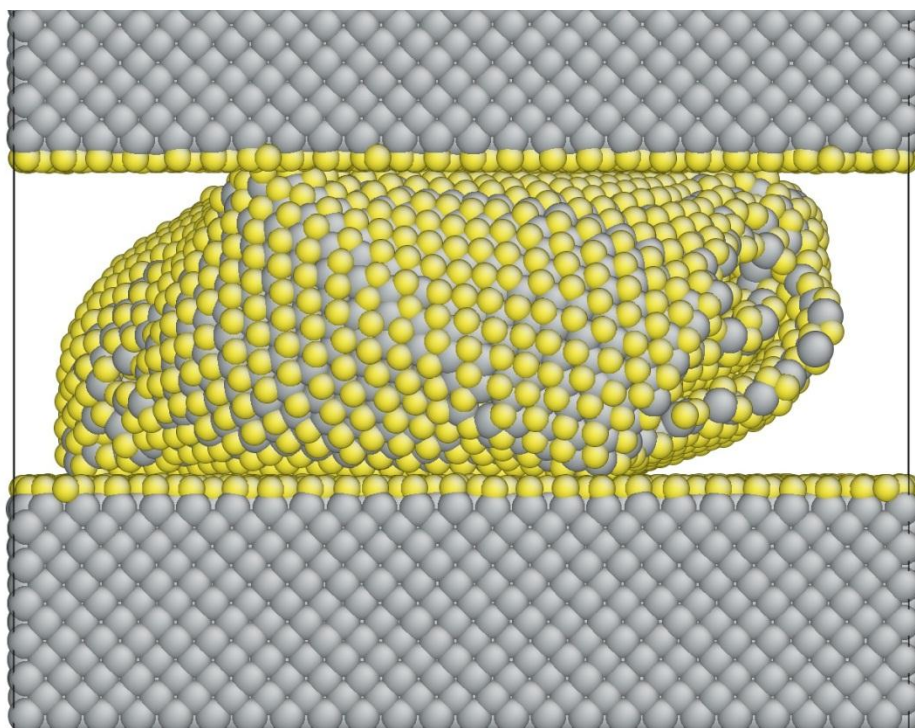


Figure 5-3. Snapshot of rupture at facet edge of IF-MoS<sub>2</sub> nano-octahedron during compression.

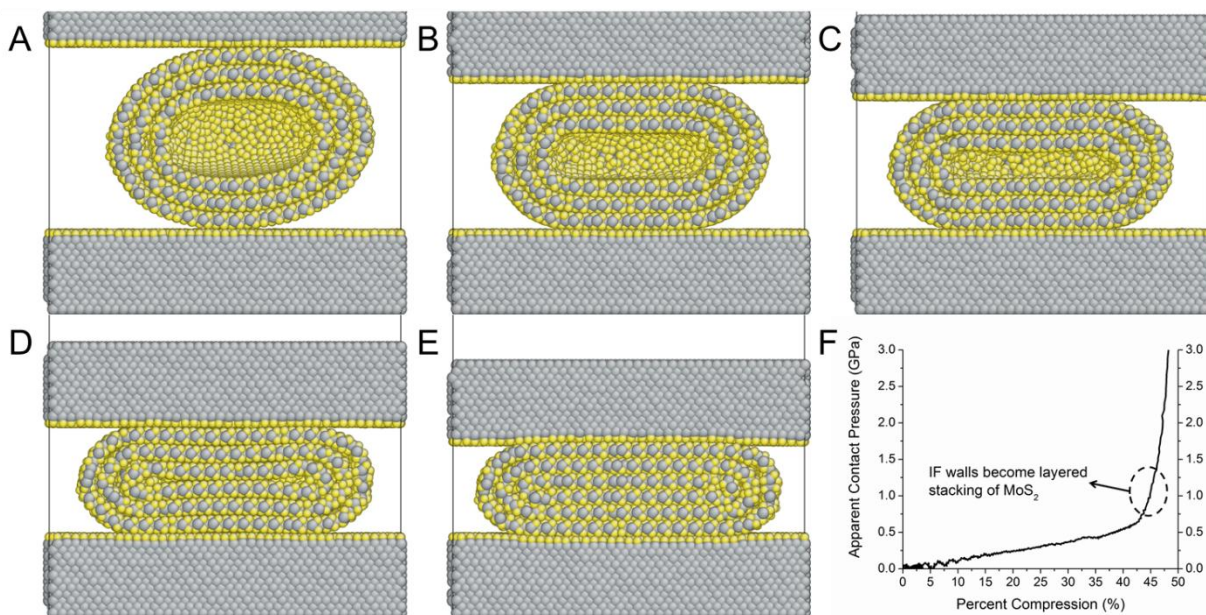


Figure 5-4. Cross-sectional snapshots of ellipsoidal nanoparticle oriented on minor axis at various stages during compression, A) initial, B) 20%, C) 30%, D) 43%, and E) 50%. F) Evolution of contact pressure during compression.

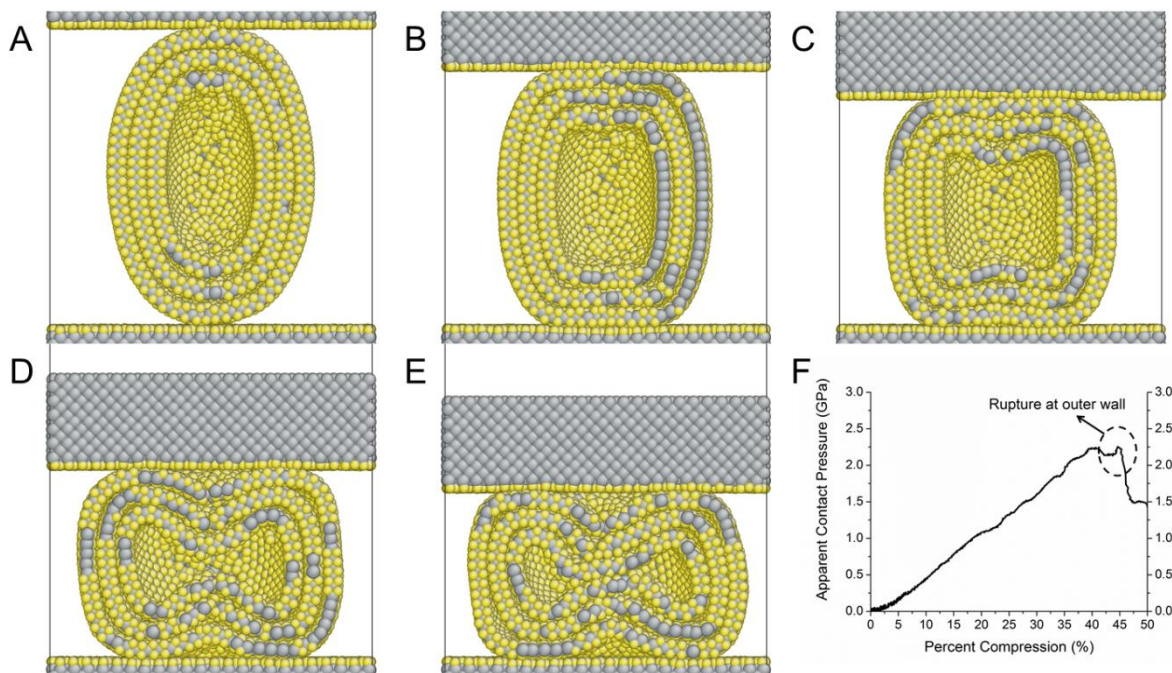


Figure 5-5. Cross-sectional snapshots of ellipsoidal nanoparticle oriented on major axis at various stages during compression, A) initial, B) 15%, C) 25%, D) 37%, and E) 45%. F) Evolution of contact pressure during compression.

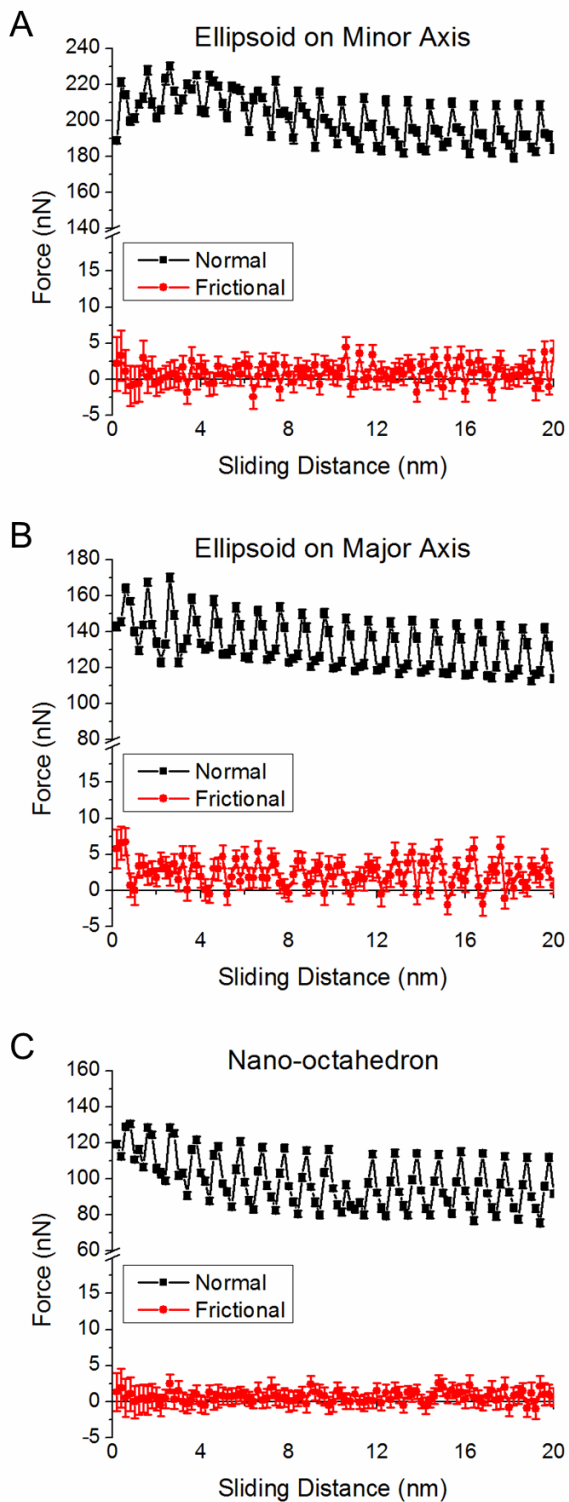


Figure 5-6. Graphs of frictional and normal forces as a function of sliding distance for A) ellipsoidal nanoparticle oriented along minor axis, B) ellipsoidal nanoparticle oriented along major axis, and C) nano-octahedron.

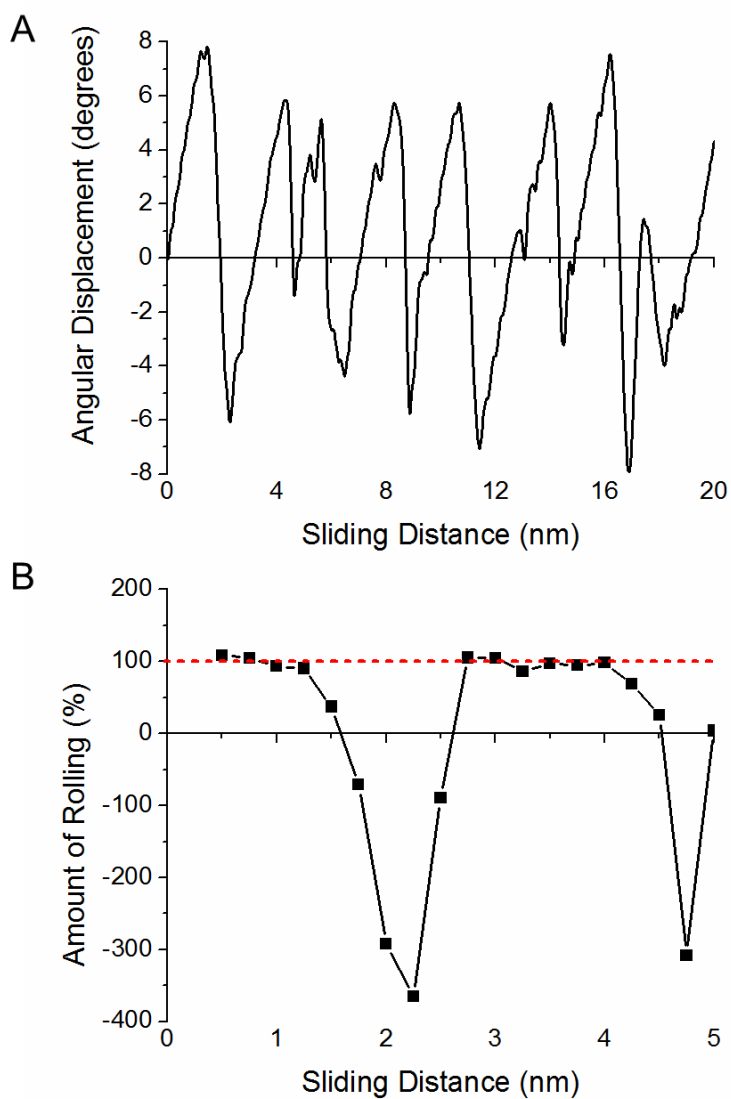


Figure 5-7. Analysis of rolling behavior during friction of ellipsoidal nanoparticle oriented along major axis at an average normal force of 21.4 nN. A) Angular displacement of nanoparticle during friction, and B) percentage of rolling observed during first 5 nm of simulation.

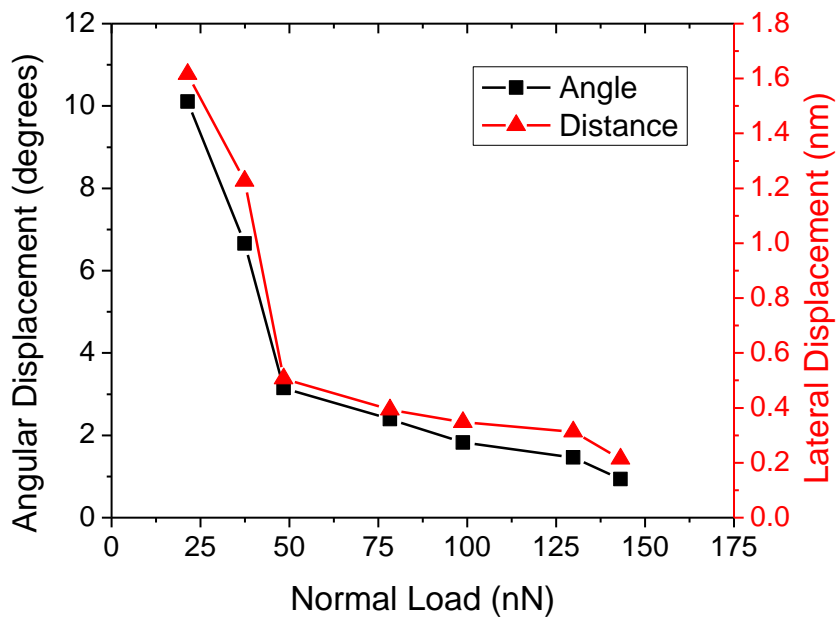


Figure 5-8. Average angular and lateral displacements between slip events during friction of ellipsoidal nanoparticle oriented along major axis as a function of applied load.

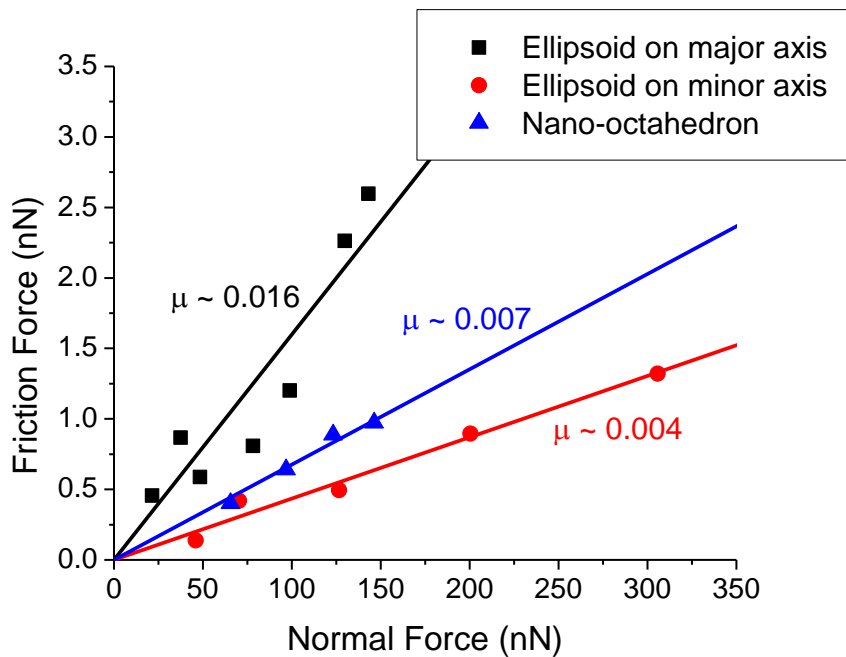


Figure 5-9. Friction load ramps for IF-MoS<sub>2</sub> systems. Errors associated with points are on the order of 2 nN for friction force and 3 nN for normal force.

## CHAPTER 6

### EFFECT OF EDGES ON TRIBOLOGICAL PROPERTIES OF LAMELLAR MOLYBDENUM DISULFIDE AT CRYOGENIC AND ELEVATED TEMPERATURES

Lamellar MoS<sub>2</sub> is well known to be intrinsically lubricious and has been widely researched and applied as a solid lubricant in tribological systems for many decades [9, 140-142]. As has been demonstrated for polytetrafluoroethylene [143], silicon [144], and graphite [145], a recent study by Zhao *et al.* [146] showed that MoS<sub>2</sub> exhibits temperature dependent tribological properties under cryogenic conditions. In particular, using an atomic force microscope (AFM) probe in an ultra-high vacuum environment, they showed that the friction on a pristine MoS<sub>2</sub> basal plane increased exponentially as temperatures decreased from 500 to 220 K; this temperature dependent friction behavior was attributed to thermally activated stick-slip with an activation energy of about 0.3 eV. Below 220 K, the tribological properties of the pristine MoS<sub>2</sub> transitioned to an athermal friction behavior due to the onset of interfacial wear resulting from the barriers for interfacial shear exceeding those necessary to break chemical bonds.

The influence of temperature on the tribological properties of MoS<sub>2</sub> was also probed on a sputtered MoS<sub>2</sub> surface [146]. The analysis indicated that friction was higher on the disordered MoS<sub>2</sub> surface at room temperature than on the pristine MoS<sub>2</sub> surface; by decreasing the system temperature to cryogenic conditions, the authors also found that interfacial wearing of the sputtered MoS<sub>2</sub> surface resulted in a less pronounced temperature dependent friction behavior than was observed for the pristine MoS<sub>2</sub> system. We hypothesize that interactions between sliding surfaces and high energy edge sites in macroscopic MoS<sub>2</sub> systems result in interfacial wear and significantly influence the temperature dependent tribological properties of MoS<sub>2</sub> films at cryogenic temperatures. To test this hypothesis, we performed classical MD simulations

in a perfect ultra-high vacuum environment involving friction of MoS<sub>2</sub> at cryogenic and elevated temperatures; these simulations investigate the effect of edge interactions in lamellar MoS<sub>2</sub> systems on the tribological performance relative to pristine MoS<sub>2</sub> systems.

### Computational Details

In these atomistic MD simulations the short-range covalent interactions were calculated using a Tersoff-type Mo-S potential [70] coupled with a Lennard-Jones (LJ) 12-6 potential [71] to describe the long-range vdW interactions. The systems were constructed so that a layer of MoS<sub>2</sub> was positioned between two sulfur-terminated (110) BCC molybdenum substrates that were in sliding contact. Specifically, two different tribological systems were considered. The first was a fully 2-D periodic MoS<sub>2</sub> system as is shown in Figure 6-1A. In the second system depicted in Figure 6-1B, edges were introduced to the MoS<sub>2</sub> layer by removing two 1 nm wide regions of MoS<sub>2</sub>, which resulted in two 1-D periodic MoS<sub>2</sub> ribbons at the interface. The friction simulations were controlled by the rigid displacement of the outermost 0.45 nm of the BCC Mo substrates while temperatures were maintained by applying a Langevin thermostat to the 0.9 nm of the BCC Mo substrates nearest to the rigid atoms. The remaining atoms were permitted to evolve freely according to Newtonian mechanics.

Prior to sliding, both MoS<sub>2</sub> systems were compressed at a rate of 2 m/s up to final contact pressures ranging from approximately 0.5 to 2.5 GPa; the contact pressures were determined by the area of the periodic substrates, which was ~23.35 nm<sup>2</sup> for the 2-D periodic MoS<sub>2</sub> system and ~46.7 nm<sup>2</sup> for the 1-D periodic MoS<sub>2</sub> ribbons. Each of the friction simulations was performed at a rate of 10 m/s for a distance of 10 to 12 nm. Additionally, the friction simulations of the 1-D periodic MoS<sub>2</sub> ribbons were done in two

orthogonal directions; the first was in the direction perpendicular to the MoS<sub>2</sub> edges, and the second was in the direction parallel to the MoS<sub>2</sub> edges (Figure 6-1B). Finally, the relative influence of temperature on the tribological performance was characterized by carrying out each simulation at temperatures ranging from 5 to 500 K.

### **Predicted Tribological Properties**

The classical MD simulations of the lamellar MoS<sub>2</sub> systems both with and without edges did not predict any temperature dependent friction, in disagreement with the experimental AFM findings [146]; as such, the tribological simulations were characterized by very low friction forces throughout sliding at each temperature and contact pressure considered. Figure 6-2 illustrates a few of these tribological simulations depicting the normal and frictional forces measured during friction of the 2-D periodic MoS<sub>2</sub> sheet sliding at 500 K (Figure 6-2A), the 1-D periodic MoS<sub>2</sub> ribbon sliding parallel to the edges at 300 K (Figure 6-2B), and the 1-D periodic MoS<sub>2</sub> ribbon sliding perpendicular to the edges at 5 K (Figure 6-2C). In each case, the sulfur-terminated interface remained chemically inert with only very weak vdW forces governing the interactions between the MoS<sub>2</sub> and (110) BCC Mo substrates. Additionally, the 1-D periodic MoS<sub>2</sub> ribbon systems exhibited no strong bonding interactions between the atoms at the high energy MoS<sub>2</sub> edge locations and the sliding surfaces of the Mo substrates. Hence, no interfacial wear was induced during friction of the 1-D periodic MoS<sub>2</sub> ribbons resulting in the same very low friction forces as were observed for the 2-D periodic MoS<sub>2</sub> sheet.

In order to further characterize any influence of temperature on the tribological properties of the lamellar MoS<sub>2</sub> systems, the steady state forces during friction were analyzed as indicated in the friction load ramps for the 2-D periodic MoS<sub>2</sub> sheet (Figure

6-3A), the 1-D periodic MoS<sub>2</sub> ribbon sliding parallel to the edges (Figure 6-3B), and the 1-D periodic MoS<sub>2</sub> ribbon sliding perpendicular to the edges (Figure 6-3C). The friction load ramps provide further support to the previous statement that the lamellar MoS<sub>2</sub> systems considered here did not display any temperature dependent friction behavior. To quantify this, the calculated friction coefficients from the load ramps in Figure 6-3 are summarized in Table 6-1. It was found that each tribological simulation of the MoS<sub>2</sub> systems both with and without edges resulted in a coefficient of friction of less than ~0.01; these values are consistent with those of experimental, lamellar MoS<sub>2</sub> systems in ultra-high vacuum environments which, as was mentioned previously in Chapter 5, can provide very low friction coefficients on the order of 0.002 [12].

To determine why the MD simulations presented here did not indicate temperature dependent tribological properties or, in particular, why the presence of edges in the 1-D periodic MoS<sub>2</sub> ribbon systems did not result in higher friction forces and interfacial wearing as compared to the 2-D periodic MoS<sub>2</sub> sheet, several possible explanations must be considered. First, the sulfur-termination of the (110) BCC Mo substrates may provide a counterface that is too chemically inert for use in determining the effects of edge interactions on the tribological properties of lamellar MoS<sub>2</sub>. Second, the BCC Mo/MoS<sub>2</sub> interface in these MD simulations was atomically flat which is not truly representative of real experimental systems such as the AFM study discussed previously [146] which utilized a Si<sub>3</sub>N<sub>4</sub> probe tip; the use of a hemispherical tip with a finite radius of curvature or a surface with some nominal roughness as the counterface for the lamellar MoS<sub>2</sub> systems could help to elucidate the predicted tribological behaviors. Finally, we must also consider the possibility that the Tersoff-type Mo-S

potential used here is not appropriate to describe the tribological simulations being performed. By carrying out new simulations which address the above possibilities, future work may be able to explain the experimentally observed temperature dependent friction behavior of lamellar MoS<sub>2</sub> as well as determine the influence of edge interactions on this behavior at cryogenic temperatures.

### **Summary**

Through classical MD simulations of lamellar MoS<sub>2</sub> systems both with and without edges, very low friction forces were predicted to be maintained throughout the sliding simulations at a range of temperatures considered from 5 to 500 K. As such, these simulations did not indicate any temperature dependent tribological properties. In addition, the presence of high energy MoS<sub>2</sub> edges in the 1-D periodic MoS<sub>2</sub> ribbon systems was not predicted to induce any interfacial wearing resulting from strong interactions with the sliding counterfaces. To explain these findings, it is possible that the sulfur-terminated (110) BCC Mo substrates provide a counterface that is too inert for strong interfacial interactions to occur and/or the atomically flat nature of the interface does not properly represent experimental systems. We also acknowledge the possibility that our interatomic potential is not appropriate to describe the tribological simulations performed in this study. Future MD simulations which address these concerns may be able to explain the experimental observations of temperature dependent tribological behavior at cryogenic temperatures in MoS<sub>2</sub> systems.

Table 6-1. Calculated friction coefficients from tribological simulations of lamellar MoS<sub>2</sub> systems at temperatures from 5 to 500 K.

Temperature (K)	2-D periodic sheet	1-D periodic ribbon (perpendicular sliding)	1-D periodic ribbon (parallel sliding)
5	0.0053 ± 0.001	0.0089 ± 0.001	0.0090 ± 0.004
100	0.0071 ± 0.002	0.0025 ± 0.001	0.0056 ± 0.001
200	0.0031 ± 0.002	0.0072 ± 0.002	0.0053 ± 0.001
300	0.0102 ± 0.002	0.0072 ± 0.001	0.0058 ± 0.001
500	0.0091 ± 0.001	0.0050 ± 0.002	0.0037 ± 0.001

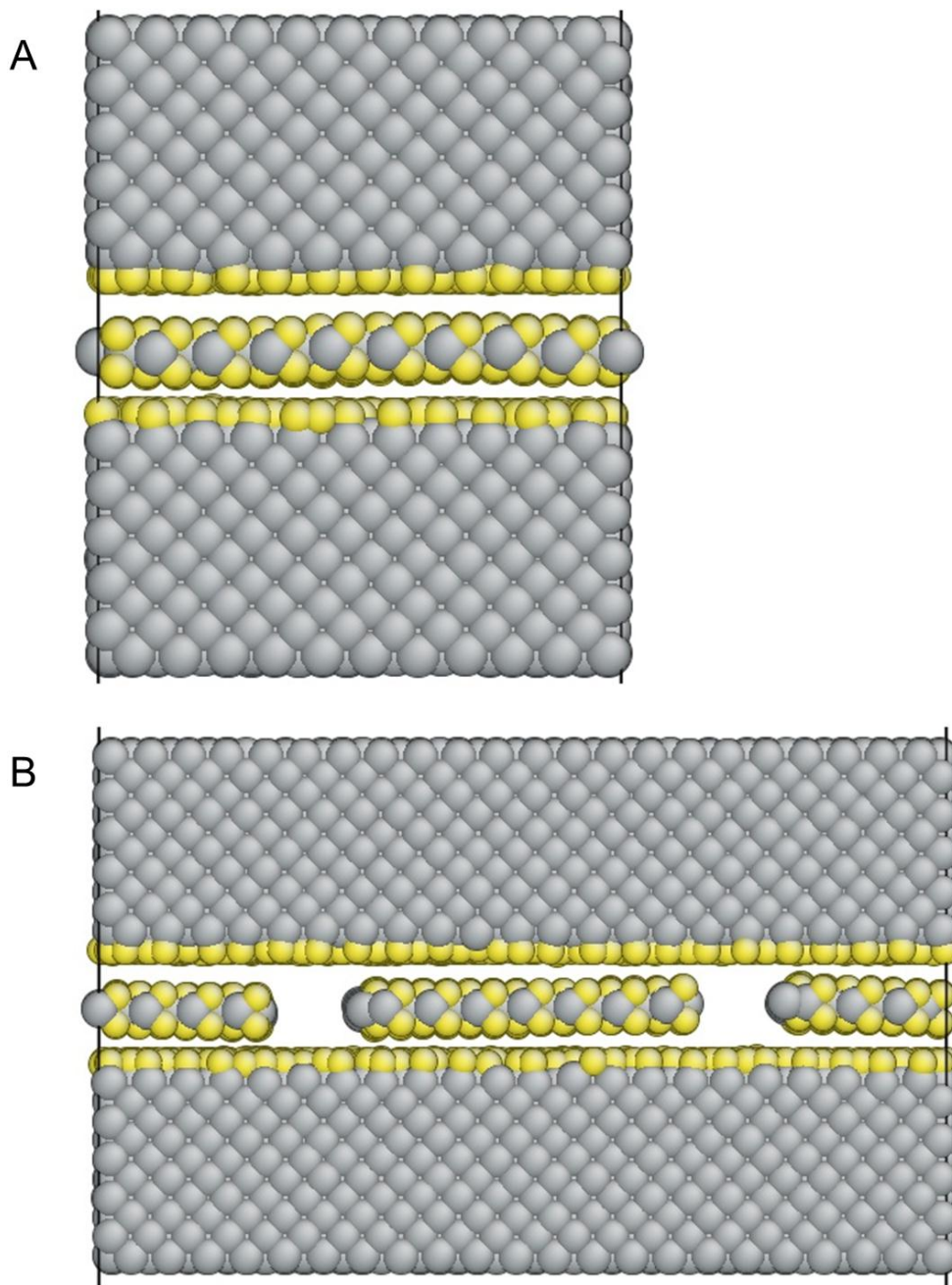


Figure 6-1. Snapshots of initial MoS<sub>2</sub> systems with A) a 2-D periodic sheet and B) 1-D periodic ribbons between sulfur-terminated (110) BCC Mo substrates for tribological simulations. Yellow atoms are S and grey atoms are Mo.

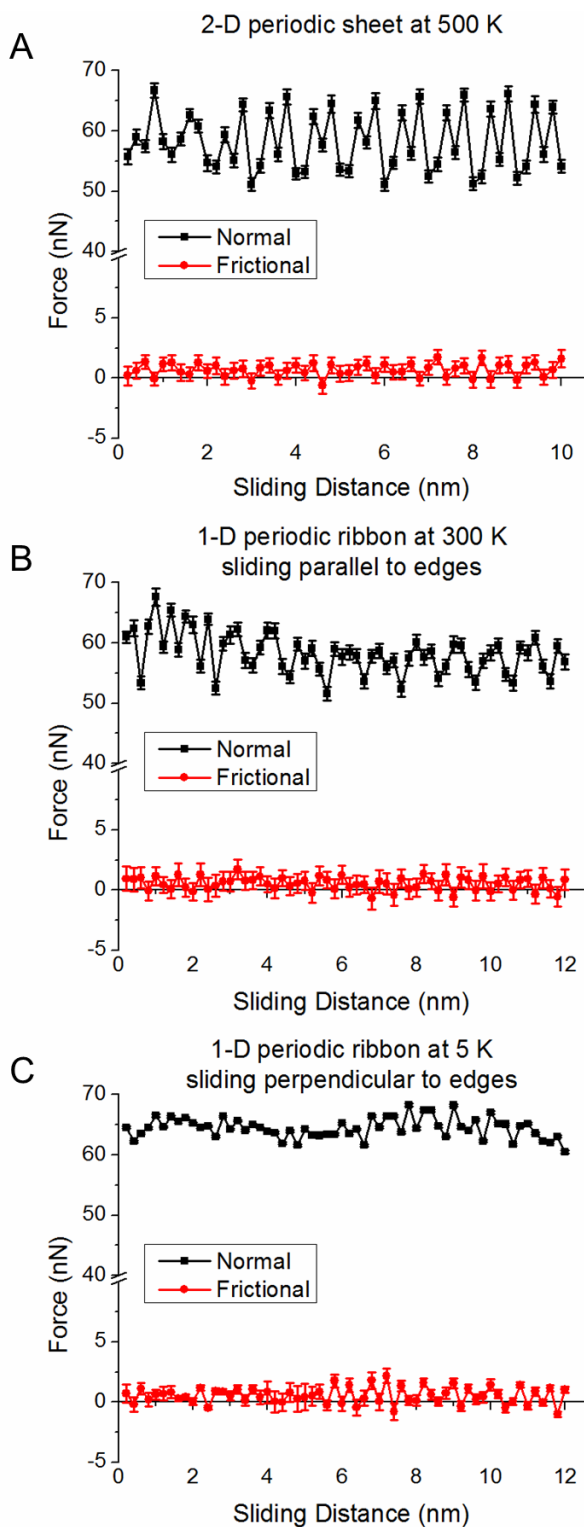


Figure 6-2. Frictional and normal forces of lamellar MoS<sub>2</sub> systems as a function of sliding distance for the A) 2-D periodic sheet at 500 K, B) 1-D periodic ribbon sliding parallel to the edges at 300 K, and C) 1-D periodic ribbon sliding perpendicular to the edges at 5 K.

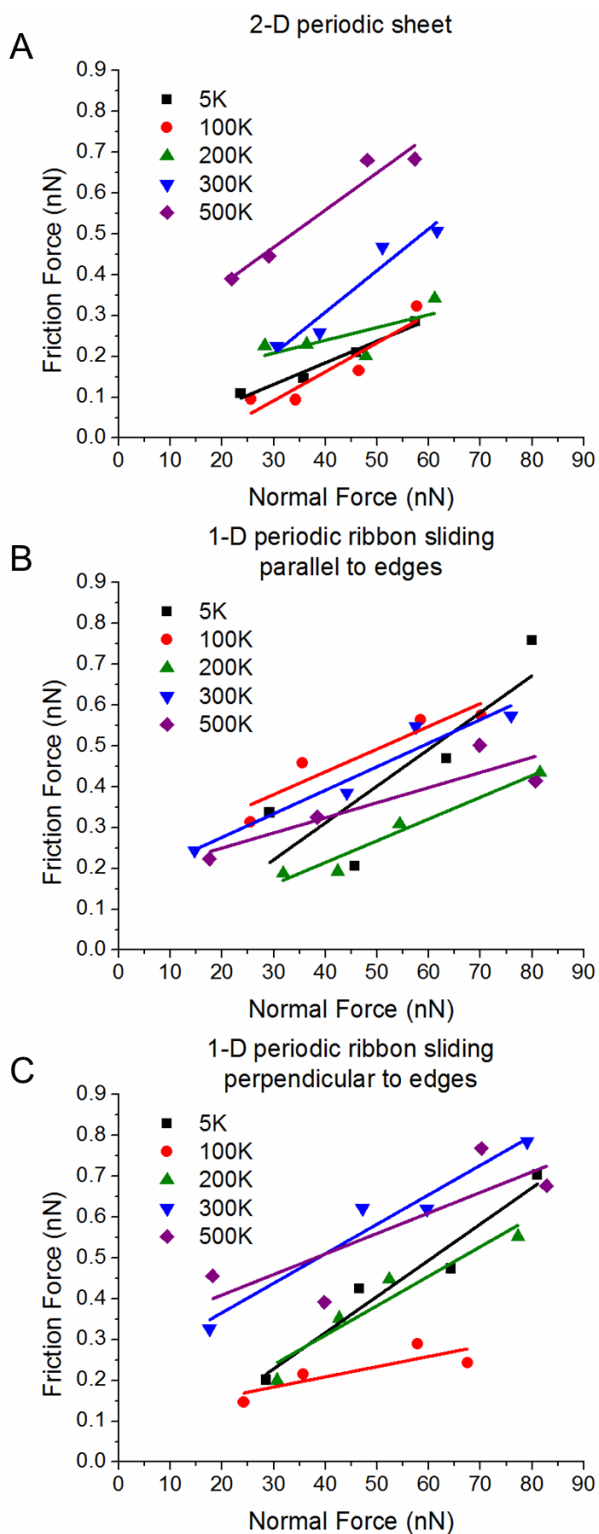


Figure 6-3. Friction load ramps for the A) 2-D periodic sheet, B) 1-D periodic ribbon sliding parallel to the edges, and C) 1-D periodic ribbon sliding perpendicular to the edges. Errors associated with points are on the order of 0.3 to 2 nN (5 to 500 K) for friction force and 0.3 to 3 nN (5 to 500 K) for normal force.

## CHAPTER 7

### MECHANICAL BEHAVIOR OF MOLYBDENUM DISULFIDE NANOTUBES UNDER COMPRESSION, TENSION, AND TORSION

The investigation of the mechanical properties of carbon nanotubes [147-149] has been of interest since their discovery by Iijima [94]. Shortly after, the discovery of inorganic nanotubes (INTs) [131] sparked further interest in this field since it became known that tubular nanostructures are not limited to carbon-based systems but can be formed from many different layered materials. Metal dichalcogenides such as MoS<sub>2</sub> and WS<sub>2</sub> are well known for their ability to form a variety of differing nanostructures [131, 150, 151] that have unique properties making them of interest for a variety of potential applications including scanning probe tips, high strength nanocomposites, mechanical devices, and electronics [96, 128, 152, 153]. Similar to graphite, metal dichalcogenide materials are lamellar with the individual layers separated by weak van der Waals (vdW) interactions. The significant difference between these inorganic materials and graphite is that the layers, rather than being planar, are three-dimensional tri-layers comprised of one layer of metal atoms (Mo, W, etc.) sandwiched between two layers of chalcogenide atoms (S, Se, or Te). Since many of the desired applications will require INTs to undergo a variety of mechanical loadings including compression, tension, and torsion, a thorough understanding of the mechanical behavior of INTs under different types of loading is essential for optimizing their use in specified applications.

Considerable interest has been shown in recent years investigating the mechanical properties of single-walled (SW) and multi-walled (MW) INTs through experimental and computational methods. Using a density-functional-based-tight-binding (DFTB) method, one study showed that, in the case of MoS<sub>2</sub> SWINTs, armchair nanotubes are slightly more energetically favorable than zigzag nanotubes at equivalent

diameters; this study also indicated that MoS<sub>2</sub> SWINTs do not exhibit reasonable strain energies until the diameters are greater than around 2 nm due to the energy penalty of rolling of the tri-layer structure [154]. For mechanical responses, the axial compression of WS<sub>2</sub> MWINTs has been experimentally investigated when they were attached to atomic force microscope tips [155], as have the tensile responses of WS<sub>2</sub> MWINTs in a scanning electron microscope [153]. The results of both of these studies showed a large amount of scatter in the measured properties resulting from variations in the orientation of the INTs during the experiments as well as inevitable errors in the estimation of the INT's length and diameter which greatly impacts the measurements.

Computational DFTB calculations have been used to investigate the Young's modulus and tensile strength [153] as well as the shear modulus [156] of MoS<sub>2</sub> SWINTs. An additional computational study showed that, for diameters less than about 7 nm, the elastic properties of MoS<sub>2</sub> SWINTs display diameter and chirality-dependent anisotropy [157]. Although first-principles-based methods are known for their high fidelity, their high computational expense requires that they be applied to systems with relatively small sizes which limit the range of mechanical behaviors which can be investigated. Atomistic MD simulations using empirical potentials allow for the consideration of larger nanotubes along with controlled structural properties including length, diameter, and chirality which will identify any interrelationships between these structural parameters and the measured elastic properties and elastic buckling events observed during mechanical loading of INTs. Here, classical MD simulations were used for the first time to probe the mechanical responses of MoS<sub>2</sub> INTs under applied compressive, tensile, and torsional loads.

## Inorganic Nanotubes

In a manner similar to carbon nanotubes, MoS<sub>2</sub> INTs can be thought of as being formed through the rolling of the S-Mo-S tri-layers that comprise the 2D lattice into cylindrical structures. Different types of these INTs are determined based on the specific lattice vector for the nanotube wrapping which is given by:

$$\vec{L}_{NT} = n \cdot \vec{a}_1 + m \cdot \vec{a}_2 \quad (7-1)$$

where  $\vec{a}_1$  and  $\vec{a}_2$  are primitive unit vectors and  $n$  and  $m$  are integer multipliers of the unit vectors. From Equation 7-1, three categories of nanotubes based on the  $(n, m)$  indices can be differentiated. The first type occurs when  $n = m$  which is referred to as the “armchair” configuration. The second type occurs when  $m = 0$  and  $n \neq 0$  and is called the “zigzag” configuration. All other possible integer combinations where  $n \neq m$  are identified as “chiral” nanotubes; the present work only involved armchair and zigzag nanotubes and did not consider chiral INTs. Figure 7-1 indicates the directions along which armchair and zigzag type nanotubes are formed through the wrapping of the MoS<sub>2</sub> lattice.

## Computational Details

For the classical MD simulations performed in this study, a Tersoff-type Mo-S potential [70] coupled with a Lennard-Jones (LJ) 12-6 potential [71] was used to calculate the short-range and long-range atomic interactions, respectively. In these simulations, six different armchair and zigzag SWINTs (three of each) were considered with indices of (27,27), (41,41), and (56,56) for the armchair nanotubes and (47,0), (71,0), and (97,0) for the zigzag nanotubes which correspond to outer diameters between approximately 5 and 10 nm. Additionally, three lengths of 10, 20, and 30 nm,

for each SWINT were considered, which allowed for differing aspect ratios, defined as length divided by diameter, ranging from about 1.0 to 6.4. Furthermore, two double-walled (DW) INTs (one armchair and one zigzag) with lengths of 20 nm were also considered. The armchair DWINT had an outer wall with indices of (34,34) and an inner wall with indices of (27,27) which is referred to as (34,34)@(27,27); the zigzag DWINT had indices of (59,0)@(47,0). For both of the DWINTS, the outer diameter was about 6 nm.

Prior to carrying out the compressive, tensile, and torsional loading, each SWINT and DWINT was equilibrated by applying a thermostat to 100% of the atoms in the system in order to minimize the strain energy caused by the wrapping of the tri-layer structure. After equilibration, regions of the INTs were denoted as either rigid and moving, thermostat, or active as is indicated in Figure 7-2. The thermostat regions comprised 30% of the system (15% at each nanotube end) and maintained a temperature of 300K during each simulation using a velocity rescaling thermostat which has been shown to provide good temperature control without negatively impacting the measured forces for carbon nanotubes [158]. The rigid and moving regions made up the outermost 6% of each nanotube end; in these regions, equal and opposite compressive, tensile, or torsional loads were attained through the rigid displacement of these atoms in specified directions. Specifically, in the case of compression and tension, a constant strain rate of 20%/ns was applied to each nanotube which corresponds to a rate of 2 m/s for every 10 nm of nanotube length; the specific rate for torsional deformation was 2 Grad/s which corresponds to 2 rad/ns of torsion. The active region constituted the remaining atoms which were permitted to evolve freely according to Newtonian

mechanics. For the simulations of torsion for the DWINTs, two different cases were considered. In the first, torsion was applied to only the outer wall, and in the second, torsion was applied to both the outer and inner walls simultaneously. These two cases allowed for the characterization of changes in the mechanical response of INTs in applications where the clamping of the nanotube could result in torsional loading being applied only on the outermost wall or to multiple walls that are being twisted at the same time.

Previous studies involving carbon nanotubes have indicated that the cutoff function in the reactive empirical bond order (REBO) potential [66] overestimates the necessary forces for breaking covalent bonds through the unphysical increasing of forces for bonds within the cutoff region [159-161]. Since this negative influence from the cutoff function was also observed in this work, the tension simulations performed here only probe the elastic response of the MoS<sub>2</sub> nanotubes rather than deformation to failure to ensure the physicality of the results. In addition, to appropriately capture the elastic buckling during torsion without any decrease in coordination for the Mo atoms, the short-range cutoff regions were extended from 0.35-0.38 to 0.39-0.395 Å for the Mo-Mo interactions and from 0.275-0.305 to 0.32-0.325 Å for the Mo-S interactions. This modification had no effect on the measured elastic properties since the short-range interactions were still limited to only the nearest neighbors.

## **Compressive and Tensile Loading**

### **Young's Modulus**

To calculate the applied stress during compression and tension, the cross-sectional area was calculated using a wall thickness of 0.615 nm for the armchair and zigzag SWINTs corresponding to the layer separation in bulk MoS<sub>2</sub> [154]. Similarly, a

value of 1.23 nm, or twice the single-walled thickness, was used for the thickness of the DWINTs. The applied stress as a function of strain during the compression of each SWINT and DWINT is illustrated in Figure 7-3A for the armchair INTs and in Figure 7-3B for the zigzag INTs. For each compression simulation, the applied stress increased linearly with strain until a critical point at which buckling occurred resulting in a significant decrease in stress. The very similar slopes in the linear regions of Figure 7-3 indicate that the Young's modulus is mostly invariant to changes in length and diameter as well as between SW and DWINTs. In order to quantify this, the Young's modulus during the compression and tension was calculated by:

$$Y = \frac{1}{V_0} \frac{\partial^2 U}{\partial \varepsilon^2} \quad (7-2)$$

where  $U$  is the total strain energy,  $\varepsilon$  is the strain, and  $V_0$  is the equilibrium volume which was determined by:

$$V_0 = L_0 \pi (r_o^2 - r_i^2) \quad (7-3)$$

where  $L_0$  is the initial length,  $r_o$  is the outer radius, and  $r_i$  is the inner radius. For the volume calculations, the unit  $r_o - r_i$  was always equal to the wall thickness of 0.615 or 1.23 nm for the SW and DWINTs, respectively.

Using Equation 7-2, we applied a second-order polynomial fit of the total energy over the first 3% strain to determine the Young's moduli for each of the armchair and zigzag INTs considered. The results from this analysis are provided in Table 7-1 for the moduli during compression and in Table 7-2 for the moduli during tension; the errors associated with the calculated moduli represent the statistical error resulting from the polynomial fit. In general, the MD simulations showed that the Young's modulus during

compression was about 12% larger for the armchair INTs and about 4% larger for the zigzag INTs than during tension. This stiffening of the nanotubes during compression relative to tension likely results from two different sources. First, the bond anharmonicity resulting from the strong repulsive energy barrier for decreasing bond lengths results in a larger increase in energy during compression. Second, since the S atoms within the nanotube walls are not covalently bonded, they are subjected to repulsive vdW forces during compression. In addition to the differences between compression and tension, the Young's modulus for the armchair INTs was about 7.5% larger than the zigzag INTs; this difference can also be attributed to the same sources. Since the Mo and S atoms are aligned orthogonal to the direction of wrapping for the armchair nanotubes (Figure 7-1), there is a more significant increase in the repulsive energy barriers for the Mo-Mo and S-S interactions than is the case for the zigzag nanotube where the atoms are not aligned perpendicular to the direction of wrapping. Despite these differences, the values for the Young's modulus from the MD simulations are in good agreement with DFTB calculations which suggest a value of around 230 GPa [155] and with that of bulk MoS<sub>2</sub> (238 GPa [137]). This agreement indicates that the use of atomistic MD simulations is an appropriate method for calculating the mechanical properties of MoS<sub>2</sub> INTs.

### **Compressive Buckling Analysis**

Qualitatively, it was observed that each of the MoS<sub>2</sub> SWINTs and DWINTs considered demonstrated the same buckling behavior; at a critical point during the compression simulations, buckling was initiated near the middle of the INTs followed by the collapse of the MoS<sub>2</sub> walls within the axis of compression. Images of the 10, 20, and 30 nm long nanotubes after buckling at 0.08 strain are shown in Figure 7-4 for the (27,27) armchair SWINTs and in Figure 7-5 for the (71,0) zigzag SWINTs. In some

instances, as illustrated in these images for the 20 and 30 nm long SWINTs, the buckled form of the nanotubes was characterized by two separate collapsed regions that were orthogonal to each other. The buckling of the MoS<sub>2</sub> INTs within the nanotube axis is the same as the mode of buckling reported for carbon nanotubes that have aspect ratios of less than 10 to 15 [162].

As is illustrated in Figure 7-3, both the armchair and zigzag INTs demonstrate buckling behavior that varies depending on changes in length and diameter. In order to quantify this observation, the critical buckling stress and strain for each of the SWINTs and DWINTs considered are shown for the armchair INTs in Figure 7-6A and for the zigzag INTs in Figure 7-6B. For the SWINTs, increasing the length from 10 to 20 nm resulted in the critical buckling stress decreasing by 10.9, 5.6, and 19.6% for the (27,27), (41,41), and (56,56) armchair SWINTs, respectively; the same length increase for the zigzag SWINTs resulted in the critical buckling stress decreasing by 1.4, 5.5, and 12.0% for the (47,0), (71,0), and (97,0) SWINTs, respectively. However, as the SWINTs increased in length from 20 to 30 nm, the simulations did not indicate any apparent impact of length on the critical buckling stress and strain. This result is consistent with findings for the compression of carbon nanotubes which have shown that, for a given nanotube diameter, the critical buckling force converges with increasing aspect ratio [163].

Regarding the effect of increasing diameter, the critical buckling stress of the 10 nm long (41,41) and (56,56) SWINTs decreased by 16.4 and 22.8% relative to the (27,27) SWINT. Relative to the 10 nm long (47,0) SWINT, the critical buckling stress of the (71,0) and (97,0) SWINTs decreased by 8.1 and 22.9%. On the other hand, for the

20 and 30 nm long SWINTs considered here, the results indicated a nearly linear relationship between critical buckling stress and diameter; specifically, the buckling stress of the armchair SWINTs in Figure 7-6A decreased by around  $0.77 \pm 0.05$  GPa for each nm increase in diameter while that of the zigzag SWINTs in Figure 7-6B decreased by around  $0.85 \pm 0.05$  GPa per nm. The different behavior demonstrated for the 10 nm long SWINTs relative to the longer nanotubes is likely a result of the very small aspect ratios which are less than about 2.0; for a given nanotube diameter, similar to the discussion previously, the critical buckling force for carbon nanotubes has been shown to diverge when the aspect ratio decreases to small values [163].

For the response of the DWINTs during compression, the presence of the inner nanotube layer was found to provide a slight increase in the critical buckling stress. Relative to the relationship between the 20 nm long SWINTs considered here, the critical buckling stress for the (34,34)@(27,27) armchair DWINT and the (59,0)@(47,0) zigzag DWINT increased by approximately 6.9% and 8.9%, respectively. Finally, considering the effect of nanotube chirality on the mechanical behavior, the zigzag INTs were found to exhibit higher critical buckling strains than the armchair INTs for the range of lengths and diameters considered here. Specifically, the critical buckling strains for the (47,0) SWINTs were about 11% larger than the (27,27) SWINTs. However, since the critical stress and strain with increasing nanotube diameter decreased at a greater rate for the zigzag SWINTs than the armchair SWINTs, the difference between critical buckling strains became less significant; the buckling strains for the (97,0) SWINTs were larger than the (56,56) SWINTs by about 4%. In addition, the (59,0)@(47,0) zigzag

DWINT had a critical buckling strain that was around 15.3% higher than the (34,34)@(27,27) armchair DWINT.

## Torsional Loading

### Torsional Shear Modulus

During applied torsion, the evolution of the torsional moment as a function of torsional angle for the both the armchair (Figure 7-7A) and zigzag (Figure 7-7B) INTs indicated that changes in either the length or diameter of the nanotubes had a significant impact on the measured torsional moment. In order to determine if there is a similar dependence for the elastic properties, the torsional shear modulus for the MoS<sub>2</sub> SWINTs and DWINTs was calculated by:

$$G = \frac{1}{V_0} \frac{\partial^2 U}{\partial \gamma^2} \quad (7-4)$$

where  $\gamma$  is the torsional shear strain which was determined by:

$$\gamma = \frac{r\theta}{L_0} \quad (7-5)$$

where  $r$  is the average nanotube radius,  $L_0$  is the nanotube length, and  $\theta$  is the torsional angle. In this analysis, we applied a second-order polynomial fit of the total energy over the first 0.4 radians of torsion for the (27,27), (34,34)@(27,27), (47,0), and (59,0)@(47,0) INTs, the first 0.26 radians of torsion for the (41,41) and (71,0) SWINTs, and the first 0.18 radians of torsion for the (56,56) and (97,0) SWINTs. The results for the torsional shear moduli from Equation 7-4 are provided in Table 7-3. With the exception of the (27,27) SWINTs, which were shown to have a modulus of around 10% lower than the (41,41) and (56,56) SWINTs, this analysis shows that the torsional shear modulus was not strongly affected by changes in length, diameter, nanotube chirality, or

number of MoS<sub>2</sub> walls. In addition, these values are in good agreement with the results of recent theoretical calculations which predict a value of about 88 GPa for MoS<sub>2</sub> INTs with diameters of greater than ~7 nm [157]. This agreement provides further support for the accuracy of the classical MD simulations.

### **Relationships between Length, Diameter, and Torsional Stiffness**

In the same manner as torsional shear modulus in Equation 7-4, the torsional stiffness was calculated as [56]:

$$K = \frac{TL_0}{\theta} = L_0 \frac{\partial^2 U}{\partial \theta^2} \quad (7-6)$$

where  $T$  is the torsional moment,  $L_0$  is the length, and  $\theta$  is the torsional angle. Using Equation 7-6, the torsional stiffness for the INT considered as a function of diameter is shown in Figure 7-8. From this analysis, we found that the torsional stiffness of both the armchair and zigzag INTs is relatively invariant with length and is only dependent on diameter. For the armchair SWINTs, the torsional stiffness increased by about 279% for the (41,41) SWINTs and 884% for the (56,56) SWINTs relative to the (27,27) SWINTs; for the zigzag SWINTs, the torsional stiffness increased by about 247% for the (71,0) SWINTs and 805% for the (97,0) SWINTs relative to the (47,0) SWINTs. This relates to a dependence of torsional stiffness on nanotube diameter that scales approximately as  $K \propto D^{3.1}$  for the armchair INTs (Figure 7-8A) and as  $K \propto D^{3.06}$  for the zigzag INTs (Figure 7-8B) which is in good agreement with similar simulations involving the torsion of carbon nanotubes [56, 147]. The relationship between nanotube length and torsional stiffness was determined by calculating the torsional stiffness per unit length which was determined by:

$$K' = \frac{T}{\theta} = \frac{K}{L_0} \quad (7-7)$$

From Equation 7-7, the torsional stiffness per unit length was found to scale close to  $1/L_0$  as approximately  $K' \propto 1/L_0^{0.98}$  and  $K' \propto 1/L_0^{0.94}$  for the armchair and zigzag SWINTs, respectively.

For the DWINTs, the calculated torsional stiffness when applying torsional loading only to the outer wall is consistent with the relationship between stiffness and diameter described by the SWINTs; the torsional stiffness of the (34,34)@(27,27) DWINT increased by about 116% compared to the (27,27) SWINTs while the (59,0)@(47,0) DWINT increased by about 106% compared to the (47,0) SWINTs. This indicates that the torsional stiffness is unaffected by the presence of additional nanotube layers which is the same as findings for carbon nanotubes [56]. When torsion was applied to both walls of the DWINTs, however, the torsional stiffness of the (34,34)@(27,27) and the (59,0)@(47,0) DWINTs, relative to conditions of torsion applied only to the outer wall, increased by about 46% as is shown in Figure 7-8; the measured torsional stiffness when applying torsion to both walls is equivalent to the sum of the torsional stiffness for the outer (34,34) or (59,0) nanotube and the inner (27,27) or (47,0) nanotube.

### **Torsional Buckling Analysis**

During torsion of each SWINT and DWINT, as illustrated in Figure 7-7, the torsional moment increased linearly with torsion angle until a critical point at which the MoS<sub>2</sub> walls buckled resulting in a significant decrease in nanotube stiffness. Representative images of the buckled form of these INTs are shown for each length considered in Figure 7-9. Qualitatively, two different buckling behaviors were observed depending on the aspect ratio of the INT. For aspect ratios less than about 3.1, which

corresponds to all of the 10 nm long SWINTs, the 20 nm (41,41) and (71,0) SWINTs, the 20 nm (56,56) and (97,0) SWINTs, and the 30 nm (56,56) and (97,0) SWINTs, the MoS<sub>2</sub> wall of the nanotubes collapsed at three points equally spaced around the circumference of the INT as is shown in Figure 7-9A and 7-9C. For all other SWINTs and the DWINTs, which have higher aspect ratios, the MoS<sub>2</sub> walls collapsed at two points around the circumference as is shown in Figure 7-9B and 7-9D; this buckled configuration for the MoS<sub>2</sub> INTs is the same as previous observations for carbon nanotubes after torsional buckling [56].

The critical buckling moments for all of the SWINTs and DWINTs are indicated in Figure 7-10A for the armchair INTs and in Figure 7-10B for the zigzag INTs. From the torsion simulations, no significant effect of nanotube chirality was observed on the critical buckling moments for the INTs considered here; the armchair and zigzag SWINTs and DWINTs demonstrated similar quantitative values and the same qualitative behavior over the range of lengths and diameters considered. Specifically, the critical buckling moment for each of the INTs was found to decrease with increasing length. Increasing the nanotube length from 10 to 20 nm, the critical buckling moment for the armchair SWINTs decreased by about 45.5, 32.9, and 37.2% for the (27,27), (41,41), and (56,56) SWINTs, respectively, while the buckling moment for the zigzag SWINTs decreased by about 36.7, 29.0, and 28.9% for the (47,0), (71,0), and (97,0) SWINTs, respectively. For the 30 nm SWINTs, relative to the 10 nm SWINTs, the critical buckling moment for the armchair SWINTs decreased by around 55.5, 43.7, and 43.7% for the (27,27), (41,41), and (56,56) SWINTs, respectively, while the buckling moment for the

zigzag SWINTs decreased by around 45.0, 38.6, and 41.9% with respect to the (47,0), (71,0), and (97,0) SWINTs.

Regarding the effect of increasing diameter, Figure 7-10 indicates that, for the INTs considered here, the 20 and 30 nm long SWINTs exhibited a roughly linear relationship between critical buckling moment and nanotube diameter. For the 20 nm SWINTs, the buckling moment for the armchair SWINTs increased by approximately  $55.1 \pm 1.6$  nNm while the zigzag SWINTs increased by about  $61.2 \pm 2.0$  nNm for each nm increase in diameter. For the 30 nm SWINTs, the buckling moment for the armchair and zigzag SWINTs increased by about  $51.5 \pm 0.9$  nNm and  $48.7 \pm 0.5$  nNm for each nm increase in diameter, respectively. The buckling moment for the 10 nm long SWINTs similarly scaled with diameter increasing by about 67% for the (41,41) SWINT and 167% for the (56,56) SWINT relative to the (27,27) SWINT and increasing by around 87% for the (71,0) SWINT and 205% for the (97,0) SWINT in comparison with the (47,0) SWINT.

For the torsional buckling of the DWINTs, the presence of the inner wall resulted in an increase in the critical buckling moment as is depicted in Figure 7-10. When torsion was applied only to the outer wall, the critical buckling moment was increased by approximately 113% for the (34,34)@(27,27) DWINT and by 99% for the (59,0)@(47,0) DWINT relative to the relationship observed for the 20 nm long SWINTs discussed previously. When torsion was applied to both nanotube walls, the critical buckling moment was only decreased by about 12.5% for the (34,34)@(27,27) DWINT and by 8.2% for the (59,0)@(47,0) DWINT in comparison with the buckling moment when torsion was applied only to the outer wall. However, this relatively small difference in

critical buckling moment becomes more significant when considering the difference in torsional stiffness discussed in the previous section. For the case when torsion was applied only to the outer MoS<sub>2</sub> wall, the critical buckling angle was around 1.12 radians for the (34,34)@(27,27) DWINT and 1.07 radians for the (71,0)@(47,0) DWINT. When torsion was applied to both walls, on the other hand, the critical buckling angle decreased by about 40.5 and 41.3% for the (34,34)@(27,27) and (71,0)@(47,0) DWINTs, respectively. This indicates that, along with an increase in the measured torsional stiffness, there is a significant reduction in the critical buckling angle when torsion is applied to both of the MoS<sub>2</sub> walls rather than only the outer wall.

### **Summary**

The work presented here provided, for the first time, an investigation of the mechanical behavior of MoS<sub>2</sub> nanotubes using classical MD simulations. Analysis of SWINTs and DWINTs subjected to compressive, tensile, and torsional loading indicated that the MD simulations predict values for the Young's modulus and torsional shear modulus of the nanotubes that are in good agreement with previous studies using different methods. Specifically, little to no dependence on length and diameter was predicted for the elastic properties over the range of dimensions considered in these simulations (10 to 30 nm lengths and 5 to 10 nm diameters). During compressive loading, the nanotubes exhibited critical buckling stresses that scaled inversely with increasing diameter. However, nanotube length was shown to have no discernible impact on the critical buckling stress and strain for lengths of at least 20 nm. Also, the addition of an inner nanotube for the DWINTs resulted in a slight increase in the critical buckling stress relative to the SWINTs.

During torsional loading, the torsional stiffness of the INTs was found to scale with diameter approximately as  $K \propto D^{3.1}$  for the armchair nanotubes and as  $K \propto D^{3.06}$  for the zigzag nanotubes which is in good agreement with previous findings for carbon nanotubes. In addition, the critical buckling moments were found to be significantly impacted by changes in either nanotube length or diameter. Also, the presence of the inner wall in the DWINTs increased the critical buckling moment by 113% and 99% for the armchair and zigzag DWINTs, respectively, when torsion was applied only to the outer MoS<sub>2</sub> wall; this extension of torsion prior to buckling was negatively affected when torsion was applied to both walls which resulted in a decrease in the critical buckling angle by around 41%. The findings from these atomistic MD simulations provide detailed information about the mechanical responses of MoS<sub>2</sub> INTs over a range of lengths and diameters when subjected to varying loading conditions.

Table 7-1. Calculated Young's moduli (in GPa) from compression simulations.

(n,m)	$L_0$ (10 nm)	$L_0$ (20 nm)	$L_0$ (30 nm)
(27,27)	$234.4 \pm 3.9$	$241.2 \pm 2.8$	$243.4 \pm 2.3$
(41,41)	$243.8 \pm 3.2$	$245.5 \pm 2.3$	$241.8 \pm 1.8$
(56,56)	$242.7 \pm 2.6$	$248.5 \pm 1.9$	$242.0 \pm 1.5$
(34,34)@(27,27)		$240.9 \pm 1.8$	
(47,0)	$216.9 \pm 3.7$	$221.3 \pm 2.8$	$222.4 \pm 2.2$
(71,0)	$230.6 \pm 3.2$	$226.4 \pm 2.3$	$224.8 \pm 1.8$
(97,0)	$230.6 \pm 2.6$	$229.2 \pm 2.4$	$229.2 \pm 1.6$
(59,0)@(47,0)		$222.9 \pm 1.9$	

Table 7-2. Calculated Young's moduli (in GPa) from tension simulations.

(n,m)	$L_0$ (10 nm)	$L_0$ (20 nm)	$L_0$ (30 nm)
(27,27)	$212.8 \pm 3.8$	$215.8 \pm 2.8$	$211.1 \pm 2.3$
(41,41)	$220.0 \pm 3.2$	$217.0 \pm 2.3$	$213.2 \pm 1.8$
(56,56)	$219.0 \pm 2.7$	$217.4 \pm 1.9$	$216.2 \pm 1.6$
(34,34)@(27,27)		$217.7 \pm 1.8$	
(47,0)	$214.1 \pm 3.9$	$211.1 \pm 2.7$	$213.3 \pm 2.2$
(71,0)	$213.4 \pm 3.2$	$216.0 \pm 2.4$	$218.9 \pm 1.9$
(97,0)	$220.3 \pm 2.8$	$220.0 \pm 1.9$	$219.4 \pm 1.6$
(59,0)@(47,0)		$213.4 \pm 1.9$	

Table 7-3. Calculated torsional shear moduli (in GPa) from torsion simulations.

(n,m)	$L_0$ (10 nm)	$L_0$ (20 nm)	$L_0$ (30 nm)
(27,27)	$73.4 \pm 0.3$	$73.4 \pm 1.0$	$76.4 \pm 1.8$
(41,41)	$79.6 \pm 0.3$	$81.8 \pm 1.1$	$83.8 \pm 1.9$
(56,56)	$82.7 \pm 0.4$	$85.0 \pm 1.2$	$83.2 \pm 2.2$
(34,34)@(27,27)		$81.2 \pm 0.5$	
(47,0)	$77.1 \pm 0.3$	$81.2 \pm 1.0$	$83.0 \pm 1.7$
(71,0)	$79.4 \pm 0.4$	$81.1 \pm 1.0$	$85.4 \pm 1.9$
(97,0)	$80.7 \pm 0.4$	$85.7 \pm 1.2$	$85.6 \pm 2.0$
(59,0)@(47,0)		$84.3 \pm 0.5$	

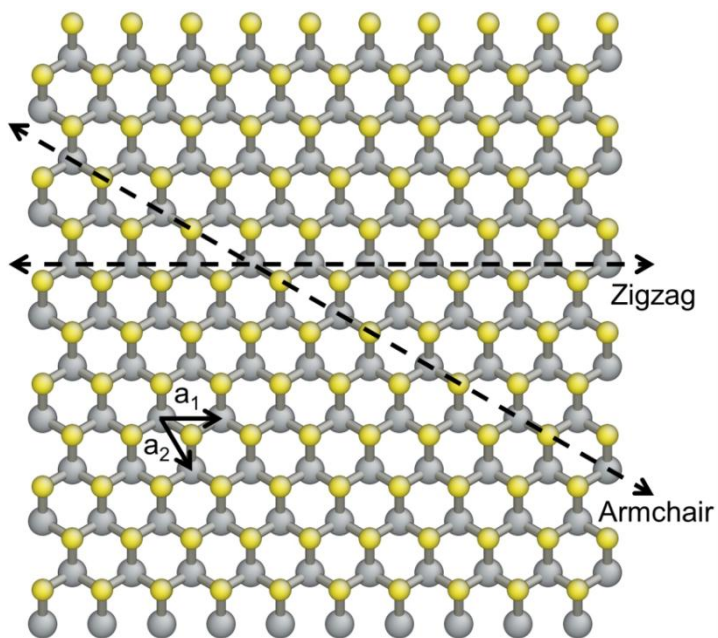


Figure 7-1. Hexagonal MoS<sub>2</sub> lattice indicating the  $a_1$  and  $a_2$  unit vectors and the directions for wrapping of armchair and zigzag nanotubes. Yellow atoms are S and grey atoms are Mo.

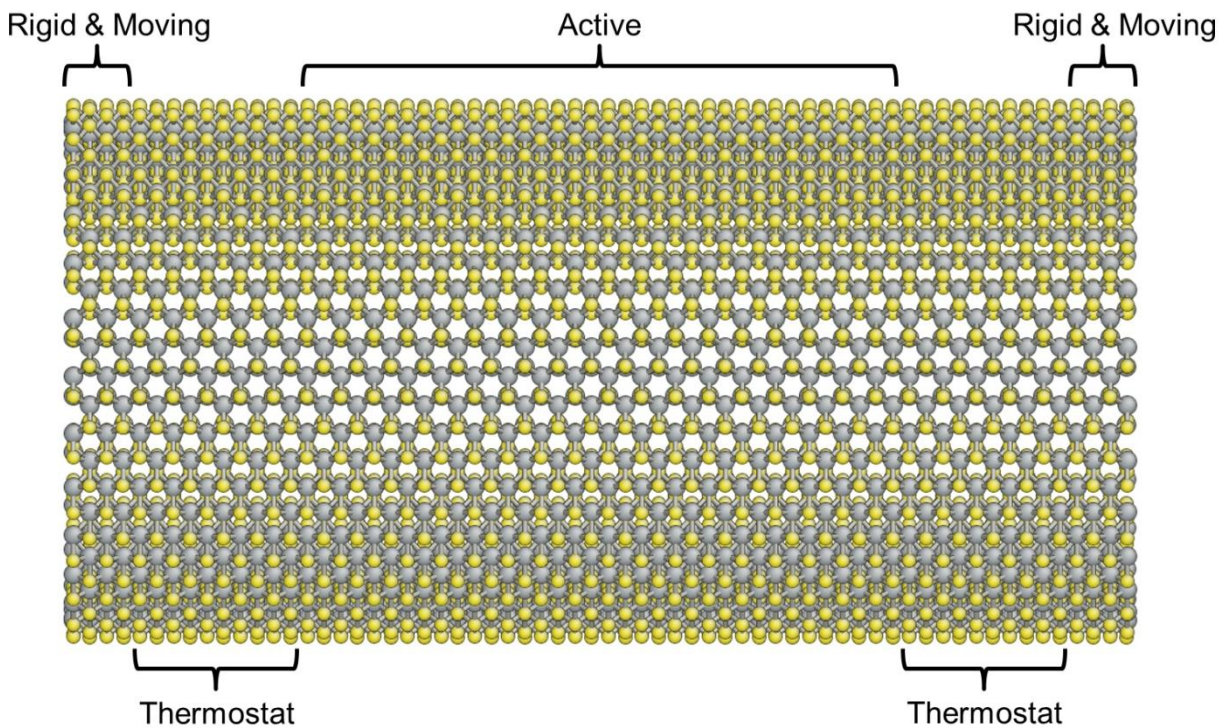


Figure 7-2. Initial structure of 10 nm (27,27) SWINT showing regions of rigid and moving, thermostat, and active atoms for compression, tension, and torsion simulations.

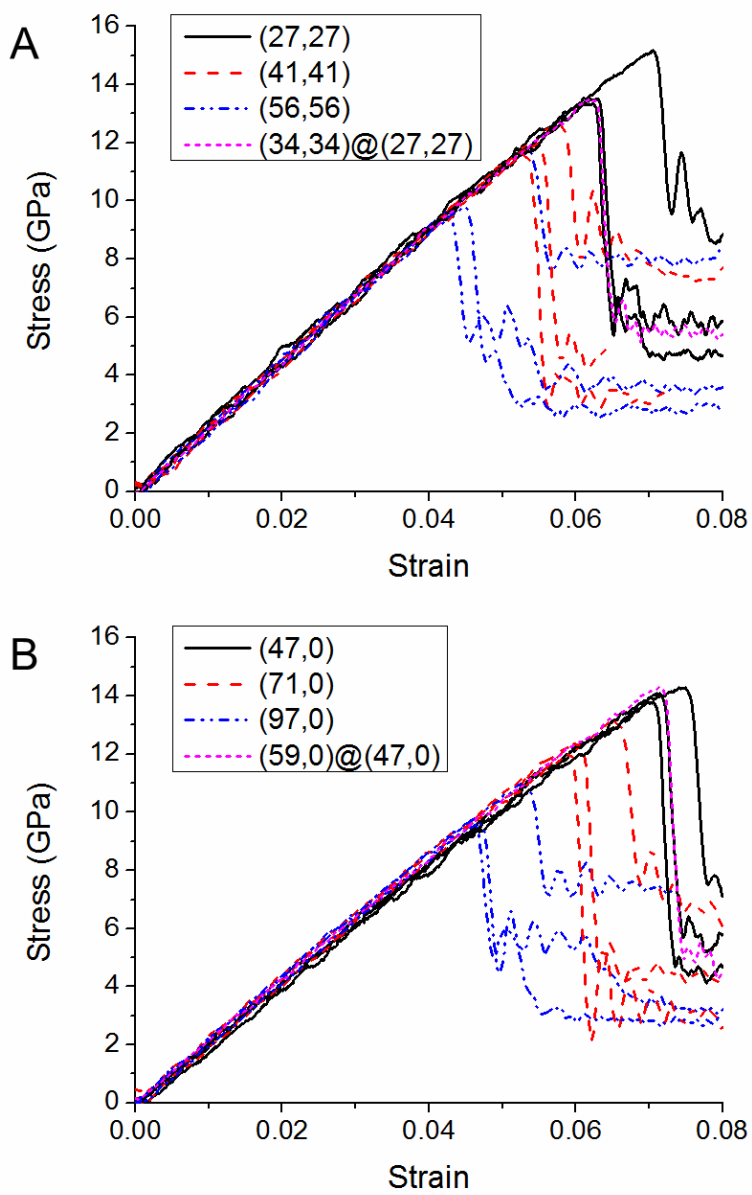


Figure 7-3. Stress versus strain during compression of A) armchair and B) zigzag SWINTS and DWINTS. Different lines for the same indices correspond to the different lengths of 10, 20, and 30 nm.

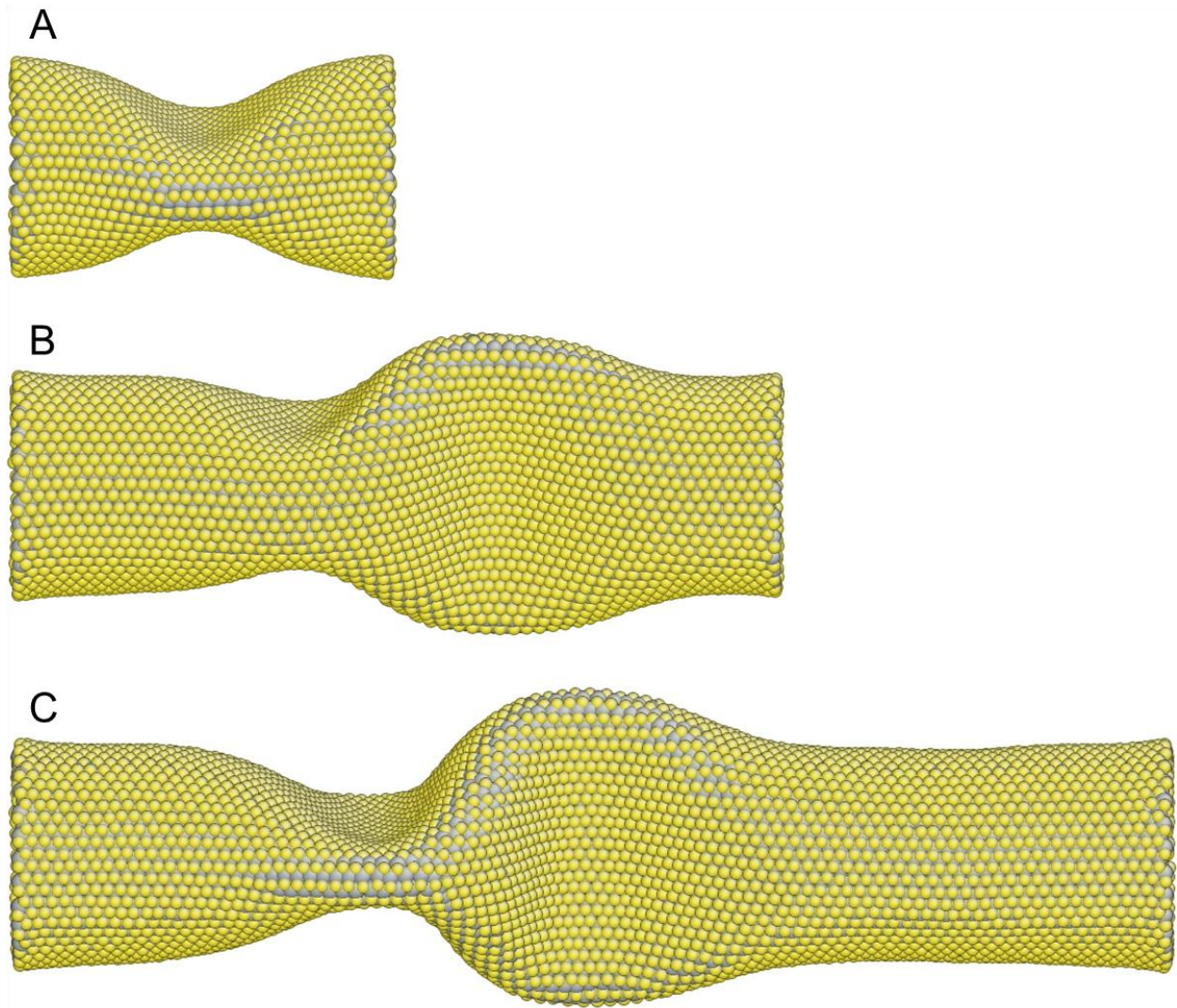


Figure 7-4. Snapshots of compressed (27,27) armchair SWINTs after buckling at 0.08 strain with initial lengths of A) 10 nm, B) 20 nm, and C) 30 nm.

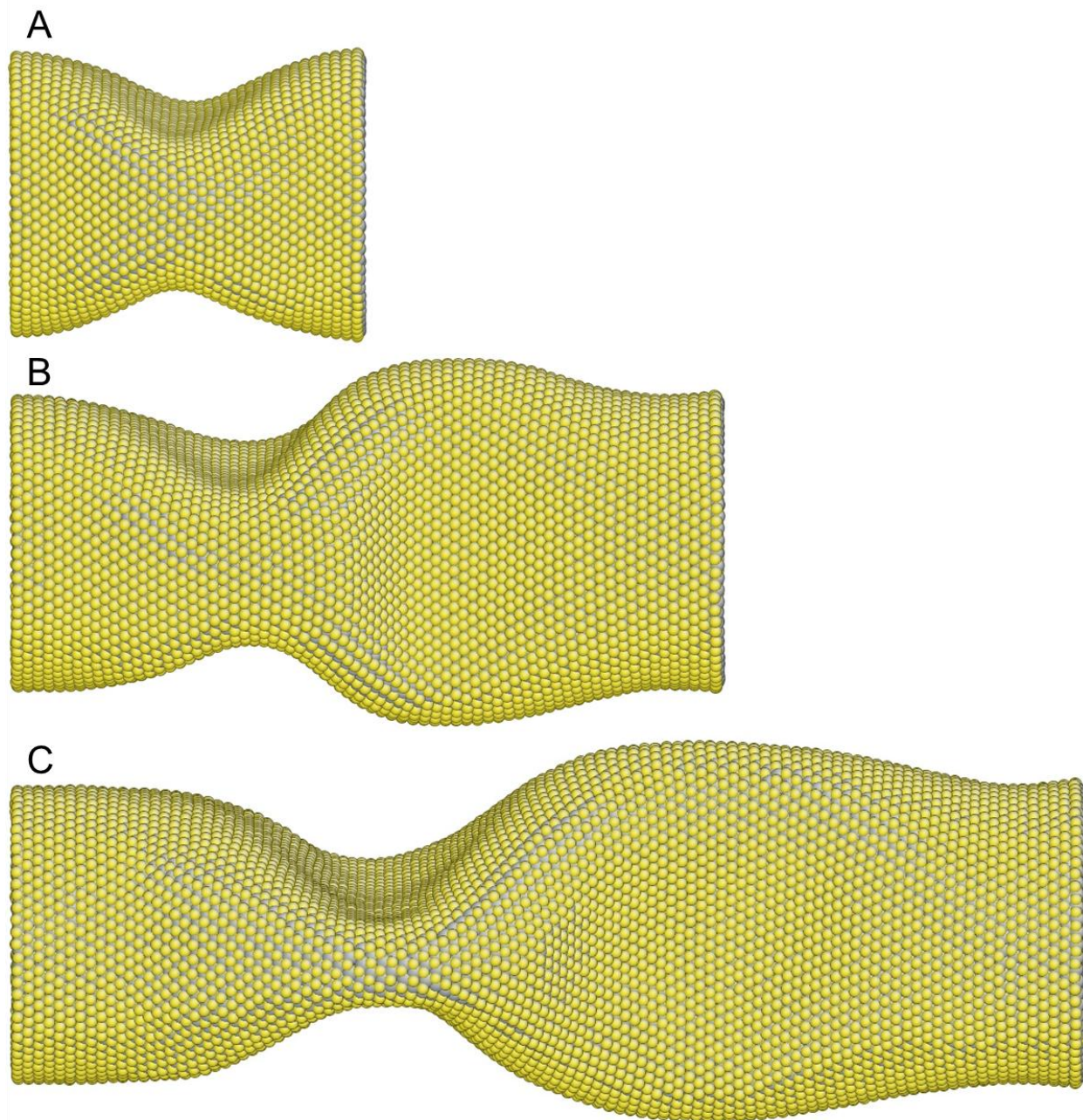


Figure 7-5. Snapshots of compressed (71,0) zigzag SWINTs after buckling at 0.08 strain with initial lengths of A) 10 nm, B) 20 nm, and C) 30 nm.

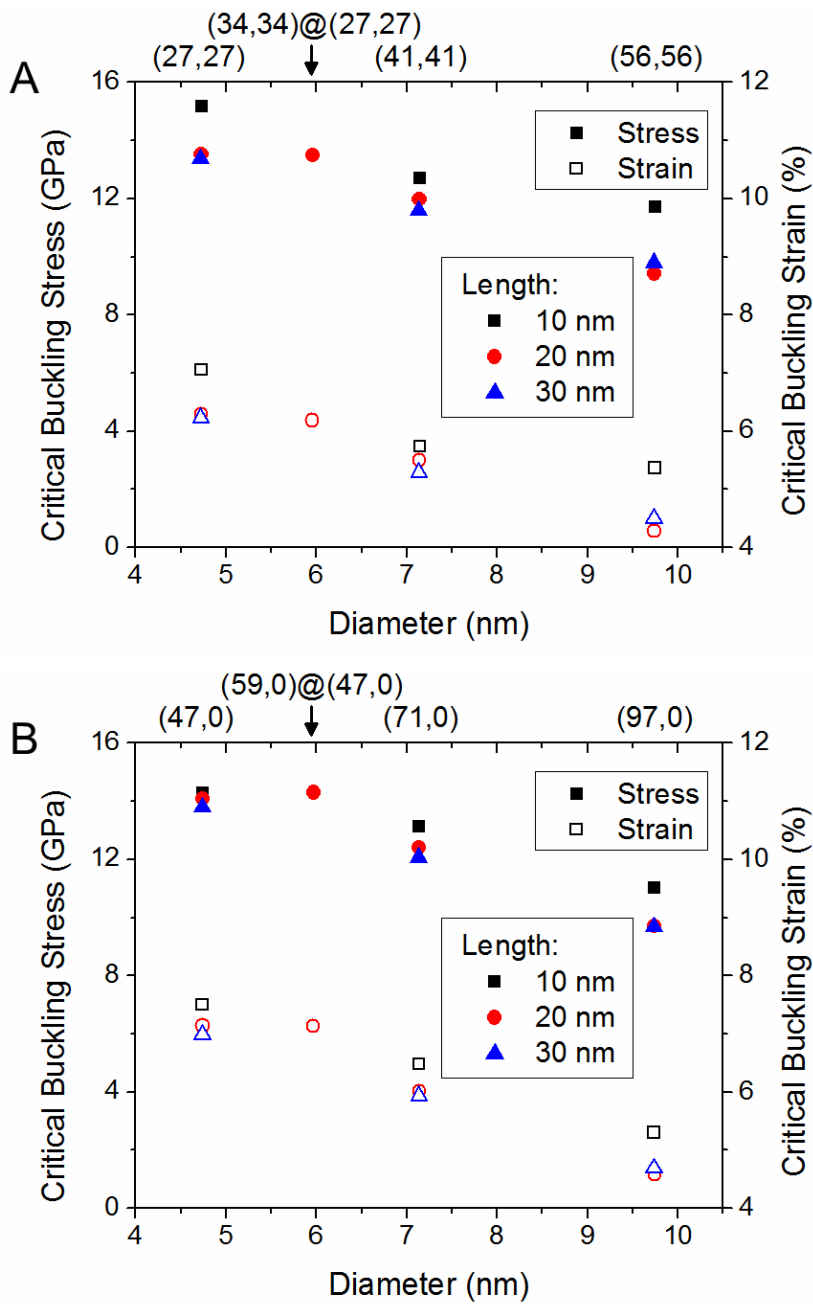


Figure 7-6. Comparison of critical stress and strain at the buckling point during compression of A) armchair and B) zigzag INTs.

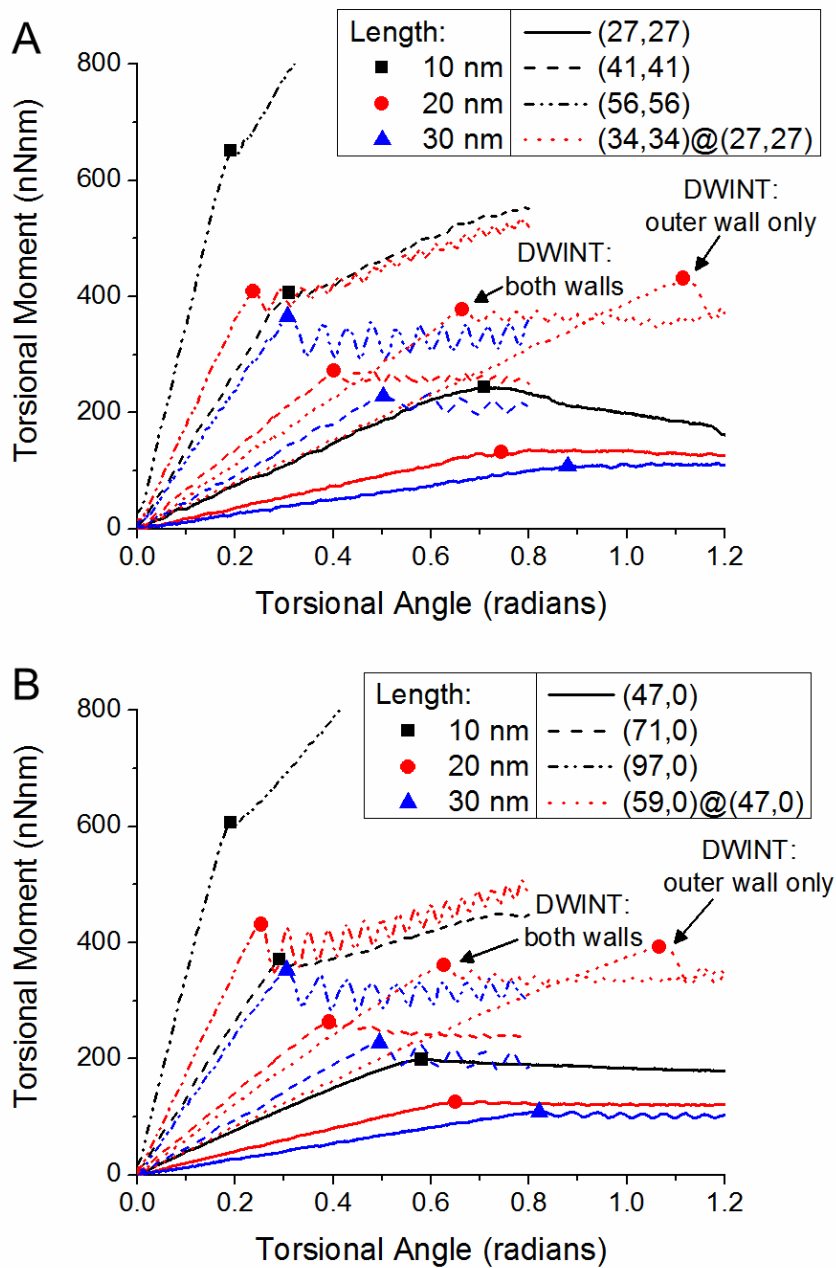


Figure 7-7. Torsional moment versus torsional angle of A) armchair and B) zigzag SWINTS and DWINTS during applied torsion. Scatterpoints indicate critical buckling moment.

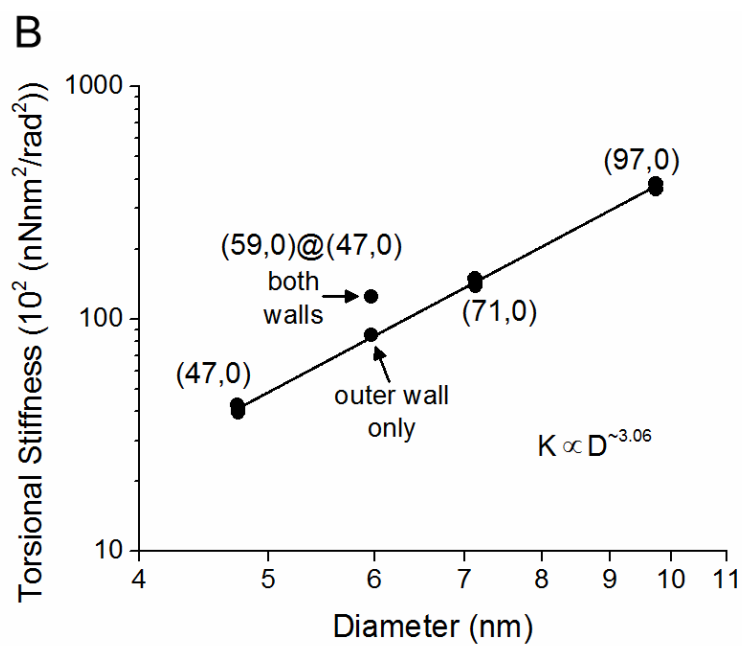
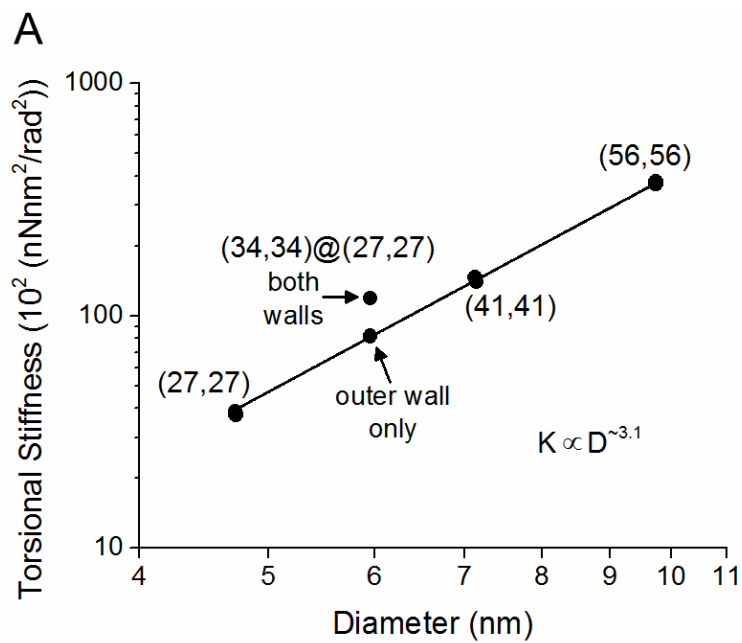


Figure 7-8. Relationship between torsional stiffness and diameter for A) armchair and B) zigzag INTs.

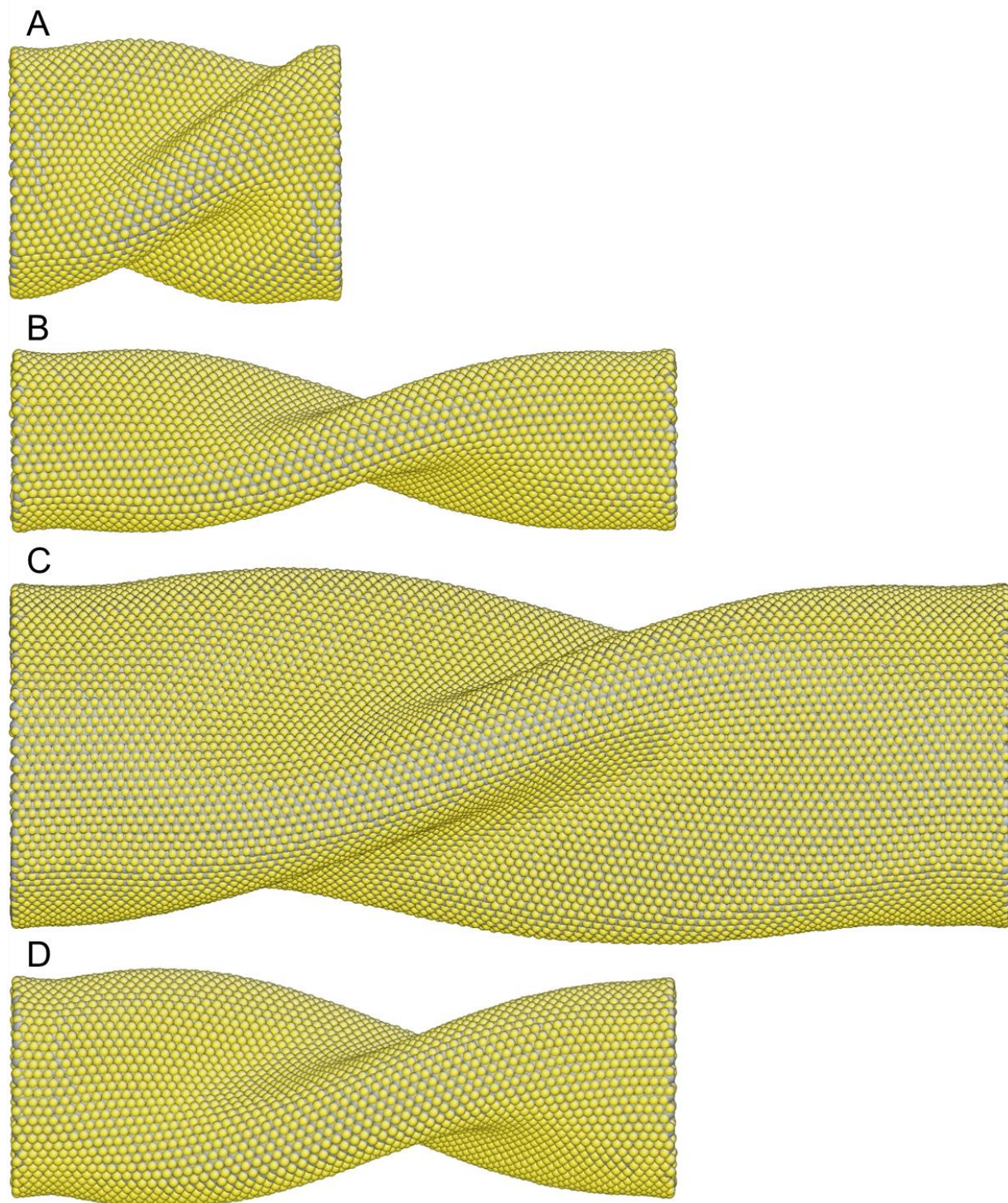


Figure 7-9. Snapshots of INTs after torsional buckling for A) 10 nm (41,41) SWINT at 0.8 radians torsion, B) 20 nm (27,27) SWINT at 1.2 radians torsion, C) 30 nm (56,56) SWINT at 0.8 radians torsion, and D) 20 nm (34,34)@(27,27) DWINT at 1.6 radians torsion.

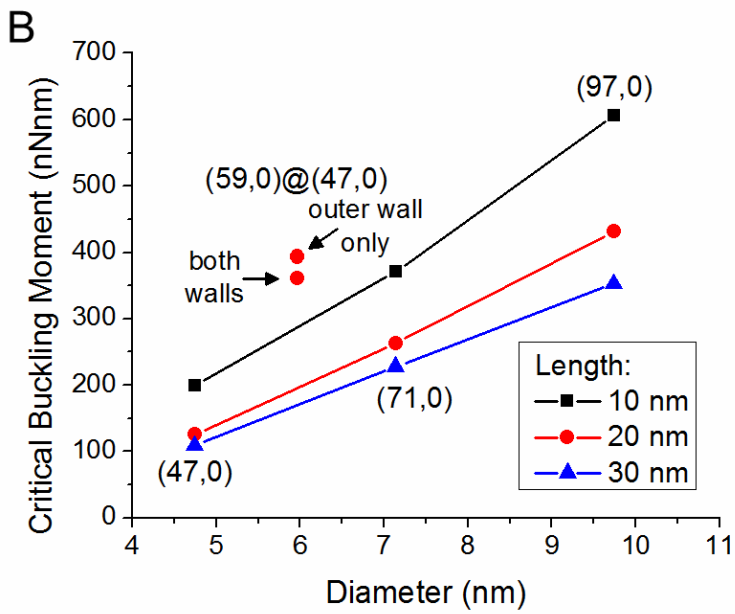
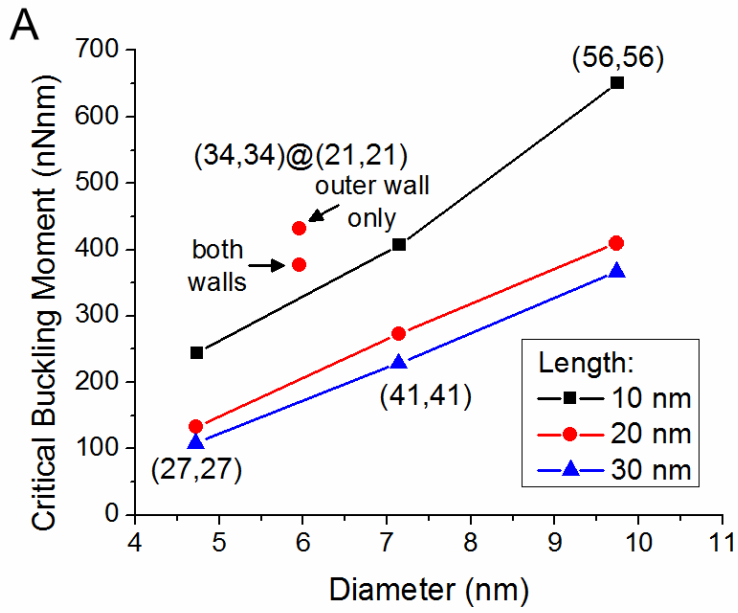


Figure 7-10. Critical buckling moment relative to the length and diameter of A) armchair and B) zigzag INTs.

## CHAPTER 8 ATOMIC-SCALE FRICTION AND WEAR OF PYROPHYLLITE\*

With the traditional selection of solid lubricants for tribological applications typically including lamellar materials such as graphite, metal dichalcogenides, and boron nitride, it is a reasonable hypothesis that new candidate solid lubricant materials that are likely to exhibit good frictional behavior will have comparable structural properties. Layered silicates such as pyrophyllite, talc, montmorillonite, illite, and muscovite possess a similar lamellar structure characterized by weak interlayer bonding. The basic intralayer structure for these lamellar silicates is a layer of octahedrally coordinated cations such as  $\text{Al}_2\text{O}_3$  sandwiched between two hexagonal layers of silicate ( $\text{SiO}_4$ ) tetrahedra forming strong composite lamellar sheets [165-168] as is illustrated in Figure 8-1. The diversity between the various layered silicate minerals results from the substitution of different cations within the lamellar sheets resulting in a net negative charge within the layers [166]. These net negative intralayer charges are balanced by the formation of additional cations within the interlayer space which leads to significant charge between the layers resulting in minerals that exhibit higher friction [169].

Of the available layered silicate minerals, pyrophyllite,  $\text{Al}_2\text{Si}_4\text{O}_{10}(\text{OH})_2$ , is one of the best candidates for solid lubrication because it contains no cation substitutions and, thus, has no interlayer charge which should allow for optimum frictional performance [165-167, 169, 170]. Pyrophyllite has its name derived from the Greek words “pyro” and “phyllo” meaning “fire” and “leaf,” respectively, due to the tendency for the silicate sheets to exfoliate during heating [168]. It is commonly used in many industrial

---

\* Adapted from Bucholz, E.W., Zhao, X., Sinnott, S.B., Perry, S.S.: Friction and wear of pyrophyllite on the atomic scale. *Tribol. Lett.* **46**, 159-165 (2012) [164]

applications including in cosmetics for its lustrous properties as well as in ceramics and refractories because of its exceptional insulating properties [168, 171].

The frictional properties of many silicate materials have been investigated, with most studies carried out within the context of geological research, which examines the effect these layered silicate minerals have on the shear events occurring in fault gouges [169, 172-175]. A study by Moore *et al.* [169] indicates that the frictional strength of these minerals is directly related to the strength of the bonds oriented in the (001) direction since shear occurs along the basal plane. This study further indicates that the weakest interlayer interactions belong to talc and pyrophyllite since these minerals have no cation inclusions within the interlayer space. Similarly, another study by Colletini *et al.* [173] provides evidence that fault zones are weakened by the formation of phyllosilicate-rich interconnects along the surface where shear will occur. Each of these findings show that the structure of phyllosilicates, particularly that of pyrophyllite, contributes to the onset of slip due to fault weakening. As such, these results highlight the opportunity for fundamental studies of layered silicate materials from the perspective of establishing the atomic-scale details of friction and wear within such structured materials.

Other non-geological research exploring the frictional properties of layered silicate minerals is much more limited. Some studies have shown that talc acts as a sufficient reducer of wear, frictional heating, and friction coefficient when added at around 5 wt.% as a lubricant additive in base oils [176, 177]. At the atomic-scale, another member of the phyllosilicate family, muscovite mica, is sometimes used as a reference material within the AFM because it is readily available and well known to cleave atomically flat

surfaces due to its structure [79, 178]. Also, both computational [179] and experimental [180] studies have shown that self-mated talc and muscovite mica (001) surfaces, respectively, exhibit low friction forces when the surfaces are sliding in an incommensurate contact.

Here, we examine the atomic-scale frictional and wear properties of mineralogical pyrophyllite with atomic force microscopy (AFM) and compare them with the well-known properties of highly oriented pyrolytic graphite (HOPG). The AFM experiments discussed in this chapter were performed in collaboration with Dr. Xueying Zhao and Professor Scott Perry at the University of Florida.

### **Experimental Details**

Specific information regarding AFM and the details of the experiments discussed here are provided in detail in Chapter 2. In these experiments, a specimen of polycrystalline pyrophyllite mineral was cleaved and individual flakes from the interior of the mineral were selected for use during the friction tests. Tantalum strips were spot-welded to the sample holders over the edges of the pyrophyllite flakes to secure them during testing. For the HOPG samples, freshly cleaved basal planes were produced by forming a uniform adhesion between the HOPG and scotch tape thus removing the layers nearest the surface when the tape was removed. Using these samples, the topographical imaging and friction measurements were performed using an AFM equipped with a four-quadrant photodetector that allowed for the simultaneous measurements of the normal and lateral force fluctuations. The frictional properties were calculated by measuring the normal and lateral forces acting between the pyrophyllite or HOPG samples and a triangular cantilever with a  $\text{Si}_3\text{N}_4$  tip at ambient pressures and in a dry nitrogen environment with less than 3% relative humidity.

The friction experiments were carried out by positioning the pyrophyllite or HOPG samples on a piezoelectric tube scanner, translating the sample relative to the fixed AFM tip, and measuring the forces as a function of increasing and decreasing applied loads; specifically, the friction scans were collected over lengths of 100 nm at a rate of 1  $\mu\text{m/s}$ . In a similar manner, the threshold to interfacial wear of the pyrophyllite surface was investigated by collecting topographic images at sequentially increasing loads and noting the differences in the imaged structure as an indication of the onset of interfacial wear. In order to calculate the shear stress during the friction experiments, defined as the friction force divided by the contact area, we used the Derjaguin-Muller-Toporov (DMT) model to approximate the contact area between the  $\text{Si}_3\text{N}_4$  tip and the pyrophyllite/HOPG surface [181]. For this method, the contact area was determined by:

$$A(L) = \pi \cdot \left( \frac{R \cdot L}{K} \right)^{\frac{2}{3}} \quad (8-1)$$

where  $R$  is the tip radius which was 37.4 nm,  $L$  is the normal load, and  $K$  is the combined elastic modulus, which was determined by:

$$K = \frac{4}{3} \cdot \left[ \frac{1 - \nu_{1,2}^2}{E_{1,2}} + \frac{1 - \nu_3^2}{E_3} \right]^{-1} \quad (8-2)$$

For pyrophyllite, the elastic modulus  $E_1$  is 23.5 GPa [182]. The Poisson's ratio  $\nu_1$  for pyrophyllite is assumed to be 0.25 since, to our knowledge, an appropriate value for the Poisson's ratio of cleaved, crystalline pyrophyllite is not readily available; this is a reasonable approximation since varying the value of Poisson's ratio results in changes for the calculated shear stress of only a few percent. For HOPG, the Poisson's ratio  $\nu_2$

is 0.25 with an elastic modulus  $E_2$  of 36.5 GPa [183]. And for the  $\text{Si}_3\text{N}_4$  tip, the Poisson's ratio  $\nu_3$  is 0.2 with an elastic modulus  $E_3$  of 200 GPa [184].

### **Surface Characterization**

In order to characterize the surface structure of the pyrophyllite samples, an x-ray diffraction (XRD) analysis was performed by Dr. Valentin Craciun at the University of Florida, and the results are given in Figure 8-2. This analysis indicated that the exfoliated pyrophyllite surface corresponds to the (001) basal plane of the crystal structure with the individual grains being highly textured along the [001] direction, consistent with numerous steps across the cleaved surface. The simultaneous appearance of diffraction peaks corresponding to the (002), (004), (006), (008), (0010), and (0012) planes are indicative of the basal orientation of the layered compound. Peaks of lesser intensity are believed to arise from peripheral regions of the very small sample. These XRD results confirmed that the atomic-scale friction properties of pyrophyllite were investigated along the low-shear, cleavage plane. Since the basal surface of cleaved graphite has been extensively documented through various microscopy techniques [185-188], surface characterization of the HOPG sample was not performed in this study.

Through topographical imaging with the AFM, we found that the cleaved mineralogical pyrophyllite sample exhibits a step-terrace structure as seen in Figure 8-3, which is consistent with the lamellar nature of the aluminosilicate crystal structure. We analyzed the surface topography through a statistical approach in order to demonstrate the layered nature of the sample (Figure 8-4). As is indicated from the data, the majority of the steps were small and corresponded to only one or two lattice displacements

(9.347 Å [170]); in some instances, observed steps were quite large and corresponded to more than six lattice displacements. This correlation between lattice displacements and measured step heights from the topographical analysis quantified that the pyrophyllite surface corresponded to that of the low energy (001) basal plane which is in agreement with the XRD analysis discussed previously (Figure 8-2).

## **Friction and Wear Analysis**

### **Atomic-Scale Friction**

On the terraced planes in regions away from steps, multiple friction experiments were performed across the pyrophyllite and HOPG surfaces and averaged. In particular, the friction forces were measured on the (001) terraces of both materials in the absence of wear which was confirmed by topographical imaging of the surface following the friction tests. Figure 8-5A shows a comparative analysis of the friction load ramps measured on pyrophyllite and graphite using the same probe tip and cantilever sensor. A linear slope analysis of the data for the friction measured between the Si<sub>3</sub>N<sub>4</sub> tip and HOPG, averaged over six data sets, resulted in a microscopic coefficient of friction of  $\mu \sim 0.003$  which is comparable to results reported in the literature (0.002 [178], 0.004 [189, 190], and 0.007 [80]). For the pyrophyllite friction experiments, the results were analyzed over nine separate measurements and indicated a friction coefficient of  $\mu \sim 0.03$  for the sliding contact of Si<sub>3</sub>N<sub>4</sub> with this silicate terrace. The results for HOPG are presented here primarily to demonstrate that the data measured for pyrophyllite are well above the noise threshold for the experimental approach employed.

In some instances, the analysis of friction coefficients can be problematic as a result of significant influences of tip geometry, adhesion, and area of contact. Interfacial shear stress represents a more fundamental measurement that, despite being a

function of counterface material and environment, provides improved comparison between materials. In order to further characterize the atomic-scale friction properties of the pyrophyllite and HOPG samples, we calculated the average shear stress during the friction experiments by approximating the contact area using the DMT model described in Equation 8-1. The results of this analysis are shown in Figure 8-5B where the calculated shear stresses for the sliding contact of the  $\text{Si}_3\text{N}_4$  single asperity and the surfaces of pyrophyllite and HOPG were found to be approximately 39.5 MPa and 2.3 MPa, respectively. This shear stress for HOPG is in good agreement with typical published values which range from 0.9 to 2.5 MPa [191], supporting the accuracy of our calculations, while that measured for pyrophyllite falls into the category of being very low. The combined analysis of pyrophyllite's friction coefficient and interfacial shear stress confirm the lubricity of this termination of the layered silicate compound under dry conditions.

Values for the shear stress of different commonly used solid lubricants have been reported over the years. For sputter-deposited lamellar  $\text{MoS}_2$  films, the shear stress during friction in a dry air environment varies in the literature from 24.8 MPa [192] to around 40 MPa [193, 194]. A value for the shear stress of an amorphous hydrocarbon film has been reported at approximately 200 MPa [195]. Meanwhile, soft metals such as lead and tin are generally reported with values on the order of 25-40 MPa [196]. Although the shear stress calculated for pyrophyllite is greater than that of HOPG, it is on the order of some of the other commonly used solid lubricant materials, highlighting the potential for use of pyrophyllite in tribological applications.

## Threshold for Interfacial Wear

The tribological properties of pyrophyllite were further investigated through an analysis of its atomic-scale wear properties. Using the  $\text{Si}_3\text{N}_4$  AFM tip as a model for a single microasperity, the threshold to material damage on the pristine pyrophyllite terraces was determined through the following procedures. First, a 10 nm by 10 nm area on an isolated terrace was imaged under sequentially increasing loads with increments of 10 nN, which allowed for the rastering of the tip across an isolated portion of the sample. At this length scale and on the crystalline terrace, the stick-slip motion of the cantilever revealed the periodicity of the lattice as is shown in the lower portion of the lateral force image in Figure 8-6A. In some cases, while collecting images under higher loads, these periodic features disappeared as was the case in Figure 8-6A at an applied load of 220 nN; the data in this image was collected from bottom to top. Upon observation of these events, the next step was to image the surrounding area (100 nm by 100 nm) at low applied load which revealed the atomic-scale damage (bond breaking) that had occurred within the silicate layer as is shown in Figure 8-6B. In this image, the central dark feature represents a depression of atomic-scale dimension formed in the sample as a result of the tip-sample interaction under high applied load. The surrounding bright regions indicate material that had been removed from the depression and was resting on the original terrace. Repeating this approach in multiple regions of the sample, it was statistically determined that the onset of wear of the pyrophyllite terrace occurred at approximately 200 nN for contact with a 40 nm radius probe tip; this corresponds to a threshold for material wear of  $\sim 1.6$  GPa.

## Discussion

Since published research on the atomic-scale friction of layered silicate minerals is limited, it is difficult to place the properties of pyrophyllite discussed here in context with other mineralogical materials. Through review of the available literature, it has been shown through surface force apparatus experiments in dry air that muscovite mica has a friction coefficient of 0.35 [197]. For fault gouge experiments, it is shown that the friction coefficient of a talc gouge is around 0.24 [175]; similar experiments showed that a serpentinite gouge comprised of various serpentine minerals such as antigorite, lizardite, and chrysotile displays a friction coefficient of about 0.23 [174]. The friction coefficient we report for pyrophyllite of about 0.03 is an order of magnitude lower than the coefficients of friction for similar minerals mentioned above.

The differences between the friction coefficient we obtained for pyrophyllite and those of similar minerals from the literature can be explained by the nature of the AFM experiments presented here. These experiments reflect the frictional properties of mineralogical pyrophyllite samples measured at the atomic-scale on pristine terraces in the absence of wear which is quite different from the conditions of friction at the macro-scale [197, 198]. In macroscopic scale evaluations, many crystallographic orientations are sampled as well as grain boundaries and structural defects. As such, the encounter with these structures provides the opportunity for additional pathways for energy dissipation, namely wear through plastic deformation, thus enhancing the frictional response. This change in friction performance at the onset of wear has been demonstrated by Gosvami *et al.* [199] who documented a large increase in the friction forces on Cu(100) and Au(111) surfaces when wear begins; similarly, an AFM study of PbS(100) showed that the friction coefficient is less than 0.05 in the absence of wear

and increases to about 0.35 during continual wearing of the surface [77]. In addition, Liu *et al.* [80], through macro-scale fretting tests, indicated that mica has a friction coefficient of up to 0.52 with visible wearing and plastic deformation at the interface; this same study showed that, during nano-scale AFM, mica has a friction coefficient of 0.045 with no evidence of interfacial wear. Furthermore, the presence of water on various pyrophyllite surfaces and planes during macro-scale measurements also contributes to the difference between the AFM friction results presented here and previous characterizations of pyrophyllite found in the literature. As such, the atomic-scale friction coefficient reported here of approximately 0.03 is consistent with pyrophyllite possessing low friction planes under dry conditions, but it is not a sufficient qualifier of the tribological properties of this material.

Rather, it is necessary to also consider the wear properties of pyrophyllite. Here we have reported that interfacial wear was not observed during the course of friction measurements. On the contrary, the measurements performed at significantly higher applied loads identified a wear threshold of 1.6 GPa; the yield strength of many silicate-based rocks is in the range of 10-500 MPa [200]. While this seems to imply that pyrophyllite should be a wear resistant material, it is important to recall the atomic-scale nature of measurements performed with the AFM. The threshold for wear we reported here relates to the energy needed to break chemical bonds within a single layer of pyrophyllite, while macroscopic yield strengths effectively sample many orientations of a given structure as well as the interactions between layers of that structure. Considering the layered structure of pyrophyllite along with the low friction exhibited at certain

crystallographic faces, it is expected that macroscopic investigations would find a much lower tolerance for interfacial wear.

### **Summary**

As a result of the structural properties of layered silicate minerals, pyrophyllite has been evaluated as a candidate for solid lubrication. Since it possesses no interlayer charge, the low energy basal plane is predominantly characterized by weak van der Waals interactions. These structural properties suggest the opportunity for low energy interfacial interactions. We have tested this theory by performing friction experiments using an AFM which demonstrate the atomic-scale tribological properties of cleaved samples of mineralogical pyrophyllite. These experiments have indicated that, in the absence of wear, pyrophyllite exhibits a coefficient of friction of approximately 0.03 and a shear strength of 39 MPa when measured in contact with silicon nitride which is comparable with other materials employed as solid lubricants. The detection of an atomic-scale threshold to wear in excess of the yield strength of many minerals is consistent with the nature of atomic bonding within silicate layers and the known energetics of macroscopic materials deformation. Together, these findings suggest the opportunity for employing pyrophyllite as a tribological material in instances where it is not necessary for the mineral to provide full load support of the moving contacts. Further investigation of the wear properties of pyrophyllite at the macro-scale would help to evaluate this possibility.

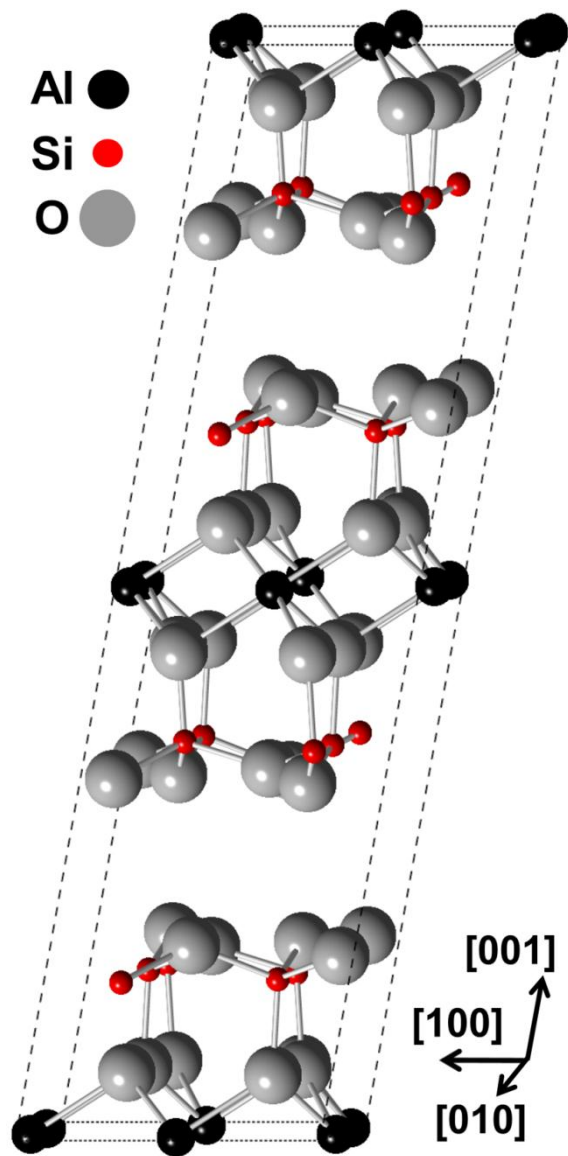


Figure 8-1. Schematic representation of the crystal structure for the aluminosilicate mineral pyrophyllite. The dashed line highlights a region containing two unit cells and the respective location of the van der Waals gap in the structure.

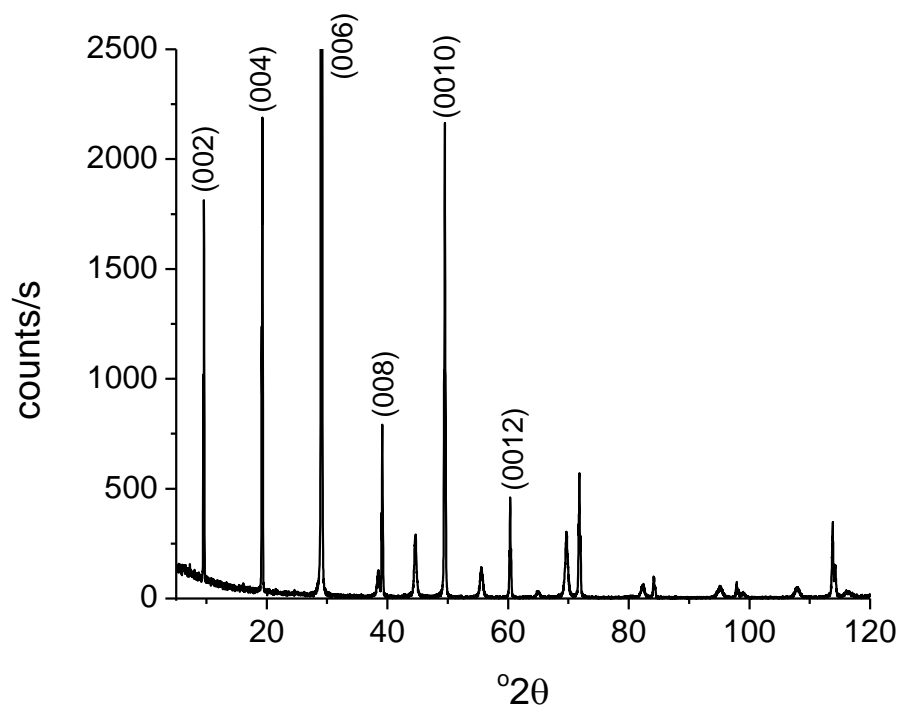


Figure 8-2. XRD analysis of a cleaved pyrophyllite flake. Labeled peaks correspond to crystallographic pyrophyllite planes oriented parallel to the surface plane.

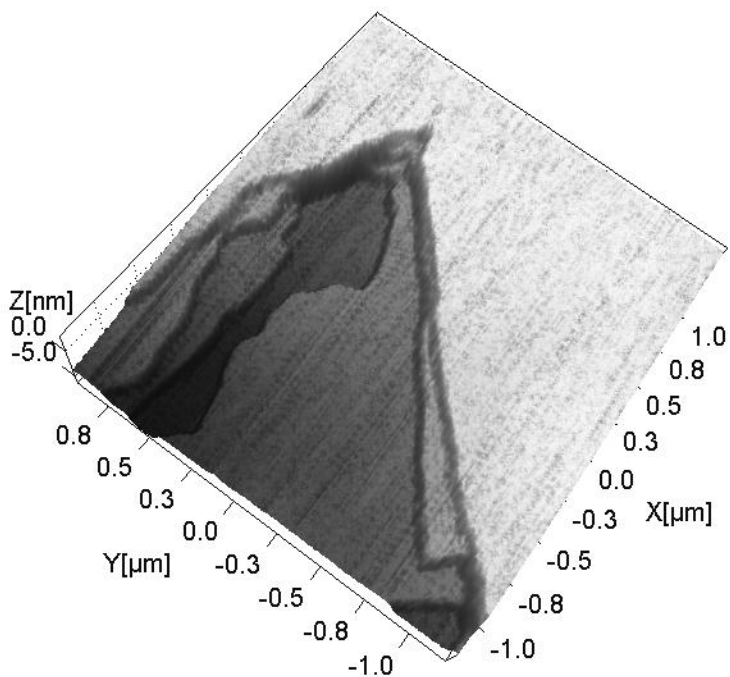


Figure 8-3. 3-D topographical AFM image of pyrophyllite illustrating the step-terrace nature of the surface observed on the nanometer scale.

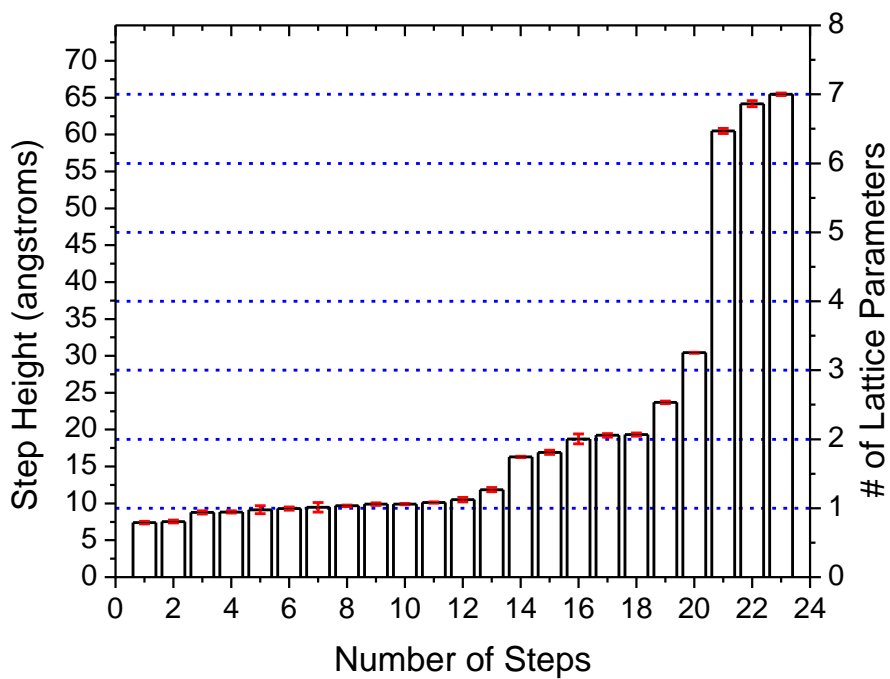


Figure 8-4. Topographical step height analysis for individual steps across the pyrophyllite surface.

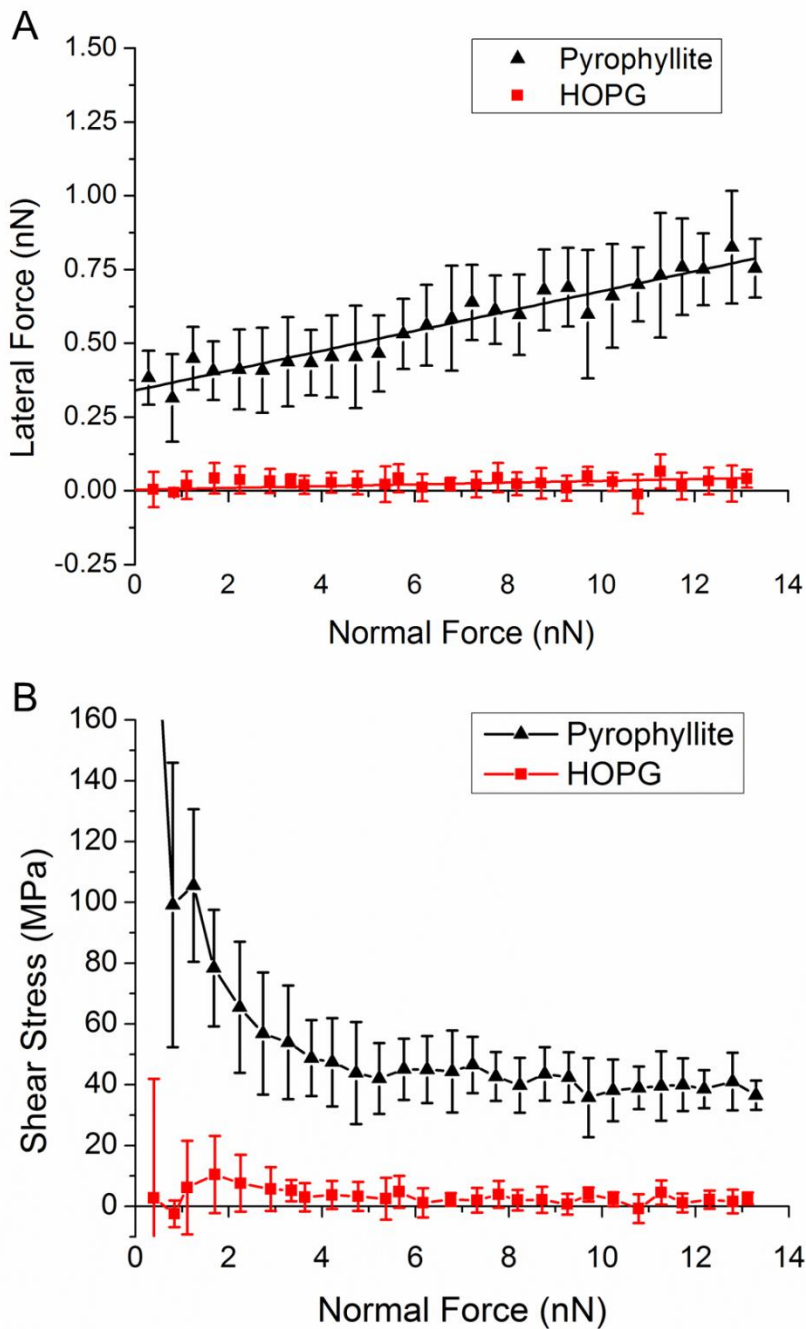


Figure 8-5. Analysis of AFM friction experiments. A) Friction load ramps measured for the sliding contact of pyrophyllite and HOPG basal planes against a  $\text{Si}_3\text{N}_4$  probe tip. B) Interfacial shear stresses as a function of load for pyrophyllite and HOPG sliding against the microscopic probe tip determined from the friction load ramp data and a calculation of the interfacial contact area.

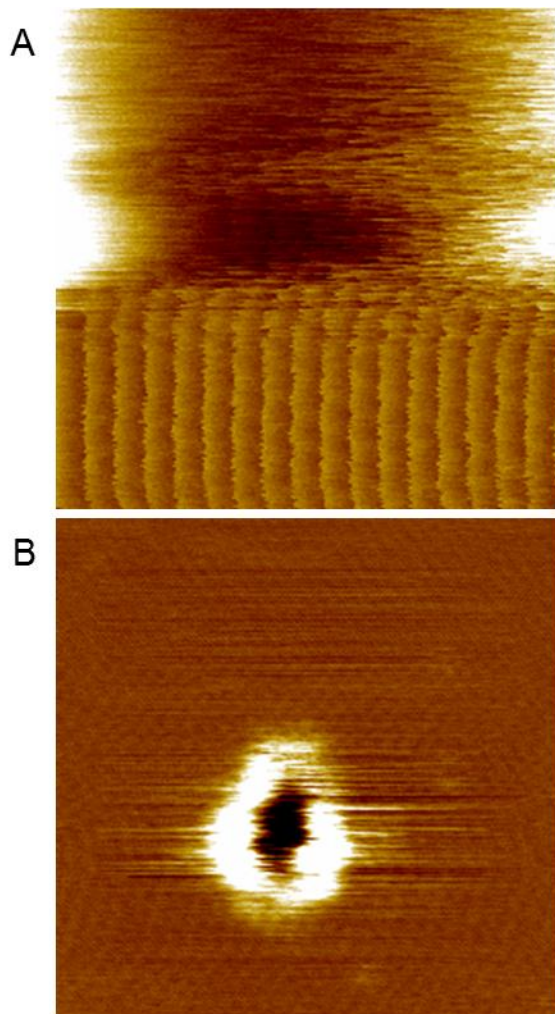


Figure 8-6. AFM images of atomic-scale wearing of the pyrophyllite surface. A) 10 nm by 10 nm lateral force image of the pyrophyllite surface, collected at an applied load of 220 nN scanning from bottom to top, reveals the stick-slip motion of the tip across the pyrophyllite lattice and the onset of interfacial wear through the loss of this resolution. B) 100 nm by 100 nm topographic scan of the region immediately surrounding where the wear was induced indicates the plastic deformation of the surface plane under these sliding conditions.

## CHAPTER 9 DATA-DRIVEN MODEL FOR ESTIMATION OF FRICTION COEFFICIENT\*

In mechanical design, the ability to accurately predict the tribological behavior of individual mechanical components is essential for maximizing performance [202]. As such, an appropriate set of guidelines for estimating the friction coefficients of new materials will be of great benefit when designing parts for applications where surfaces will be in sliding contact. Experimentally, the frictional response of a material is determined using methods such as the surface force apparatus (SFA) [197, 203, 204], atomic force microscopy (AFM) [77, 197, 205, 206], and tribometry [143, 207, 208]. Additionally, computational approaches, including molecular dynamics (MD) [22, 60, 65] and density functional theory (DFT) [100, 209], have been shown to provide atomic-level information regarding the frictional behavior of materials. With the present progression of modern technologies, an advancement of the means for the rapid discovery of the frictional responses of materials is of the utmost importance. An important tool for modern materials research is materials informatics which combines data mining, statistical inference, and materials science in order to accelerate the rate of new material design and discovery. Through materials informatics methods, it is possible to identify hidden relationships in a large collection of complex data and to correlate these relationships as predictive rules for the development of new materials for use in desired applications.

In the field of tribology, several properties of ceramic materials, some of which are candidate high-temperature, solid-state lubricants, have been linked to friction

---

\* Adapted from Bucholz, E.W., Kong, C.S., Marchman, K.R., Sawyer, W.G., Phillpot, S.R., Sinnott, S.B., Rajan, K.R.: Data-driven model for estimation of friction coefficient via informatics methods. *Tribol. Lett.* **47**, 211-221 (2012) [201]

coefficient. For example, a study by Erdemir [210] shows that there is an inverse relationship between a solid oxide's friction coefficient and its ionic potential, which is defined as the ratio of the material's cationic charge to the cationic radius. For materials with a higher ionic potential, there is strong screening of the cations by the surrounding anions resulting in the cations having little to no chemical interactions with other cations, in turn leading to lower friction coefficients. On the other hand, for materials with a lower ionic potential, the cation screening is reduced, which enables them to form strong ionic or covalent bonds that increase the friction coefficient. Another study indicates that solid oxides display a similar inverse correlation between friction coefficient and absolute electronegativity, since materials with higher electronegativity have a stronger hold on their binding electrons, which makes interfacial chemical bond formation more difficult and leads to lower friction coefficients [211].

From the above findings for solid-state oxides, we hypothesize that additional measurable correlations exist between intrinsic material properties and the friction coefficients of similar chalcogenide materials as well as less similar materials. For this work, we utilized a material dataset comprised of 16 different material properties for 38 inorganic ceramics and minerals, including a variety of binary chalcogenide minerals and other non-chalcogenides. Utilizing this dataset, we developed a robust and accurate data-driven model for estimating the friction coefficient of various classes of ceramic materials through the combined use of multivariate data mining algorithms for the selection of important model parameters and for the construction of predictive models.

For the remainder of this chapter, we begin by describing the experiments that were performed to obtain the friction coefficients used for some of the materials along with the details of the compilation of our material dataset. Next, we detail the results of the materials informatics methods used in this work. Finally, we discuss the data-driven model we have developed for estimating friction coefficient, including its advantages and the implications that could arise from its use.

## **Experimental Details**

### **Microtribometry**

The tribological properties of 24 ceramic samples, which are listed in Table 9-1, were investigated using a pin-on-disk tribometer; these experiments were carried out by Kellon Marchman, a graduate student from the University of Florida. Since some of these samples had a toxic nature, two different pin-on-disk tribometers were used, one under a fume extracting hood and another in a clean room environment. These experiments were performed in open air at an ambient temperature of 22°C and relative humidity of 25-40%. Contact pressures were attained in both cases using a dead-weight load of 1 N. The rotation of the pin-on-disk setup was obtained using a spindle attached to a servo motor which encompassed a rotary encoder for position feedback and was capable of speeds ranging from 0.3-500 rpm; in this manner, a linear sliding velocity of 50 mm/s was maintained in each experiment by adjusting the rotation rate based on the wear track radius which was varied using a calibrated motorized stage. Each experiment was performed until a steady state friction coefficient was reached with the friction forces being measured by a linear force transducer and a flexure with known calibration constants.

## **Samples and Preparation**

In order to acquire appropriate mineral samples for the tribometer experiments, multiple sample forms were required; specifically, we used three main types of sample forms as is indicated in Table 9-1. Sample set 1 included mineralogical samples which were set in one inch epoxy molds. After the epoxy was cured, the samples were polished in steps with aluminum oxide abrasive discs up to 1200 grit in order to expose the mineral specimen. These one inch disks were then mounted in the tribometer and run against a ruby sphere with a diameter of 6.35 mm. Sample set 2 was made up of single crystal optical windows which were used as the running surface. These optical windows are preferred surfaces in tribological experiments because of their high magnitude of flatness ( $2\lambda$  at 632.8 nm), high magnitude of parallelism ( $\leq 3.5$  arcminutes), and low surface roughness ( $R_a$  of 4.36 nm). The pin used against these optical windows was also a 6.35 mm diameter ruby sphere. For sample set 3, the mineral samples were crystalline pieces with sizes ranging from 3-6 mm; each of these samples was over 99.5% pure based on an assay of trace metals. Unlike sample sets 1 and 2, the minerals in sample set 3 were used as the running pin because of their small size. The substrates (disks) used for these experiments were sapphire optical windows with diameters of 25 mm. In order to avoid cross-contamination between samples, each experiment was performed at a different wear track radius on the sapphire window, and the optical window was cleaned with a laboratory wipe and methanol.

## **Data Compilation**

To develop our predictive model we used a material dataset comprised of 16 intrinsic properties for 38 different inorganic minerals (Table 9-2). The friction information for 24 of the minerals was obtained in the manner described in the previous

section while the friction coefficients for the remaining 14 minerals were obtained through a review of the available literature as indicated in the table. The selection of properties in the dataset was made in such a way that the material properties can be either easily attained or calculated so that the resulting model may be more readily utilized for predicting the friction coefficients of a database containing new materials. The compilation of the material properties included in the dataset shown in Table 9-2 was done with the assistance of Jonathan Liddy, a former undergraduate student from the University of Florida.

We calculated the ionic potential as the ratio of the mineral's cation charge to the cation radius as defined by Erdemir [210] where the cation charge is the formal charge necessary to balance the mineral's chemical formula. The percent ionicity was calculated as [212]:

$$\%IP = \left(1 - \exp\left(-0.25(\chi_A - \chi_B)^2\right)\right) \cdot 100 \quad (9-1)$$

where  $\chi_A$  and  $\chi_B$  are the electronegativity (EN) of the anion and the cation on the Pauling scale, respectively, with EN difference being the term,  $\chi_A - \chi_B$ , from Equation 9-1. From the crystal structures for each of the minerals, we defined the  $R_{ij}$  distance as the nearest neighbor bond length between cation and anion; we also determined interplanar spacing as the distance between adjacent planes of atoms, generally orthogonal to the cleavage plane. In order to determine the electrostatic potential energy for the minerals, we used the General Utility Lattice Program (GULP) [213] to calculate the single-point electrostatic lattice energy of a periodic unit cell of each mineral which we then normalized to the electrostatic potential energy per atom by

dividing by the number of atoms in the unit cell. From this electrostatic potential energy, we calculated the Madelung constant for the cation as [214]:

$$M_i = \frac{E_{el} 4\pi\epsilon_0 R_{ij}}{e^2 z_i} \quad (9-2)$$

where  $E_{el}$  is the electrostatic potential energy per atom from GULP,  $\epsilon_0$  is the permittivity of free space ( $8.8542 \times 10^{-12} \text{ C}^2 \text{ J}^{-1} \text{ m}^{-1}$ ),  $e$  is the charge of an electron ( $1.6022 \times 10^{-19} \text{ C}$ ),  $z_i$  is the cation charge, and  $R_{ij}$  is the nearest neighbor distance between cation and anion.

### **Development of Predictive Model**

Detailed information regarding the different materials informatics and data mining methods performed in this work were provided in detail in Chapter 2. The specific application of the various materials informatics methods presented in this section were carried out by Dr. Chang Sun Kong, a post-doctoral associate from Iowa State University.

### **Principal Component Analysis**

The first step in applying materials informatics to the tribological dataset given in Table 9-2 was to apply the principal component analysis (PCA) approach for dimensional reduction of the multivariate data, which identifies the major pattern of the complex data structure while maximizing the amount of variability contained within the dataset. From the PCA, we found that the first 3 PCs captured 34.9%, 30.9%, and 11.7% of the total variability, respectively, or 77.5% of the total variance within the original data matrix. Thus, by selecting only the first two PC axes, we were able to reflect more than 65% of the total information from the original data comprised of 15 variables.

The two primary results obtained from the PCA were the scores and loadings plots, which are illustrated in Figure 9-1. The scores plot shown in Figure 9-1A demonstrates the interrelationships between the samples within the dataset relative to the first and second PCs, which are identified as PC1 and PC2, respectively. The graph indicates that there was clearly discernible grouping based on material chemistry, distinguishing between the oxides, chalcogenides, and halides within the dataset. In particular, the halide materials were located in the first and second quadrants, while the materials in which the anionic elements belonged to the oxygen group in the periodic table (i.e. oxides and chalcogenides) were predominantly located in the third and fourth quadrants. This suggests that the main contribution of the PC2 dimension was for the separation based on the anionic elements, differentiating between the oxygen and halogen groups. It should further be noted that one data point, GaAs, which corresponds to the pnictide group, was located in the cluster of chalcogenides.

The loadings plot shown in Figure 9-1B indicates which material properties were influential and how the properties were interrelated within the plane of PC1 and PC2. As briefly mentioned in Chapter 2, each PC is a linear combination of the original variables (i.e. material properties) [90]; therefore, a variable having a high magnitude coefficient (PC loading) indicates that the variable has high dominance on the PC. Additionally, since a set of PC loading values is determined by the cosine angles between PCs and original variables, the positions of the vectors in Figure 9-1B relative to each other indicates the correlations between the variables. Specifically, the clustering of properties within the loadings plot shows that those properties are positively correlated. Similarly, when the properties in the graph are spatially similar yet separated by the origin, the

properties are inversely correlated. When two properties are highly correlated, it suggests that only one of the properties needs to be included in the analysis since both properties provide similar information [87]. From Figure 9-1B, we determined that some of the variables were highly correlated including, for example, cation charge and ionic potential, EN difference and percent ionicity, melting temperature and average hardness, molar weight and density, and cation radius and electrostatic potential. The inverse relationships were also apparent between cation radius, ionic potential and cation charge, between EN difference and density, and between  $R_{ij}$  distance and average hardness, among others. Based on these correlations, the loadings plot was used for the effective selection of model parameters while minimizing the redundant use of similar variables.

### **Analysis of Variable Importance**

In order to identify the most significant parameters (i.e. material properties) for developing the predictive model, two different analysis criteria, variable importance in projection (VIP) and error sum of squares (SS), were utilized to quantify the relative significance of each material property in the dataset given in Table 9-2. The results of these analyses are illustrated in Figure 9-2. For the VIP method, any given property with an importance value higher than unity was considered to be an important parameter for building the predictive model. Figure 9-2A shows that nine different properties (molar weight, EN difference, anion EN, cation EN, melting temperature, interplanar spacing, Madelung constant, percent ionicity, and Mohs hardness) were significant indicators of friction coefficient based on the VIP analysis. Alternatively, the SS analysis, which is shown in Figure 9-2B, indicated that seven properties (density, cation EN, melting temperature,  $R_{ij}$  distance, Madelung constant, cation radius, and cation charge) were

significant indicators of friction coefficient. Together, the VIP and SS methods overlapped in identifying three significant material properties (cation EN, melting temperature, and Madelung constant) which were used as the foundation on which to build our data-driven friction model.

### **Recursive Partitioning**

Friction coefficients, rather than being strict, finite values, are highly dependent upon testing parameters such as the details of the testing machine and environmental conditions. It is well-established that changes in these conditions can lead to significant variations in measured friction values [210]. Due to the inherent complexity of friction measurements, a traditional regression to formulate a predictive equation for friction coefficient is not likely to be an ideal solution; consequently, we have implemented the recursive partitioning method to develop our predictive friction model. Through recursive partitioning, the material dataset, which includes complex features such as nonlinear behaviors, is subdivided into smaller subsets in which the materials having the highest similarity within the parameter space are grouped together. Based on the results of the parameter space partitioning, a series of predictive if-then rules for the material properties are generated that provide a range of probable friction coefficients for the materials.

To develop our predictive model, we began with the three material properties identified to be most significant by the VIP and SS analyses; however, since three parameters is insufficient for generating a predictive model, we included additional parameters identified as important in Figure 9-2 in order to maximize the  $R^2$  value for the model. In particular, we found the best combination of material properties using the seven properties identified by the SS analysis shown in Figure 9-2B. The results for the

optimum predictive model are given in Figure 9-3 as a dendrogram of the if-then rules developed using these seven material properties.

A comparison between the experimental friction coefficients and the predicted values using this model is provided in Figure 9-4. The comparison indicated a high level of accuracy as evidenced by the  $R^2$  value of 0.8904; however, before we could truly attest to its accuracy, it was important to apply an appropriate means of validation. We accomplished this through a leave-one-out (LOO) cross-validation [215] of the friction model. In this approach, the dataset was divided into two subsets, referred to as the test data and training data; specifically, for the LOO cross-validation, the test data contained only one material from the dataset while the remaining materials made up the training data. From these subsets, different predictive models were generated with the test data always being removed for validation of the respective predictive models generated using the training data. From the LOO cross-validation, the  $R^2$  value decreased to 0.8193; the minor decrease of the predictability of the model demonstrated the robustness and accuracy of the model for estimating the friction coefficient of new materials. Thus, by using the data-driven approach described here, one can search new candidate materials with low friction coefficients in a high-throughput manner prior to exhaustive experimentation.

### **Discussion of Predictive Model**

The ability to predict friction coefficient in a robust and effective manner would accelerate the optimization of tribological design for mechanical systems. As such, this data-driven model allows for the rapid determination of the friction properties of ceramics by quickly filtering candidate materials on the basis of their intrinsic properties. It is well known that the frictional properties of most materials vary with conditions, such

as ambient air versus vacuum or dry environments [10, 18, 169, 210, 216] or room temperature versus cryogenic or high temperatures [10, 77, 146, 217]; this dependence on conditions was not accounted for here and is expected to influence the predictive ability of our model. Additional changes in the experimental tribological set-up such as rate of sliding and contact pressure, as well as variations in the counterface, could also lead to further discrepancies between a material's measured friction coefficient and the estimated value provided by our model. Nevertheless, this approach provides a means that is new to the tribological community for the high-throughput screening of candidate materials through identifying the key material properties and their combined influence on the macroscopic friction behavior of materials and linking them as an efficient materials design tool.

From the if-then rules for the friction model provided in Figure 9-3, it is clearly shown that density may be used as the first criterion to differentiate low and high friction coefficient materials, while the melting temperature and cation radius were also identified as important parameters. High friction coefficient materials are designated based primarily on density and the EN of the cation, but they are further separated through melting temperature,  $R_{ij}$  distance, and cation charge. It is particularly noteworthy that the if-then rules consist of four parameters: density ( $\geq 6.9$  or  $< 5.6$  g/cc), Madelung constant, melting temperature ( $< 1511$  K), and cation radius ( $< 0.76$  Å) for the screening of candidate ceramic materials with low friction coefficients ( $< \sim 0.25$ ). As such, this predictive model indicates that these four material properties should be checked first when designing new solid-state ceramic materials for low friction applications.

## Summary

Through the use of multivariate data mining algorithms, we have developed a predictive model for estimating the friction coefficient of a variety of classes of ceramic materials. We have demonstrated that fundamental descriptors of materials providing information varying from crystal structure to electronic structure have a significant influence on the ability to determine coefficient of friction in the class of materials included in this study. This data-driven model, which combines methods of data classification and dimensionality reduction to quantify the influence of a material's properties on its frictional performance, indicates the potential for additional studies in predictive modeling and the design of materials with desired tribological characteristics. The application of the new computational materials design platform presented here will enable not only the prediction of a material's friction coefficient but also the filtering of possible elemental combinations from the periodic table to predict the coefficient of friction for previously unknown compounds.

Table 9-1. List of 24 minerals and their forms used in tribometer experiments.

Sample set 1: Mineralogical samples	Sample set 2: Single crystal optical window samples	Sample set 3: Crystalline pieces ( $< 6$ mm)
Ag <sub>2</sub> S	SiO <sub>2</sub>	CdS
Cu <sub>2</sub> S	ZnS	NiS
FeS <sub>2</sub>	ZnSe	Sb <sub>2</sub> S <sub>3</sub>
PbS	BaF <sub>2</sub>	CoSe
MoS <sub>2</sub>	CaF <sub>2</sub>	PbSe
YPO <sub>4</sub>	CdTe	Cu <sub>2</sub> Se
	MgF <sub>2</sub>	NiTe
	NaCl	
	KCl	
	KBr	
	GaAs	

Table 9-2. Material dataset with 16 properties and 38 materials used to develop predictive model for friction coefficient.

Chemical formula	Structure/phase	Coefficient of friction <sup>a</sup>	Mohs hardness <sup>b</sup>	Formal cation charge	Cation radius (Å) <sup>c</sup>	Ionic potential	Percent ionicity (%)	Madelung constant	Electrostatic potential (eV/atom)
MgO	Periclase	0.425 [210]	5.50	2	0.72	2.778	67.833	-1.747	-23.904
SiO <sub>2</sub>	Quartz	0.449	7.00	4	0.40	10.000	44.728	-1.474	-52.773
Al <sub>2</sub> O <sub>3</sub>	Corundum	0.400 [210]	9.00	3	0.54	5.556	56.709	-1.216	-28.334
ZnO	Zincite	0.700 [210]	4.00	2	0.74	2.703	55.113	-1.642	-23.885
CuO	Tenorite	0.400 [218]	3.50 [219]	2	0.77	2.597	44.728	-1.365	-20.199
FeO	Wustite	0.600 [210]	5.00 [219]	2	0.55	3.636	47.692	-1.747	-23.350
MoO <sub>3</sub>	Molybdate	0.235 [210]	3.50 [220]	6	0.69	8.696	33.608	-1.392	-61.521
NiO	Bunsenite	0.500 [210]	5.50	2	0.69	2.899	44.302	-1.747	-24.150
V <sub>2</sub> O <sub>5</sub>	Shcherbinaite	0.310 [210]	3.25 [221]	5	0.79	6.329	55.914	-1.486	-58.475
TiO <sub>2</sub>	Rutile	0.450 [210]	6.20	4	0.86	4.651	59.445	-1.600	-47.076
SnO <sub>2</sub>	Cassiterite	0.500 [210]	6.50	4	0.69	5.797	42.166	-1.600	-44.890
ZrO <sub>2</sub>	Baddeleyite	0.500 [210]	6.50	4	0.72	5.556	67.144	-1.660	-43.753
Ag <sub>2</sub> S	Acanthite	0.101	2.30	1	1.15	0.870	10.024	-1.576	-8.921
WS <sub>2</sub>	Tungstenite	0.043 [222]	2.50 [223]	4	0.60	6.667	1.203	-1.283	-30.666
PbS	Galena	0.202	2.50	2	1.19	1.681	1.550	-1.747	-16.957
Cu <sub>2</sub> S	Chalcocite	0.315	2.80	1	0.77	1.299	10.917	-1.567	-9.791
MoS <sub>2</sub>	Molybdenite	0.220	1.30	4	0.69	5.797	4.314	-1.283	-30.486
FeS <sub>2</sub>	Pyrite	0.200	6.30	2	0.55	3.636	13.118	-0.791	-10.070
ZnS	Sphalerite	0.527	3.80	2	0.74	2.703	19.445	-1.637	-20.141

<sup>a</sup> All friction coefficients from tribometry experiments detailed previously unless otherwise stated

<sup>b</sup> All Mohs hardness values from CRC Handbook [224] unless otherwise stated

<sup>c</sup> All ionic radii from Gersten and Smith [225]

Table 9-2. Continued

Chemical formula	Structure/phase	Coefficient of friction <sup>a</sup>	Mohs hardness <sup>b</sup>	Formal cation charge	Cation radius (Å) <sup>c</sup>	Ionic potential	Percent ionicity (%)	Madelung constant	Electrostatic potential (eV/atom)
Sb <sub>2</sub> S <sub>3</sub>	Stibnite	0.300	2.00	3	0.76	3.947	6.782	-1.551	-25.842
CdS	Greenockite	0.370	3.30	2	0.95	2.105	17.965	-1.642	-18.681
NiS	Millerite	0.240	3.30	2	0.69	2.899	10.616	-1.626	-20.321
MoSe <sub>2</sub>	Drysdallite	0.060 [226]	2.00 [227]	4	0.69	5.797	3.731	-1.283	-29.257
ZnSe	Stilleite	0.490	5.00 [223]	2	0.74	2.703	18.331	-1.637	-19.222
GaSe	P6 <sub>3</sub> /mmc	0.230 [228]	2.00 [229]	2	0.62	3.226	12.794	-1.039	-12.054
CoSe	Freboldite	0.280	2.75 [230]	2	0.65	3.077	10.616	-1.706	-19.832
Cu <sub>2</sub> Se	Berzelianite	0.490	2.70 [223]	1	0.77	1.299	10.024	-1.554	-8.855
PbSe	Clausthalite	0.190	2.75 [223]	2	1.19	1.681	1.203	-1.747	-16.375
CdTe	Zinc Blende	0.718	3.00 [229]	2	0.95	2.105	4.115	-1.637	-16.810
NiTe	Imgreite	0.280	4.00 [231]	2	0.69	2.899	0.898	-1.706	-18.566
GaAs	Zinc Blende	0.405	4.50 [229]	3	0.62	4.839	3.365	-2.455	-43.357
CaF <sub>2</sub>	Fluorite	0.372	4.00	2	1.00	2.000	89.140	-0.839	-10.224
BaF <sub>2</sub>	Frankdicksonite	0.392	2.50 [219]	2	1.35	1.481	90.810	-0.839	-9.009
MgF <sub>2</sub>	Sellaite	0.429	5.00	2	0.72	2.778	83.174	-0.801	-11.583
NaCl	Halite	0.303	2.00	1	1.02	0.980	71.155	-0.873	-4.461
KCl	Sylvite	0.319	2.00	1	1.38	0.725	74.561	-0.873	-3.999
KBr	Rock Salt	0.379	1.50 [229]	1	1.38	0.725	68.174	-0.873	-3.813
YPO <sub>4</sub>	Xenotime	0.357	4.50	3 <sup>d</sup>	0.90 <sup>d</sup>	3.333 <sup>d</sup>	52.884	-2.804 <sup>d</sup>	-51.689

<sup>a</sup> All friction coefficients from tribometry experiments detailed previously unless otherwise stated

<sup>b</sup> All Mohs hardness values from CRC Handbook [224] unless otherwise stated

<sup>c</sup> All ionic radii from Gersten and Smith [225]

<sup>d</sup> Value specific to yttrium ion

Table 9-2. Continued

Chemical formula	Interplanar spacing (Å)	R <sub>ij</sub> distance (Å)	Melting temperature (K) <sup>e</sup>	EN of cation <sup>f</sup>	EN of anion <sup>f</sup>	EN difference <sup>f</sup>	Density (g/cc) <sup>e</sup>	Molar weight (g/mol) <sup>g</sup>
MgO	2.106	2.106	3098	1.31	3.44	2.13	3.600	40.304
SiO <sub>2</sub>	1.500	1.610	1995	1.90	3.44	1.54	2.648	60.084
Al <sub>2</sub> O <sub>3</sub>	1.327	1.855	2327	1.61	3.44	1.83	3.990	101.961
ZnO	1.796	1.981	2247	1.65	3.44	1.79	5.600	81.380
CuO	1.277	1.948	1500	1.90	3.44	1.54	6.310	79.545
FeO	2.155	2.155	1650	1.83	3.44	1.61	6.000	71.844
MoO <sub>3</sub>	2.102	1.956	1075	2.16	3.44	1.28	4.700	143.960
NiO	2.084	2.084	2230	1.91	3.44	1.53	6.720	74.693
V <sub>2</sub> O <sub>5</sub>	2.303	1.831	954	1.63	3.44	1.81	3.350	181.880
TiO <sub>2</sub>	1.983	1.958	2116	1.54	3.44	1.90	4.170	79.866
SnO <sub>2</sub>	2.057	2.054	1903	1.96	3.44	1.48	6.850	150.709
ZrO <sub>2</sub>	1.290	2.187	2983	1.33	3.44	2.11	5.680	123.223
Ag <sub>2</sub> S	2.072	2.546	1098	1.93	2.58	0.65	7.230	247.801
WS <sub>2</sub>	3.124	2.411	1523	2.36	2.58	0.22	7.600	247.970
PbS	2.968	2.968	1386	2.33	2.58	0.25	7.600	239.300
Cu <sub>2</sub> S	1.427	2.306	1402	1.90	2.58	0.68	5.600	159.157
MoS <sub>2</sub>	2.980	2.425	1458 [232]	2.16	2.58	0.42	5.060	160.090
FeS <sub>2</sub>	1.464	2.264	1444 [232]	1.83	2.58	0.75	5.020	119.975
ZnS	1.913	2.342	1973	1.65	2.58	0.93	4.040	97.440

<sup>e</sup> All melting temperature and density values from CRC Handbook [233] unless otherwise stated

<sup>f</sup> Electronegativity values on the Pauling scale

<sup>g</sup> Molar weights according to the National Institute of Standards and Technology

Table 9-2. Continued

Chemical formula	Interplanar spacing (Å)	R <sub>ij</sub> distance (Å)	Melting temperature (K) <sup>e</sup>	EN of cation <sup>f</sup>	EN of anion <sup>f</sup>	EN difference <sup>f</sup>	Density (g/cc) <sup>e</sup>	Molar weight (g/mol) <sup>g</sup>
Sb <sub>2</sub> S <sub>3</sub>	1.915	2.594	823	2.05	2.58	0.53	4.562	339.715
CdS	2.599	2.532	1753	1.69	2.58	0.89	4.826	144.476
NiS	1.635	2.306	1249	1.91	2.58	0.67	5.500	90.758
MoSe <sub>2</sub>	3.118	2.527	1473	2.16	2.55	0.39	6.900	253.880
ZnSe	2.004	2.454	1790 [234]	1.65	2.55	0.90	5.650	144.340
GaSe	3.184	2.484	1233	1.81	2.55	0.74	5.030	148.680
CoSe	1.325	2.479	1328	1.88	2.55	0.67	7.650	137.890
Cu <sub>2</sub> Se	1.460	2.529	1386	1.90	2.55	0.65	6.840	206.050
PbSe	3.074	3.074	1351	2.33	2.55	0.22	8.100	286.200
CdTe	2.291	2.806	1365 [234]	1.69	2.10	0.41	6.200	240.010
NiTe	1.339	2.648	1133 [235]	1.91	2.10	0.19	8.384 [236]	186.293
GaAs	1.999	2.448	1511	1.81	2.18	0.37	5.318	144.645
CaF <sub>2</sub>	1.366	2.366	1691	1.00	3.98	2.98	3.180	78.075
BaF <sub>2</sub>	1.550	2.685	1641	0.89	3.98	3.09	4.893	175.324
MgF <sub>2</sub>	1.981	1.992	1536	1.31	3.98	2.67	3.148	62.302
NaCl	2.820	2.820	1073.7	0.93	3.16	2.23	2.170	58.443
KCl	3.146	3.146	1044	0.82	3.16	2.34	1.988	74.551
KBr	3.300	3.300	1007	0.82	2.96	2.14	2.740	119.002
YPO <sub>4</sub>	2.243	2.345 <sup>d</sup>	2268 [237]	1.71	3.44	1.74	4.800 [224]	183.877

<sup>d</sup> Value specific to yttrium ion

<sup>e</sup> All melting temperature and density values from CRC Handbook [233] unless otherwise stated

<sup>f</sup> Electronegativity values on the Pauling scale

<sup>g</sup> Molar weights according to the National Institute of Standards and Technology

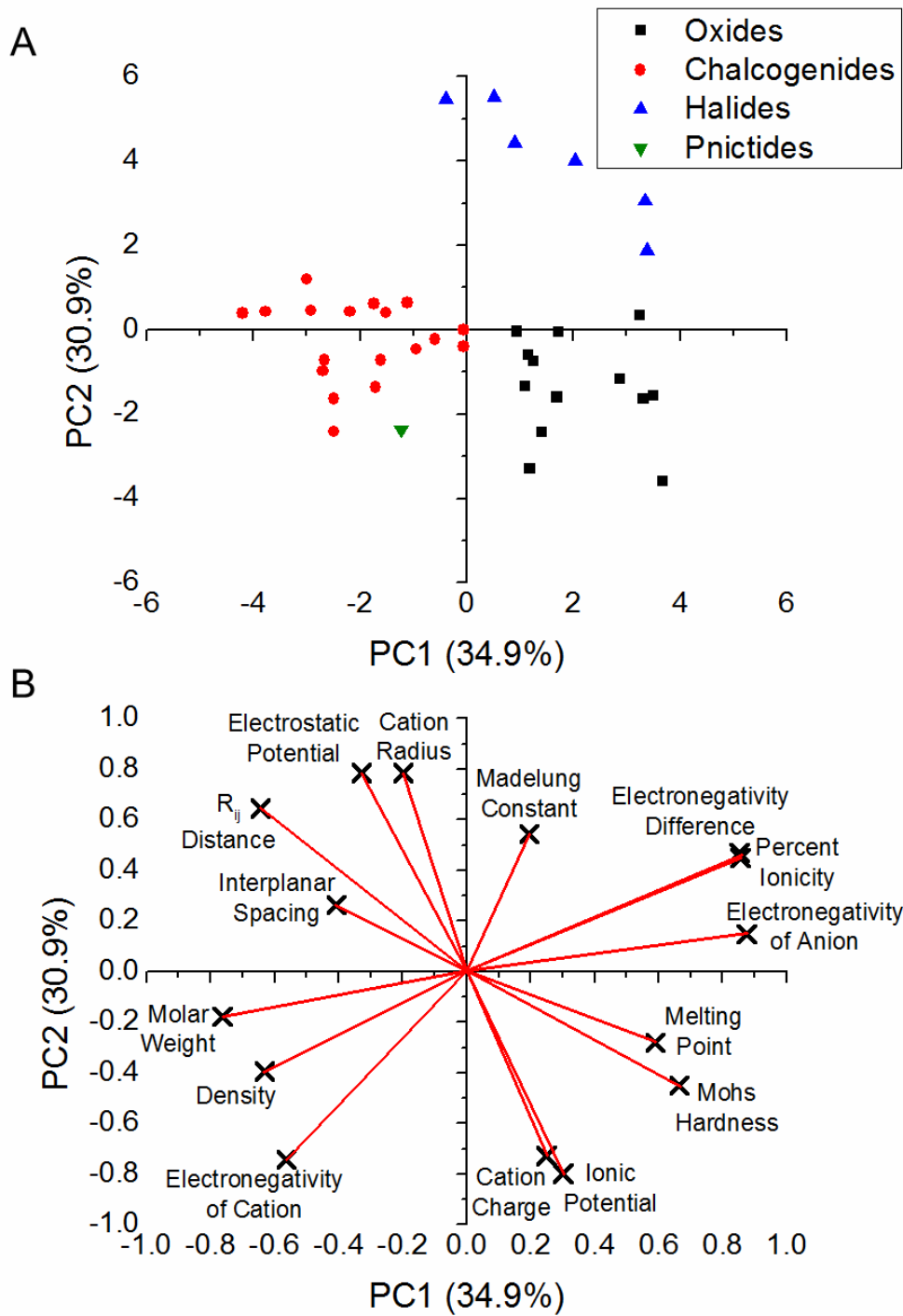


Figure 9-1. Principal component analysis A) scores plot and B) loadings plot for PC1 versus PC2.

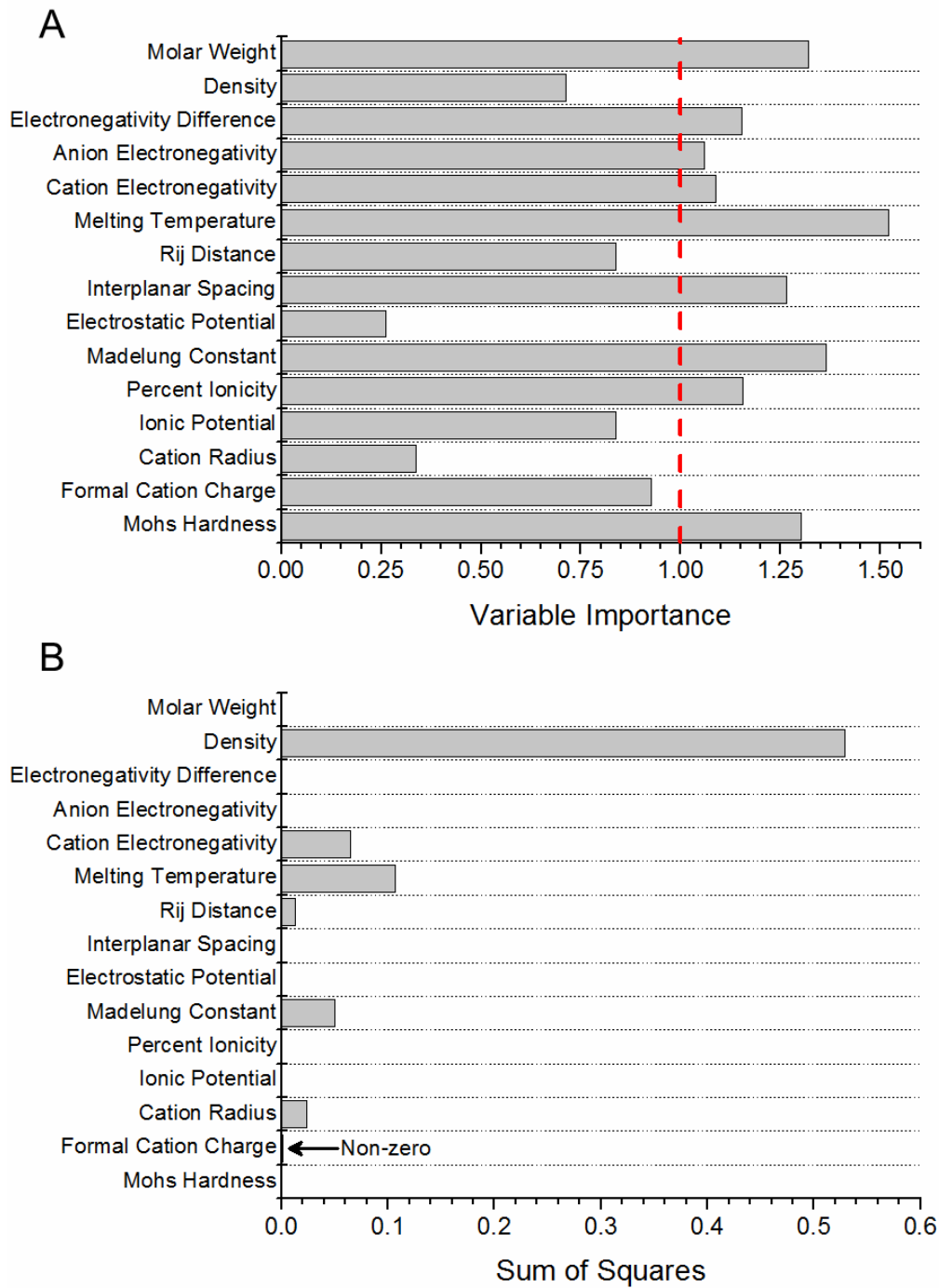


Figure 9-2. Analysis of variable significance indicating methods of A) variable importance and B) sum of squares that were used to determine parameters to include in recursive partitioning.

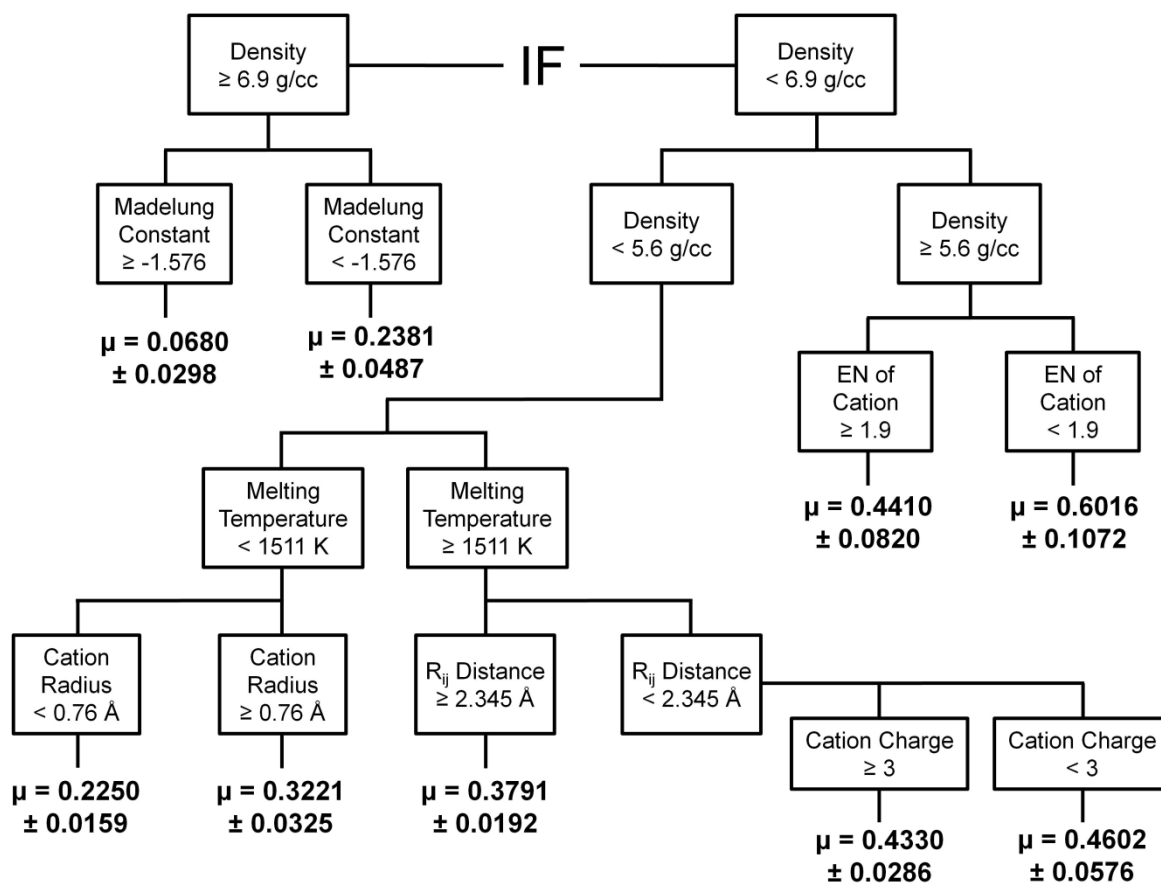


Figure 9-3. Dendrogram for estimation of friction coefficient from recursive partitioning.

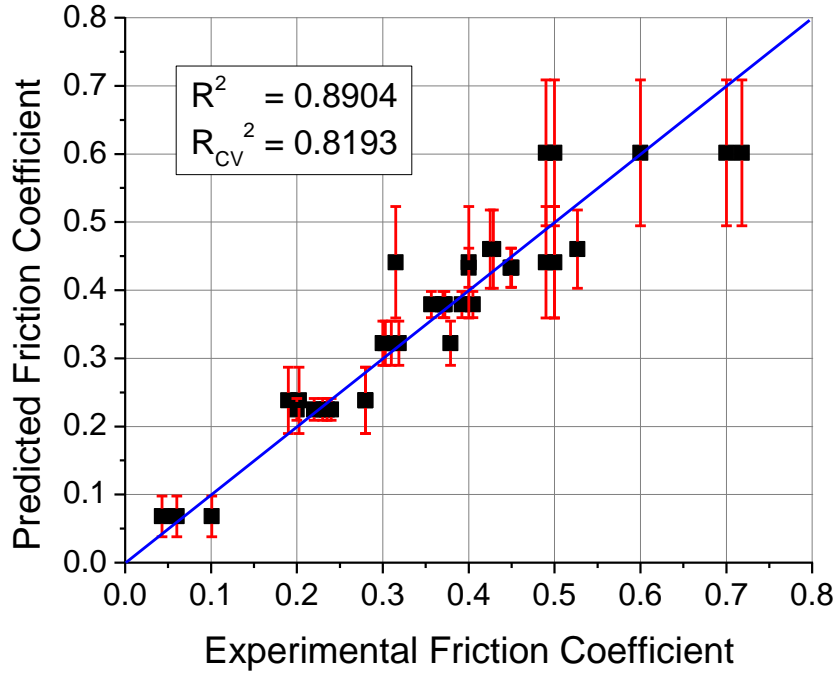


Figure 9-4. Predicted versus experimental friction coefficient from recursive partitioning. Error bars represent the standard deviation relative to each branch of the dendrogram.

## CHAPTER 10 GENERAL CONCLUSIONS

A combination of computational and experimental methods, specifically classical MD simulations, AFM experiments, and multivariate statistical analyses, were used in the studies reported in this dissertation to provide fundamental insight into the tribological and mechanical properties of a variety of materials including carbon-based and inorganic nanostructures, lamellar materials, and inorganic ceramic compounds. By using the combined approach of each of these computational and experimental techniques, the key mechanisms involved in the friction and mechanics of these different materials were reported.

Atomistic MD simulations of carbon nano-onions, both with and without a residual diamond core, sliding between DLC surfaces established that the lubrication mechanism of these nanoparticles does not involve the exfoliation of graphene sheets as was originally hypothesized. Rather, the simulations demonstrated the ability of the COs to roll within the tribological interface and identified the conditions during which rolling, which provides optimal friction performance, was found to be possible. The results quantified the influence of rolling and/or sliding on the tribological properties of COs and D-COs and showed that the relative proportion of rolling/sliding behavior was determined by strong interfacial bond formations during friction. In particular, the COs displayed a load dependent friction behavior transitioning from rolling to sliding above an apparent contact pressure of  $\sim 2.5$  GPa; the D-COs, on the other hand, displayed a prevalence for sliding at all contact pressures resulting from the presence of the residual diamond core. The observed transition from rolling to sliding of the COs was also accompanied by an increase in coefficient of friction from  $\sim 0.029$  to  $0.151$ .

Classical MD simulations investigating the mechanical and tribological properties of a-C nanoparticles were motivated by qualitative *in situ* HRTEM experiments involving the nanocompression of individual a-C nanoparticles. The simulations agreed well with the experimental observations indicating that the a-C nanoparticles deformed during compressive loading via an elastic/plastic process. The results of the nanocompression simulations indicated that changes in nanoparticle diameter from 2-5 nm and/or hydrogen content from 0-50 at.% H had no discernible effect on the mechanical response of the nanoparticles; it was further identified that the transition from elastic to plastic behavior was induced by the formation of new C-C bonds, which increased the cross-linking of the internal network. The MD friction simulations indicated that the a-C nanoparticles exhibited both diameter and at.% H dependent tribological properties, which was affected by the formation of strong interfacial bonds during friction. Increased hydrogenation passivated the unsaturated sp- and sp<sup>2</sup>-hybridized carbon atoms at the surface, which limited interfacial bonds and reduced friction. Also, the 4 nm diameter nanoparticle systems had higher friction coefficients than the 2 nm diameter systems resulting from the larger surface area causing more initiation points for interfacial bonds. The results indicated that a-C nanoparticles, which are able to provide low coefficients of friction, require a high degree of surface passivation in order to obtain optimal tribological properties since friction increases with the formation of interfacial bonds.

MD simulations of the compression and friction of IF-MoS<sub>2</sub> nanoparticles indicated that these nanoparticles exhibit both structure and orientation dependent tribological and mechanical properties. The nanocompression simulations demonstrated that IF-MoS<sub>2</sub> nanoparticles exhibit preferential exfoliation at defect locations such as grain

boundaries since the nano-octahedron exhibited exfoliation at the facet edges while no localized failure was observed for the ellipsoidal nanoparticle oriented along its minor axis. The tribological simulations demonstrated that the friction coefficient for the IF-MoS<sub>2</sub> nanoparticles varied up to a factor of 4 for the three systems considered ranging from 0.004 for the ellipsoidal nanoparticle oriented along its minor axis to 0.016 for the ellipsoidal nanoparticle on its major axis. These simulations further indicated that the circular orientation of the ellipsoidal nanoparticle positioned on its major axis provided the ability to roll within the interface; this rolling mechanism was found to be load dependent and was observed below a contact pressure of ~380 MPa. The IF-MoS<sub>2</sub> simulations reported here elucidate the relative influence of nanoparticle structure and orientation on the observed lubrication mechanisms of these nanoparticles.

Classical MD simulations of lamellar MoS<sub>2</sub> systems both with and without exposed edges were performed to investigate experimental observations of temperature dependent and independent tribological properties of MoS<sub>2</sub> systems at cryogenic temperatures [146]. Contrary to the experimental findings, these tribological simulations predicted that very low friction forces were maintained throughout the simulations at the range of temperatures considered from 5 to 500 K; therefore, the simulations did not indicate any temperature dependent tribological properties. Also, opposing the initial hypothesis, no evidence of interfacial wearing induced by the presence of high energy MoS<sub>2</sub> edges was observed. Future MD simulations which address system changes, such as alternative sliding counterfaces, may be able to explain the experimental observations of temperature dependent tribological behavior during friction of lamellar MoS<sub>2</sub> systems at cryogenic temperatures.

The mechanical behavior of MoS<sub>2</sub> nanotubes being subjected to compressive, tensile, and torsional loading was reported, for the first time, using classical MD simulations, which predicted values for Young's modulus and torsional shear modulus that were in good agreement with previous studies using different methods [155, 157]. The simulations predicted little to no dependence of the elastic properties on length and diameter for the SWINTs and DWINTs considered here having 10 to 30 nm lengths and 5 to 10 nm diameters. During compressive loading, the critical buckling stress of the INTs was found to scale inversely with increasing diameter; however, above a length of at least 20 nm, no discernible impact of INT length on critical buckling stress was observed. During torsional loading, the torsional stiffness of the INTs was shown to scale with diameter approximately as  $K \propto D^{3.1}$  for the armchair INTs and as  $K \propto D^{3.06}$  for the zigzag INTs, which is in good agreement with previous findings for carbon nanotubes [56, 147]. In addition, the results indicated that the critical buckling moments were significantly impacted by changes in the structural properties of the INTs including nanotube length, diameter, and number of MoS<sub>2</sub> walls. For the DWINTs, it was further shown that the application of torsion to both walls resulted in a 41% decrease in critical buckling angle relative to torsion applied only to the outer wall. The results reported here provide detailed information about the mechanical responses of MoS<sub>2</sub> INTs over a range of lengths and diameters when subjected to varying loading conditions.

The AFM friction experiments of mineralogical pyrophyllite samples demonstrated the atomic-scale tribological properties of the cleaved mineral; pyrophyllite was deemed a candidate for solid lubrication based on its promising structural properties, which feature a low energy basal plane predominantly characterized by weak vdW interactions

suggesting the opportunity for low energy interfacial interactions. The AFM experiments indicated that, in the absence of wear, pyrophyllite exhibits a coefficient of friction of  $\sim 0.03$  and a shear strength of 39 MPa when in contact with a  $\text{Si}_3\text{N}_4$  probe tip which is comparable with other materials employed as solid lubricants [192-196]. The experiments further indicated an atomic-scale threshold to wear of  $\sim 1.6$  GPa; this finding is in excess of the yield strength of many minerals [200], which is consistent with the nature of atomic bonding within silicate layers and the energetics of macroscopic material deformation. The findings from these AFM experiments suggest that pyrophyllite shows promise for use as a tribological material in systems where conditions do not necessitate the pyrophyllite to bear the full load support of the moving contacts.

Using multivariate data mining algorithms, we developed a predictive model for estimating the friction coefficient of a variety of classes of ceramic materials. Fundamental descriptors of materials providing varying information were shown to have a significant influence on the ability to predict the coefficient of friction for the class of materials considered here. By combining methods of data classification and dimensionality reduction to quantify the relative influence of a material's properties on its friction performance, this data-driven model demonstrates the potential for additional studies in predictive modeling and the design of materials with specific tribological characteristics. Beyond the ability to estimate the friction coefficient for known materials, the future application of the new computational materials design platform reported in this work will provide the ability to filter possible elemental combinations from the

periodic table in order to predict the coefficient of friction for previously unknown compounds.

Overall, the computational and experimental studies discussed in this dissertation reported fundamental contributions to the investigation of the tribological and mechanical properties of many materials. In friction and nanomechanics, it is necessary to develop a thorough understanding of the mechanisms involved during specific processes in order to optimize the desired performance. As such, in the field of tribology, the lubrication mechanisms of nanoparticles are widely investigated [39, 46, 103, 139], but achieving atomic-level information and *in situ* observation of sliding interfaces is a continual experimental challenge. Motivated by experimental findings, the classical MD simulations of COs, a-C nanoparticles, and IF-MoS<sub>2</sub> nanoparticles reported here identified the specific mechanisms that occur when these nanoparticles are subjected to compressive and frictional forces within a tribological contact and quantified the relative influence of these atomistic mechanisms on the observed frictional performance. For the nanomechanical manipulation of nanotubes, experimental methods, such as AFM and electron microscopy, are frequently used to investigate the elastic properties and buckling behavior of the nanotubes [147, 149, 153, 155]; however, classical MD simulations provide the opportunity to control the specific structural parameters of nanotubes, such as length, diameter, and number of walls, in order to identify the relationships between structural changes and mechanical response, which was demonstrated for MoS<sub>2</sub> nanotubes for the first time in the work presented here.

Experimentally, pyrophyllite belongs to the phyllosilicate class of minerals, which are materials of geological significance in fault zones [169, 172, 173, 175]. In this dissertation, AFM friction experiments on cleaved pyrophyllite samples confirmed the hypothesis that, at the atomic-scale, pyrophyllite provides a low coefficient of friction and low shear stresses as well as a high threshold to interfacial wear, which suggests the potential for implementing pyrophyllite as a lubricious material in tribological systems. Finally, the use of multivariate statistical analyses demonstrated the ability to utilize fundamental material properties in order to quickly and accurately estimate the friction coefficients of inorganic ceramic compounds; these findings provide the tribological community with a new, efficient, and high-throughput means of identifying candidate materials that may provide desired frictional performance.

## LIST OF REFERENCES

1. Bhushan, B.: Principles and Applications of Tribology. John Wiley & Sons, Inc., New York (1999)
2. Miyoshi, K.: Solid Lubrication Fundamentals and Applications. Marcel Dekker, Inc., New York (2001)
3. Jost, H.P.: Tribology: How a word was coined 40 years ago. Tribol. Lubr. Technol. **62**, 24-28 (2006)
4. Jost, H.P.: Lubrication (Tribology) Education and Research - A Report on the Present Position and Industry's Needs. Her Majesty's Stationery Office, London (1966)
5. Rabinowicz, E.: Friction and Wear of Materials, 2nd edn. John Wiley & Sons, Inc., New York (1995)
6. Jost, H.P.: Tribology - Origin and future. Wear **136**, 1-17 (1990)
7. Ku, P.M.: Energy and materials conservation through tribology. Lubr. Eng. **34**, 131-134 (1978)
8. Pinkus, O., Wilcock, D.F.: Strategy for Energy Conservation Through Tribology. American Society of Mechanical Engineers, New York (1977)
9. Hilton, M.R., Fleischauer, P.D.: Applications of solid lubricant films in spacecraft. Surf. Coat. Technol. **55**, 435-441 (1992)
10. Miyoshi, K.: Solid lubricants and coatings for extreme environments: State-of-the-art survey. Tech. Memo. NASA/TM, 214668 (2007)
11. Dienwiebel, M., Verhoeven, G.S., Pradeep, N., Frenken, J.W.M., Heimberg, J.A., Zandbergen, H.W.: Superlubricity of graphite. Phys. Rev. Lett. **92**, 126101 (2004)
12. Donnet, C., Martin, J.M., LeMogne, T., Belin, M.: Super-low friction of MoS<sub>2</sub> coatings in various environments. Tribol. Int. **29**, 123-128 (1996)
13. Fleischauer, P.D.: Fundamental aspects of the electronic structure, materials properties and lubrication performance of sputtered MoS<sub>2</sub> films. Thin Solid Films **154**, 309-322 (1987)
14. Lieber, C.M., Kim, Y.: Characterization of the structural, electronic and tribological properties of metal dichalcogenides by scanning probe microscopies. Thin Solid Films **206**, 355-359 (1991)

15. Pawlak, Z., Pai, R., Bayraktar, E., Kaldonski, T., Oloyede, A.: Lamellar lubrication in vivo and vitro: Friction testing of hexagonal boron nitride. *Biosyst.* **94**, 202-208 (2008)
16. Hirano, M.: Atomistics of friction. *Surf. Sci. Rep.* **60**, 159-201 (2006)
17. Lancaster, J.K.: A review of the influence of environmental humidity and water on friction, lubrication, and wear. *Tribol. Int.* **23**, 371-389 (1990)
18. Ohmae, N.: Humidity effects on tribology of advanced carbon materials. *Tribol. Int.* **39**, 1497-1502 (2006)
19. Vanhulsel, A., Velasco, F., Jacobs, R., Eersels, L., Havermans, D., Roberts, E.W., Sherrington, I., Anderson, M.J., Gaillard, L.: DLC solid lubricant coatings on ball bearings for space applications. *Tribol. Int.* **40**, 1186-1194 (2007)
20. Robertson, J.: Properties of diamond-like carbon. *Surf. Coat. Technol.* **50**, 185-203 (1992)
21. Erdemir, A.: The role of hydrogen in tribological properties of diamond-like carbon films. *Surf. Coat. Technol.* **146**, 292-297 (2001)
22. Schall, J.D., Gao, G.T., Harrison, J.A.: Effects of adhesion and transfer film formation on the tribology of self-mated DLC contacts. *J. Phys. Chem. C* **114**, 5321-5330 (2010)
23. Chhowalla, M., Amaratunga, G.A.J.: Thin films of fullerene-like MoS<sub>2</sub> nanoparticles with ultra-low friction and wear. *Nature* **407**, 164-167 (2000)
24. Ugarte, D.: Curling and closure of graphitic networks under electron-beam irradiation. *Nature* **359**, 707-709 (1992)
25. Rapoport, L., Bilik, Y., Feldman, Y., Homyonfer, M., Cohen, S.R., Tenne, R.: Hollow nanoparticles of WS<sub>2</sub> as potential solid-state lubricants. *Nature* **387**, 791-793 (1997)
26. Bhushan, B., Gupta, B.K., Vancleef, G.W., Capp, C., Coe, J.V.: Fullerene (C<sub>60</sub>) films for solid lubrication. *Tribol. Trans.* **36**, 573-580 (1993)
27. Buldum, A., Lu, J.P.: Atomic scale sliding and rolling of carbon nanotubes. *Phys. Rev. Lett.* **83**, 5050-5053 (1999)
28. Rapoport, L., Nepomnyashchy, O., Lapsker, I., Verdyan, A., Soifer, Y., Popovitz-Biro, R., Tenne, R.: Friction and wear of fullerene-like WS<sub>2</sub> under severe contact conditions: Friction of ceramic materials. *Tribol. Lett.* **19**, 143-149 (2005)
29. Fusaro, R.L.: Self-lubricating polymer composites and polymer transfer film lubrication for space applications. *Tribol. Int.* **23**, 105-122 (1990)

30. Khedkar, J., Negulescu, I., Meletis, E.I.: Sliding wear behavior of PTFE composites. *Wear* **252**, 361-369 (2002)
31. Sawyer, W.G., Freudenberg, K.D., Bhimaraj, P., Schadler, L.S.: A study on the friction and wear behavior of PTFE filled with alumina nanoparticles. *Wear* **254**, 573-580 (2003)
32. Fischer, T.E., Mullins, W.M.: Chemical aspects of ceramic tribology. *J. Phys. Chem.* **96**, 5690-5701 (1992)
33. Hsu, S.M.: Boundary lubrication: Current understanding. *Tribol. Lett.* **3**, 1-11 (1997)
34. Grossiord, C., Varlot, K., Martin, J.M., Le Mogne, T., Esnouf, C., Inoue, K.: MoS<sub>2</sub> single sheet lubrication by molybdenum dithiocarbamate. *Tribol. Int.* **31**, 737-743 (1998)
35. Cizaire, L., Vacher, B., Le Mogne, T., Martin, J.M., Rapoport, L., Margolin, A., Tenne, R.: Mechanisms of ultra-low friction by hollow inorganic fullerene-like MoS<sub>2</sub> nanoparticles. *Surf. Coat. Technol.* **160**, 282-287 (2002)
36. Rapoport, L., Leshchinsky, V., Lapsker, I., Volovik, Y., Nepomnyashchy, O., Lvovsky, M., Popovitz-Biro, R., Feldman, Y., Tenne, R.: Tribological properties of WS<sub>2</sub> nanoparticles under mixed lubrication. *Wear* **255**, 785-793 (2003)
37. Peng, Y.T., Hu, Y.Z., Wang, H.: Tribological behaviors of surfactant-functionalized carbon nanotubes as lubricant additive in water. *Tribol. Lett.* **25**, 247-253 (2007)
38. Matsumoto, N., Joly-Pottuz, L., Kinoshita, H., Ohmae, N.: Application of onion-like carbon to micro and nanotribology. *Diam. Relat. Mater.* **16**, 1227-1230 (2007)
39. Joly-Pottuz, L., Martin, J.M., Belin, M., Dassenoy, F., Montagnac, G., Reynard, B.: Study of inorganic fullerenes and carbon nanotubes by in situ Raman tribometry. *Appl. Phys. Lett.* **91**, 153107 (2007)
40. Joly-Pottuz, L., Dassenoy, F., Vacher, B., Martin, J.M., Mieno, T.: Ultralow friction and wear behaviour of Ni/Y-based single wall carbon nanotubes (SWNTs). *Tribol. Int.* **37**, 1013-1018 (2004)
41. Joly-Pottuz, L., Martin, J.M., Dassenoy, F., Belin, M., Montagnac, G., Reynard, B., Fleischer, N.: Pressure-induced exfoliation of inorganic fullerene-like WS<sub>2</sub> particles in a Hertzian contact. *J. Appl. Phys.* **99**, 023524 (2006)
42. Sawyer, W.G., Perry, S.S., Phillpot, S.R., Sinnott, S.B.: Integrating experimental and simulation length and time scales in mechanistic studies of friction. *J. Phys.: Condens. Matter* **20**, 354012 (2008)

43. Binnig, G., Quate, C.F., Gerber, C.: Atomic force microscope. *Phys. Rev. Lett.* **56**, 930-933 (1986)
44. Szlufarska, I., Chandross, M., Carpick, R.W.: Recent advances in single-asperity nanotribology. *J. Phys. D: Appl. Phys.* **41**, 123001 (2008)
45. Beaber, A.R., Nowak, J.D., Ugurlu, O., Mook, W.M., Girshick, S.L., Ballarini, R., Gerberich, W.W.: Smaller is tougher. *Phil. Mag.* **91**, 1179-1189 (2011)
46. Lahouij, I., Dassenoy, F., Vacher, B., Martin, J.M.: Real time TEM imaging of compression and shear of single fullerene-like MoS<sub>2</sub> nanoparticle. *Tribol. Lett.* **45**, 131-141 (2012)
47. Shan, Z.W., Adesso, G., Cabot, A., Sherburne, M.P., Asif, S.A.S., Warren, O.L., Chrzan, D.C., Minor, A.M., Alivisatos, A.P.: Ultrahigh stress and strain in hierarchically structured hollow nanoparticles. *Nat. Mater.* **7**, 947-952 (2008)
48. Tevet, O., Goldbart, O., Cohen, S.R., Rosentsveig, R., Popovitz-Biro, R., Wagner, H.D., Tenne, R.: Nanocompression of individual multilayered polyhedral nanoparticles. *Nanotechnol.* **21**, 365705 (2010)
49. Frankland, S.J.V., Harik, V.M.: Analysis of carbon nanotube pull-out from a polymer matrix. *Surf. Sci.* **525**, L103-L108 (2003)
50. Tangney, P., Louie, S.G., Cohen, M.L.: Dynamic sliding friction between concentric carbon nanotubes. *Phys. Rev. Lett.* **93**, 065503 (2004)
51. Bao, W.X., Zhu, C.C., Cui, W.Z.: Simulation of Young's modulus of single-walled carbon nanotubes by molecular dynamics. *Physica B* **352**, 156-163 (2004)
52. Chen, M.J., Liang, Y.C., Li, H.Z., Li, D.: Molecular dynamics simulation on mechanical property of carbon nanotube torsional deformation. *Chin. Phys.* **15**, 2676-2681 (2006)
53. Xiao, S.P., Hou, W.Y.: Studies of size effects on carbon nanotubes' mechanical properties by using different potential functions. *Fuller. Nanotub. Carbon Nanostruct.* **14**, 9-16 (2006)
54. Heo, S., Sinnott, S.B.: Effect of molecular interactions on carbon nanotube friction. *J. Appl. Phys.* **102**, 064307 (2007)
55. Jeong, B.W., Lim, J.K., Sinnott, S.B.: Tensile mechanical behavior of hollow and filled carbon nanotubes under tension or combined tension-torsion. *Appl. Phys. Lett.* **90**, 023102 (2007)
56. Jeong, B.W., Lim, J.K., Sinnott, S.B.: Elastic torsional responses of carbon nanotube systems. *J. Appl. Phys.* **101**, 084309 (2007)

57. Li, X.Y., Yang, W.: Simulating fullerene ball bearings of ultra-low friction. *Nanotechnol.* **18**, 115718 (2007)
58. Harrison, J.A., Schall, J.D., Knippenberg, M.T., Gao, G.T., Mikulski, P.T.: Elucidating atomic-scale friction using molecular dynamics and specialized analysis techniques. *J. Phys.: Condens. Matter* **20**, 354009 (2008)
59. Heo, S.J., Jang, I., Barry, P.R., Phillpot, S.R., Perry, S.S., Sawyer, W.G., Sinnott, S.B.: Effect of the sliding orientation on the tribological properties of polyethylene in molecular dynamics simulations. *J. Appl. Phys.* **103**, 083502 (2008)
60. Barry, P.R., Chiu, P.Y., Perry, S.S., Sawyer, W.G., Phillpot, S.R., Sinnott, S.B.: The effect of normal load on polytetrafluoroethylene tribology. *J. Phys.: Condens. Matter* **21**, 144201 (2009)
61. Heo, S., Sinnott, S.B.: Computational investigation of the mechanical properties of nanomaterials. *Diam. Relat. Mater.* **18**, 438-442 (2009)
62. Jeong, B.W., Sinnott, S.B.: A torsional parametric oscillator based on carbon nanotubes. *Appl. Phys. Lett.* **95**, 083112 (2009)
63. Mylvaganam, K., Zhang, L.C., Xiao, K.Q.: Origin of friction in films of horizontally oriented carbon nanotubes sliding against diamond. *Carbon* **47**, 1693-1700 (2009)
64. Khomenko, A.V., Prodanov, N.V.: Molecular dynamics of cleavage and flake formation during the interaction of a graphite surface with a rigid nanoasperity. *Carbon* **48**, 1234-1243 (2010)
65. Pastewka, L., Moser, S., Moseler, M.: Atomistic insights into the running-in, lubrication, and failure of hydrogenated diamond-like carbon coatings. *Tribol. Lett.* **39**, 49-61 (2010)
66. Brenner, D.W., Shenderova, O.A., Harrison, J.A., Stuart, S.J., Ni, B., Sinnott, S.B.: A second-generation reactive empirical bond order (REBO) potential energy expression for hydrocarbons. *J. Phys.: Condens. Matter* **14**, 783-802 (2002)
67. Tersoff, J.: New empirical model for the structural properties of silicon. *Phys. Rev. Lett.* **56**, 632-635 (1986)
68. Tersoff, J.: New empirical approach for the structure and energy of covalent systems. *Phys. Rev. B* **37**, 6991-7000 (1988)
69. Brenner, D.W.: Empirical potential for hydrocarbons for use in simulating the chemical vapor deposition of diamond films. *Phys. Rev. B* **42**, 9458-9471 (1990)
70. Liang, T., Phillpot, S.R., Sinnott, S.B.: Parametrization of a reactive many-body potential for Mo-S systems. *Phys. Rev. B* **79**, 245110 (2009)

71. Allen, M.P., Tildesley, D.J.: Computer Simulation of Liquids. Oxford University Press, New York (1987)
72. Adelman, S.A., Doll, J.D.: Generalized Langevin equation approach for atom/solid-surface scattering: General formulation for classical scattering off harmonic solids. *J. Chem. Phys.* **64**, 2375-2388 (1976)
73. Jang, I., Burris, D.L., Dickrell, P.L., Barry, P.R., Santos, C., Perry, S.S., Phillpot, S.R., Sinnott, S.B., Sawyer, W.G.: Sliding orientation effects on the tribological properties of polytetrafluoroethylene. *J. Appl. Phys.* **102**, 123509 (2007)
74. Gao, G.T., Mikulski, P.T., Harrison, J.A.: Molecular-scale tribology of amorphous carbon coatings: Effects of film thickness, adhesion, and long-range interactions. *J. Am. Chem. Soc.* **124**, 7202-7209 (2002)
75. Chen, Z., Laboriante, I.C., Perry, S.S.: Compositional dependence of the microscopic frictional properties of single crystal metal carbides. *Tribol. Lett.* **23**, 209-214 (2006)
76. Tordjeman, P., Morel, N., Ramonda, M.: Tribological properties of silicate materials on nano and microscale. *Appl. Surf. Sci.* **255**, 6999-7004 (2009)
77. Zhao, X.Y., Perry, S.S.: Temperature-dependent atomic scale friction and wear on PbS(100). *Tribol. Lett.* **39**, 169-175 (2010)
78. Talylor, J.R.: An Introduction to Error Analysis: The Study of Uncertainties in Physical Measurements, 2nd edn. University Science Books, Sausalito (1997)
79. Hu, J., Xiao, X.D., Ogletree, D.F., Salmeron, M.: Atomic scale friction and wear of mica. *Surf. Sci.* **327**, 358-370 (1995)
80. Liu, E., Blanpain, B., Celis, J.P., Roos, J.R.: Comparative study between macrotribology and nanotribology. *J. Appl. Phys.* **84**, 4859-4865 (1998)
81. Butt, H.J., Jaschke, M.: Calculation of thermal noise in atomic force microscopy. *Nanotechnol.* **6**, 1-7 (1995)
82. Levy, R., Maaloum, M.: Measuring the spring constant of atomic force microscope cantilevers: Thermal fluctuations and other methods. *Nanotechnol.* **13**, 33-37 (2002)
83. Ogletree, D.F., Carpick, R.W., Salmeron, M.: Calibration of frictional forces in atomic force microscopy. *Rev. Sci. Instrum.* **67**, 3298-3306 (1996)
84. Carpick, R.W., Agrait, N., Ogletree, D.F., Salmeron, M.: Measurement of interfacial shear (friction) with an ultrahigh vacuum atomic force microscope. *J. Vac. Sci. Technol. B* **14**, 1289-1295 (1996)

85. Ferris, K.F., Peurrung, L.M., Marder, J.: Materials informatics: Fast track to new materials. *Adv. Mater. Process.* **165**, 50-51 (2007)
86. Gang, Y., Jingzhong, C., Li, Z.: Data mining techniques for materials informatics: Datasets preparing and applications. In: Zhao, C., Wu, Y., Wang, J., Liu, Q. (eds.) *Proceedings of the 2009 Second International Symposium on Knowledge Acquisition and Modeling*, vol. 2, pp. 189-192. Wuhan, China, Nov. 30-Dec. 1 (2009)
87. Nowers, J.R., Broderick, S.R., Rajan, K., Narasimhan, B.: Combinatorial methods and informatics provide insight into physical properties and structure relationships during IPN formation. *Macromol. Rapid Commun.* **28**, 972-976 (2007)
88. George, L., Hrubciak, R., Rajan, K., Saxena, S.K.: Principal component analysis on properties of binary and ternary hydrides and a comparison of metal versus metal hydride properties. *J. Alloy. Compd.* **478**, 731-735 (2009)
89. Hautier, G., Fischer, C., Ehlacher, V., Jain, A., Ceder, G.: Data mined ionic substitutions for the discovery of new compounds. *Inorg. Chem.* **50**, 656-663 (2011)
90. Jolliffe, I.T.: *Principal Component Analysis*, 2nd edn. Springer, New York (2002)
91. Chong, I.G., Jun, C.H.: Performance of some variable selection methods when multicollinearity is present. *Chemom. Intell. Lab. Syst.* **78**, 103-112 (2005)
92. Bucholz, E.W., Phillpot, S.R., Sinnott, S.B.: Molecular dynamics investigation of the lubrication mechanism of carbon nano-onions. *Comput. Mater. Sci.* **54**, 91-96 (2012)
93. Kroto, H.W., Heath, J.R., O'Brien, S.C., Curl, R.F., Smalley, R.E.: C<sub>60</sub>: Buckminsterfullerene. *Nature* **318**, 162-163 (1985)
94. Iijima, S.: Helical microtubules of graphitic carbon. *Nature* **354**, 56-58 (1991)
95. Kuznetsov, V.L., Chuvilin, A.L., Butenko, Y.V., Malkov, I.Y., Titov, V.M.: Onion-like carbon from ultra-disperse diamond. *Chem. Phys. Lett.* **222**, 343-348 (1994)
96. Tenne, R.: Inorganic nanotubes and fullerene-like nanoparticles. *Nat. Nanotechnol.* **1**, 103-111 (2006)
97. Hirano, M., Shinjo, K.: Superlubricity and frictional anisotropy. *Wear* **168**, 121-125 (1993)
98. Kim, H.J., Kim, D.E.: Nano-scale friction: A review. *Int. J. Precis. Eng. Manuf.* **10**, 141-151 (2009)

99. Onodera, T., Morita, Y., Suzuki, A., Koyama, M., Tsuboi, H., Hatakeyama, N., Endou, A., Takaba, H., Kubo, M., Dassenoy, F., Minfray, C., Joly-Pottuz, L., Martin, J.M., Miyamoto, A.: A computational chemistry study on friction of h-MoS<sub>2</sub>. Part I. Mechanism of single sheet lubrication. *J. Phys. Chem. B* **113**, 16526-16536 (2009)
100. Liang, T., Sawyer, W.G., Perry, S.S., Sinnott, S.B., Phillpot, S.R.: First-principles determination of static potential energy surfaces for atomic friction in MoS<sub>2</sub> and MoO<sub>3</sub>. *Phys. Rev. B* **77**, 104105 (2008)
101. Grossiord, C., Martin, J.M., Varlot, K., Vacher, B., Le Mogne, T., Yamada, Y.: Tribochemical interactions between Znntp, Modtc and calcium borate. *Tribol. Lett.* **8**, 203-212 (2000)
102. Miura, K., Tsuda, D., Itamura, N., Sasaki, N.: Superlubricity of fullerene intercalated graphite composite. *Jpn. J. Appl. Phys.* **46**, 5269-5274 (2007)
103. Joly-Pottuz, L., Vacher, B., Ohmae, N., Martin, J.M., Epicier, T.: Anti-wear and friction reducing mechanisms of carbon nano-onions as lubricant additives. *Tribol. Lett.* **30**, 69-80 (2008)
104. Joly-Pottuz, L., Bucholz, E.W., Matsumoto, N., Phillpot, S.R., Sinnott, S.B., Ohmae, N., Martin, J.M.: Friction properties of carbon nano-onions from experiment and computer simulations. *Tribol. Lett.* **37**, 75-81 (2010)
105. Pastewka, L., Pou, P., Perez, R., Gumbsch, P., Moseler, M.: Describing bond-breaking processes by reactive potentials: Importance of an environment-dependent interaction range. *Phys. Rev. B* **78**, 161402 (2008)
106. Stuart, S.J., Tutein, A.B., Harrison, J.A.: A reactive potential for hydrocarbons with intermolecular interactions. *J. Chem. Phys.* **112**, 6472-6486 (2000)
107. Kuznetsov, V.L., Zilberberg, I.L., Butenko, Y.V., Chuvilin, A.L., Segall, B.: Theoretical study of the formation of closed curved graphite-like structures during annealing of diamond surface. *J. Appl. Phys.* **86**, 863-870 (1999)
108. Tomita, S., Sakurai, T., Ohta, H., Fujii, M., Hayashi, S.: Structure and electronic properties of carbon onions. *J. Chem. Phys.* **114**, 7477-7482 (2001)
109. Smith, E.D., Robbins, M.O., Cieplak, M.: Friction on adsorbed monolayers. *Phys. Rev. B* **54**, 8252-8260 (1996)
110. Guo, H.B., Qi, Y.: Environmental conditions to achieve low adhesion and low friction on diamond surfaces. *Model. Simul. Mater. Sci. Eng.* **18**, 034008 (2010)
111. Gao, G.T., Mikulski, P.T., Chateauneuf, G.M., Harrison, J.A.: The effects of film structure and surface hydrogen on the properties of amorphous carbon films. *J. Phys. Chem. B* **107**, 11082-11090 (2003)

112. Falvo, M.R., Taylor, R.M., Helser, A., Chi, V., Brooks, F.P., Washburn, S., Superfine, R.: Nanometre-scale rolling and sliding of carbon nanotubes. *Nature* **397**, 236-238 (1999)
113. Falvo, M.R., Steele, J., Taylor, R.M., Superfine, R.: Gearlike rolling motion mediated by commensurate contact: Carbon nanotubes on HOPG. *Phys. Rev. B* **62**, 10665-10667 (2000)
114. Schall, J.D., Brenner, D.W.: Molecular dynamics simulations of carbon nanotube rolling and sliding on graphite. *Mol. Simul.* **25**, 73-79 (2000)
115. Sasaki, N., Itamura, N., Miura, K.: Simulation of atomic-scale ultralow friction of graphite/C<sub>60</sub>/graphite interface along [10 $\bar{1}$ 0] direction. *Jpn. J. Appl. Phys.* **46**, L1237-L1239 (2007)
116. Kang, J.W., Hwang, H.J.: Fullerene nano ball bearings: An atomistic study. *Nanotechnol.* **15**, 614-621 (2004)
117. Robertson, J.: Amorphous carbon. *Adv. Phys.* **35**, 317-374 (1986)
118. Grill, A.: Tribology of diamondlike carbon and related materials: An updated review. *Surf. Coat. Technol.* **94**, 507-513 (1997)
119. Erdemir, A., Donnet, C.: Tribology of diamond-like carbon films: Recent progress and future prospects. *J. Phys. D: Appl. Phys.* **39**, R311-R327 (2006)
120. Charitidis, C.A.: Nanomechanical and nanotribological properties of carbon-based thin films: A review. *Int. J. Refract. Met. Hard Mater.* **28**, 51-70 (2010)
121. Robertson, J.: Diamond-like amorphous carbon. *Mater. Sci. Eng. R* **37**, 129-281 (2002)
122. Ferrari, A.C., Robertson, J.: Interpretation of Raman spectra of disordered and amorphous carbon. *Phys. Rev. B* **61**, 14095-14107 (2000)
123. Lifshitz, Y.: Hydrogen-free amorphous carbon films: Correlation between growth conditions and properties. *Diam. Relat. Mater.* **5**, 388-400 (1996)
124. Sinnott, S.B., Colton, R.J., White, C.T., Shenderova, O.A., Brenner, D.W., Harrison, J.A.: Atomistic simulations of the nanometer-scale indentation of amorphous-carbon thin films. *J. Vac. Sci. Technol. A* **15**, 936-940 (1997)
125. Ferrari, A.C., Robertson, J., Beghi, M.G., Bottani, C.E., Ferulano, R., Pastorelli, R.: Elastic constants of tetrahedral amorphous carbon films by surface Brillouin scattering. *Appl. Phys. Lett.* **75**, 1893-1895 (1999)

126. Ronkainen, H., Varjus, S., Koskinen, J., Holmberg, K.: Differentiating the tribological performance of hydrogenated and hydrogen-free DLC coatings. *Wear* **249**, 260-266 (2001)
127. Miyoshi, K., Street, K.W., Vander Wal, R.L., Andrews, R., Sayir, A.: Solid lubrication by multiwalled carbon nanotubes in air and in vacuum. *Tribol. Lett.* **19**, 191-201 (2005)
128. Rapoport, L., Fleischer, N., Tenne, R.: Applications of WS<sub>2</sub> (MoS<sub>2</sub>) inorganic nanotubes and fullerene-like nanoparticles for solid lubrication and for structural nanocomposites. *J. Mater. Chem.* **15**, 1782-1788 (2005)
129. Joly-Pottuz, L., Dassenoy, F., Belin, M., Vacher, B., Martin, J.M., Fleischer, N.: Ultralow-friction and wear properties of IF-WS<sub>2</sub> under boundary lubrication. *Tribol. Lett.* **18**, 477-485 (2005)
130. Lu, J.P.: Elastic properties of carbon nanotubes and nanoropes. *Phys. Rev. Lett.* **79**, 1297-1300 (1997)
131. Tenne, R., Margulis, L., Genut, M., Hodes, G.: Polyhedral and cylindrical structures of tungsten disulfide. *Nature* **360**, 444-446 (1992)
132. Tannous, J., Dassenoy, F., Bruhacs, A., Tremel, W.: Synthesis and tribological performance of novel Mo<sub>x</sub>W<sub>1-x</sub>S<sub>2</sub> (0 ≤ x ≤ 1) inorganic fullerenes. *Tribol. Lett.* **37**, 83-92 (2010)
133. Rapoport, L., Nepomnyashchy, O., Lapsker, I., Verdyan, A., Moshkovich, A., Feldman, Y., Tenne, R.: Behavior of fullerene-like WS<sub>2</sub> nanoparticles under severe contact conditions. *Wear* **259**, 703-707 (2005)
134. Tannous, J., Dassenoy, F., Lahouij, I., Le Mogne, T., Vacher, B., Bruhacs, A., Tremel, W.: Understanding the tribochemical mechanisms of IF-MoS<sub>2</sub> nanoparticles under boundary lubrication. *Tribol. Lett.* **41**, 55-64 (2011)
135. Rosentsveig, R., Gorodnev, A., Feuerstein, N., Friedman, H., Zak, A., Fleischer, N., Tannous, J., Dassenoy, F., Tenne, R.: Fullerene-like MoS<sub>2</sub> nanoparticles and their tribological behavior. *Tribol. Lett.* **36**, 175-182 (2009)
136. Lahouij, I., Dassenoy, F., de Knoop, L., Martin, J.M., Vacher, B.: In situ TEM observation of the behavior of an individual fullerene-like MoS<sub>2</sub> nanoparticle in a dynamic contact. *Tribol. Lett.* **42**, 133-140 (2011)
137. Feldman, J.L.: Elastic constants of 2H-MoS<sub>2</sub> and 2H-NbSe<sub>2</sub> extracted from measured dispersion curves and linear compressibilities. *J. Phys. Chem. Solids* **37**, 1141-1144 (1976)
138. Schwarz, U.S., Komura, S., Safran, S.A.: Deformation and tribology of multi-walled hollow nanoparticles. *Europhys. Lett.* **50**, 762-768 (2000)

139. Tevet, O., Von-Huth, P., Popovitz-Biro, R., Rosentsveig, R., Wagner, H.D., Tenne, R.: Friction mechanism of individual multilayered nanoparticles. *Proc. Natl. Acad. Sci. U.S.A.* **108**, 19901-19906 (2011)
140. Winer, W.O.: Molybdenum disulfide as a lubricant: A review of the fundamental knowledge. *Wear* **10**, 422-452 (1967)
141. Hirvonen, J.P., Koskinen, J., Jervis, J.R., Nastasi, M.: Present progress in the development of low friction coatings. *Surf. Coat. Technol.* **80**, 139-150 (1996)
142. Savan, A., Pflüger, E., Voumard, P., Schröer, A., Simmonds, M.: Modern solid lubrication: Recent developments and applications of MoS<sub>2</sub>. *Lubr. Sci.* **12**, 185-203 (2000)
143. Burris, D.L., Perry, S.S., Sawyer, W.G.: Macroscopic evidence of thermally activated friction with polytetrafluoroethylene. *Tribol. Lett.* **27**, 323-328 (2007)
144. Schirmeisen, A., Jansen, L., Holscher, H., Fuchs, H.: Temperature dependence of point contact friction on silicon. *Appl. Phys. Lett.* **88**, 123108 (2006)
145. Zhao, X.Y., Hamilton, M., Sawyer, W.G., Perry, S.S.: Thermally activated friction. *Tribol. Lett.* **27**, 113-117 (2007)
146. Zhao, X.Y., Phillpot, S.R., Sawyer, W.G., Sinnott, S.B., Perry, S.S.: Transition from thermal to athermal friction under cryogenic conditions. *Phys. Rev. Lett.* **102**, 186102 (2009)
147. Srivastava, D., Wei, C., Cho, K.: Nanomechanics of carbon nanotubes and composites. *Appl. Mech. Rev.* **56**, 215-230 (2003)
148. Dresselhaus, M.S., Dresselhaus, G., Charlier, J.C., Hernandez, E.: Electronic, thermal and mechanical properties of carbon nanotubes. *Phil. Trans. R. Soc. Lond. A* **362**, 2065-2098 (2004)
149. Wang, C.M., Zhang, Y.Y., Xiang, Y., Reddy, J.N.: Recent studies on buckling of carbon nanotubes. *Appl. Mech. Rev.* **63** (2010)
150. Margulis, L., Salitra, G., Tenne, R., Talianker, M.: Nested fullerene-like structures. *Nature* **365**, 113-114 (1993)
151. Remskar, M., Skraba, Z., Cleton, F., Sanjines, R., Levy, F.: MoS<sub>2</sub> as microtubes. *Appl. Phys. Lett.* **69**, 351-353 (1996)
152. Rothschild, A., Cohen, S.R., Tenne, R.: WS<sub>2</sub> nanotubes as tips in scanning probe microscopy. *Appl. Phys. Lett.* **75**, 4025-4027 (1999)

153. Kaplan-Ashiri, I., Cohen, S.R., Gartsman, K., Ivanovskaya, V., Heine, T., Seifert, G., Wiesel, I., Wagner, H.D., Tenne, R.: On the mechanical behavior of WS<sub>2</sub> nanotubes under axial tension and compression. *Proc. Natl. Acad. Sci. U.S.A.* **103**, 523-528 (2006)
154. Seifert, G., Terrones, H., Terrones, M., Jungnickel, G., Frauenheim, T.: Structure and electronic properties of MoS<sub>2</sub> nanotubes. *Phys. Rev. Lett.* **85**, 146-149 (2000)
155. Kaplan-Ashiri, I., Cohen, S.R., Gartsman, K., Rosentsveig, R., Seifert, G., Tenne, R.: Mechanical behavior of individual WS<sub>2</sub> nanotubes. *J. Mater. Res.* **19**, 454-459 (2004)
156. Kaplan-Ashiri, I., Cohen, S.R., Apter, N., Wang, Y.K., Seifert, G., Wagner, H.D., Tenne, R.: Microscopic investigation of shear in multiwalled nanotube deformation. *J. Phys. Chem. C* **111**, 8432-8436 (2007)
157. Zhang, D.B., Dumitrica, T., Seifert, G.: Helical nanotube structures of MoS<sub>2</sub> with intrinsic twisting: An objective molecular dynamics study. *Phys. Rev. Lett.* **104**, 065502 (2010)
158. Heo, S., Sinnott, S.B.: Investigation of the influence of thermostat configurations on the mechanical properties of carbon nanotubes in molecular dynamics simulations. *J. Nanosci. Nanotechnol.* **7**, 1518-1524 (2007)
159. Belytschko, T., Xiao, S.P., Schatz, G.C., Ruoff, R.S.: Atomistic simulations of nanotube fracture. *Phys. Rev. B* **65**, 235430 (2002)
160. Sammalkorpi, M., Krasheninnikov, A., Kuronen, A., Nordlund, K., Kaski, K.: Mechanical properties of carbon nanotubes with vacancies and related defects. *Phys. Rev. B* **70**, 245416 (2004)
161. Zhang, S.L., Mielke, S.L., Khare, R., Troya, D., Ruoff, R.S., Schatz, G.C., Belytschko, T.: Mechanics of defects in carbon nanotubes: Atomistic and multiscale simulations. *Phys. Rev. B* **71**, 115403 (2005)
162. Feliciano, J., Tang, C., Zhang, Y.Y., Chen, C.F.: Aspect ratio dependent buckling mode transition in single-walled carbon nanotubes under compression. *J. Appl. Phys.* **109** (2011)
163. Ansari, R., Rouhi, S.: Atomistic finite element model for axial buckling of single-walled carbon nanotubes. *Physica E* **43**, 58-69 (2010)
164. Bucholz, E.W., Zhao, X.Y., Sinnott, S.B., Perry, S.S.: Friction and wear of pyrophyllite on the atomic scale. *Tribol. Lett.* **46**, 159-165 (2012)

165. Sainz-Diaz, C.I., Timon, V., Botella, V., Artacho, E., Hernandez-Laguna, A.: Quantum mechanical calculations of dioctahedral 2:1 phyllosilicates: Effect of octahedral cation distributions in pyrophyllite, illite, and smectite. *Am. Miner.* **87**, 958-965 (2002)
166. Sainz-Diaz, C.I., Hernandez-Laguna, A., Dove, M.T.: Modeling of dioctahedral 2:1 phyllosilicates by means of transferable empirical potentials. *Phys. Chem. Miner.* **28**, 130-141 (2001)
167. Zartman, G.D., Liu, H., Akdim, B., Pachter, R., Heinz, H.: Nanoscale tensile, shear, and failure properties of layered silicates as a function of cation density and stress. *J. Phys. Chem. C* **114**, 1763-1772 (2010)
168. Bonewitz, R.L.: *Rock and Gem*. DK Publishing, Inc., New York (2005)
169. Moore, D.E., Lockner, D.A.: Crystallographic controls on the frictional behavior of dry and water-saturated sheet structure minerals. *J. Geophys. Res.* **109**, B03401 (2004)
170. Lee, J.H., Guggenheim, S.: Single crystal x-ray refinement of pyrophyllite-1Tc. *Am. Miner.* **66**, 350-357 (1981)
171. Bentayeb, A., Amouric, A., Olives, J., Dekayir, A., Nadiri, A.: XRD and HRTEM characterization of pyrophyllite from Morocco and its possible applications. *Appl. Clay Sci.* **22**, 211-221 (2003)
172. Ikari, M.J., Saffer, D.M., Marone, C.: Effect of hydration state on the frictional properties of montmorillonite-based fault gouge. *J. Geophys. Res.* **112**, B06423 (2007)
173. Collettini, C., Niemeijer, A., Viti, C., Marone, C.: Fault zone fabric and fault weakness. *Nature* **462**, 907-910 (2009)
174. Carpenter, B.M., Marone, C., Saffer, D.M.: Frictional behavior of materials in the 3D SAFOD volume. *Geophys. Res. Lett.* **36**, L05302 (2009)
175. Moore, D.E., Lockner, D.A.: Talc friction in the temperature range 25°-400°C: Relevance for fault-zone weakening. *Tectonophys.* **449**, 120-132 (2008)
176. Prasad, B.K.: Lubricated sliding wear behavior of a cast iron: Effect of graphite and/or talc fraction in oil. *J. Mater. Eng. Perform.* **19**, 413-420 (2010)
177. Prasad, B.K., Rathod, S., Modi, O.P., Yadav, M.S.: Influence of talc concentration in oil lubricant on the wear response of a bronze journal bearing. *Wear* **269**, 498-505 (2010)

178. Martinez-Martinez, D., Kolodziejczyk, L., Sanchez-Lopez, J.C., Fernandez, A.: Tribological carbon-based coatings: An AFM and LFM study. *Surf. Sci.* **603**, 973-979 (2009)
179. Tamura, H., Tsujimichi, K., Yamano, H., Shiota, K., Kubo, M., Fahmi, A., Miyamoto, A.: Molecular dynamics simulation of the friction between talc (001) surfaces. *Appl. Surf. Sci.* **119**, 335-340 (1997)
180. Hirano, M., Shinjo, K., Kaneko, R., Murata, Y.: Anisotropy of frictional forces in muscovite mica. *Phys. Rev. Lett.* **67**, 2642-2645 (1991)
181. Derjaguin, B.V., Muller, V.M., Toporov, Y.P.: Effect of contact deformations on adhesion of particles. *J. Colloid Interface Sci.* **53**, 314-326 (1975)
182. Zhang, G.P., Wei, Z.X., Ferrell, R.E., Guggenheim, S., Cygan, R.T., Luo, J.: Evaluation of the elasticity normal to the basal plane of non-expandable 2:1 phyllosilicate minerals by nanoindentation. *Am. Miner.* **95**, 863-869 (2010)
183. Blakslee, O.L., Proctor, D.G., Seldin, E.J., Spence, G.B., Weng, T.: Elastic constants of compression-annealed pyrolytic graphite. *J. Appl. Phys.* **41**, 3373-3382 (1970)
184. Khan, A., Philip, J., Hess, P.: Young's modulus of silicon nitride used in scanning force microscope cantilevers. *J. Appl. Phys.* **95**, 1667-1672 (2004)
185. Binnig, G., Fuchs, H., Gerber, C., Rohrer, H., Stoll, E., Tosatti, E.: Energy-dependent state-density corrugation of a graphite surface as seen by scanning tunneling microscopy. *Europhys. Lett.* **1**, 31-36 (1986)
186. Park, S.I., Quate, C.F.: Tunneling microscopy of graphite in air. *Appl. Phys. Lett.* **48**, 112-114 (1986)
187. Meyer, E., Heinzemann, H., Grutter, P., Jung, T., Weisskopf, T., Hidber, H.R., Lapka, R., Rudin, H., Guntherodt, H.J.: Comparative study of lithium fluoride and graphite by atomic force microscopy (AFM). *J. Microsc.* **152**, 269-280 (1988)
188. Chang, H.P., Bard, A.J.: Observation and characterization by scanning tunneling microscopy of structures generated by cleaving highly oriented pyrolytic graphite. *Langmuir* **7**, 1143-1153 (1991)
189. Arias, D.F., Marulanda, D.M., Baena, A.M., Devia, A.: Determination of friction coefficient on ZrN and TiN using lateral force microscopy (LFM). *Wear* **261**, 1232-1236 (2006)
190. Buzio, R., Gnecco, E., Boragno, C., Valbusa, U.: Friction force microscopy investigation of nanostructured carbon films. *Carbon* **40**, 883-890 (2002)

191. Roselman, I.C., Tabor, D.: The friction of carbon fibres. *J. Phys. D: Appl. Phys.* **9**, 2517-2532 (1976)
192. Singer, I.L., Bolster, R.N., Wegand, J., Fayeulle, S., Stupp, B.C.: Hertzian stress contribution to low friction behavior of thin MoS<sub>2</sub> coatings. *Appl. Phys. Lett.* **57**, 995-997 (1990)
193. Stoyanov, P., Chromik, R.R., Goldbaum, D., Lince, J.R., Zhang, X.L.: Microtribological performance of Au-MoS<sub>2</sub> and Ti-MoS<sub>2</sub> coatings with varying contact pressure. *Tribol. Lett.* **40**, 199-211 (2010)
194. Grosseau-Poussard, J.L., Moine, P., Brendle, M.: Shear strength measurements of parallel MoS<sub>x</sub> thin films. *Thin Solid Films* **307**, 163-168 (1997)
195. Schiffmann, K.I.: Microfriction and macrofriction of metal containing amorphous hydrocarbon hard coatings determined by AFM and pin-on-disk tests. *Tribol. Lett.* **5**, 109-116 (1998)
196. Childs, T.H.C.: Deformation and flow of metals in sliding friction. In: Singer, I.L., Pollock, H.M. (eds.) *Fundamentals of Friction: Macroscopic and Microscopic Processes*, pp. 209-225. Kluwer Academic Publishers, Dordrecht (1992)
197. Johnson, K.L.: The contribution of micro/nano-tribology to the interpretation of dry friction. *Proc. Inst. Mech. Eng. Part C* **214**, 11-22 (2000)
198. Krim, J.: Friction at the atomic scale. *Sci. Am.* **275**, 74-80 (1996)
199. Gosvami, N.N., Filleter, T., Egberts, P., Bennewitz, R.: Microscopic friction studies on metal surfaces. *Tribol. Lett.* **39**, 19-24 (2010)
200. Robertson, E.C.: Experimental study of the strength of rocks. *Geol. Soc. Am. Bull.* **66**, 1275-1314 (1955)
201. Bucholz, E.W., Kong, C.S., Marchman, K.R., Sawyer, W.G., Phillpot, S.R., Sinnott, S.B., Rajan, K.: Data-driven model for estimation of friction coefficient via informatics methods. *Tribol. Lett.* **47**, 211-221 (2012)
202. Ludema, K.C.: Mechanism-based modeling of friction and wear. *Wear* **200**, 1-7 (1996)
203. Luengo, G., Campbell, S.E., Srdanov, V.I., Wudl, F., Israelachvili, J.N.: Direct measurement of the adhesion and friction of smooth C<sub>60</sub> surfaces. *Chem. Mater.* **9**, 1166-1171 (1997)
204. Maeda, N., Chen, N.H., Tirrell, M., Israelachvili, J.N.: Adhesion and friction mechanisms of polymer-on-polymer surfaces. *Science* **297**, 379-382 (2002)

205. Kopta, S., Salmeron, M.: The atomic scale origin of wear on mica and its contribution to friction. *J. Chem. Phys.* **113**, 8249-8252 (2000)
206. van den Oetelaar, R.J.A., Flipse, C.F.J.: Atomic-scale friction on diamond(111) studied by ultra-high vacuum atomic force microscopy. *Surf. Sci.* **384**, L828-L835 (1997)
207. Sanchez-Lopez, J.C., Donnet, C., Loubet, J.L., Belin, M., Grill, A., Patel, V., Jahnes, C.: Tribological and mechanical properties of diamond-like carbon prepared by high-density plasma. *Diam. Relat. Mater.* **10**, 1063-1069 (2001)
208. Polcar, T., Novak, R., Siroky, P.: The tribological characteristics of TiCN coating at elevated temperatures. *Wear* **260**, 40-49 (2006)
209. Zhong, W., Tomanek, D.: First-principles theory of atomic-scale friction. *Phys. Rev. Lett.* **64**, 3054-3057 (1990)
210. Erdemir, A.: A crystal-chemical approach to lubrication by solid oxides. *Tribol. Lett.* **8**, 97-102 (2000)
211. Erdemir, A., Li, S.H., Jin, Y.S.: Relation of certain quantum chemical parameters to lubrication behavior of solid oxides. *Int. J. Mol. Sci.* **6**, 203-218 (2005)
212. Callister, W.D.: *Materials Science and Engineering: An Introduction*, 6th edn. John Wiley & Sons, Inc., New York (2003)
213. Gale, J.D., Rohlf, A.L.: The general utility lattice program (GULP). *Mol. Simul.* **29**, 291-341 (2003)
214. Glasser, L.: Solid-state energetics and electrostatics: Madelung constants and Madelung energies. *Inorg. Chem.* **51**, 2420-2424 (2012)
215. Refaeilzadeh, P., Tang, L., Liu, H.: Cross-validation. In: Liu, L., Ozsu, M.T. (eds.) *Encyclopedia of Database Systems*, pp. 532-538. Springer, New York (2009)
216. Horn, H.M., Deere, D.U.: Frictional characteristics of minerals. *Geotech.* **12**, 319-335 (1962)
217. Woydt, M., Habig, K.H.: High temperature tribology of ceramics. *Tribol. Int.* **22**, 75-88 (1989)
218. Goto, M., Kasahara, A., Tosa, M.: Low frictional property of copper oxide thin films optimised using a combinatorial sputter coating system. *Appl. Surf. Sci.* **252**, 2482-2487 (2006)
219. Anthony, J.W., Bideaux, R.A., Bladh, K.W., Nichols, M.C.: *Handbook of Mineralogy, Volume III: Halides, Hydroxides, Oxides*. Mineral Data Publishing, Tucson (1997)

220. Ralph, J., Chau, I.: Molybdate. <http://www.mindat.org/min-2748.html> (2011). Accessed 23 January 2012
221. Ralph, J., Chau, I.: Shcherbinaite. <http://www.mindat.org/min-3636.html> (2011). Accessed 23 January 2012
222. Prasad, S.V., McDevitt, N.T., Zabinski, J.S.: Tribology of tungsten disulfide films in humid environments: The role of a tailored metal-matrix composite substrate. *Wear* **230**, 24-34 (1999)
223. Anthony, J.W., Bideaux, R.A., Bladh, K.W., Nichols, M.C.: Handbook of Mineralogy, Volume I: Elements, Sulfides, Sulfosalts. Mineral Data Publishing, Tucson (1990)
224. Physical and optical properties of minerals. In: Haynes, W.M. (ed.) CRC Handbook of Chemistry and Physics, 92nd edn, pp. 4-138-144. CRC Press/Taylor and Francis, Boca Raton (2011)
225. Gersten, J.I., Smith, F.W.: The Physics and Chemistry of Materials. John Wiley & Sons, Inc., New York (2001)
226. Kubart, T., Polcar, T., Kopecky, L., Novak, R., Novakova, D.: Temperature dependence of tribological properties of MoS<sub>2</sub> and MoSe<sub>2</sub> coatings. *Surf. Coat. Technol.* **193**, 230-233 (2005)
227. Ralph, J., Chau, I.: Drysdallite. <http://www.mindat.org/min-1322.html> (2011). Accessed 23 January 2012
228. Erdemir, A.: Crystal chemistry and solid lubricating properties of the monochalcogenides gallium selenide and tin selenide. *Tribol. Trans.* **37**, 471-478 (1994)
229. Gurzadyan, G., Tzankov, P.: Dielectrics and electrooptics. In: Martienssen, W., Warlimont, H. (eds.) Springer Handbook of Condensed Matter and Materials Data, pp. 817-901. Springer, Berlin (2005)
230. Ralph, J., Chau, I.: Frebaldite. <http://www.mindat.org/min-1602.html> (2011). Accessed 23 January 2012
231. Lewis, R.J.: Sax's Dangerous Properties of Industrial Materials, vol. 3, 11th edn. John Wiley & Sons, Inc., Hoboken (2004)
232. Aylward, G.H., Findlay, T.J.V.: SI Chemical Data. John Wiley & Sons, Inc., New York (1971)
233. Physical constants of inorganic compounds. In: Haynes, W.M. (ed.) CRC Handbook of Chemistry and Physics, 92nd edn, pp. 4-43-101. CRC Press/Taylor and Francis, Boca Raton (2011)

234. Properties of semiconductors. In: Haynes, W.M. (ed.) CRC Handbook of Chemistry and Physics, 92nd edn, pp. 12-80-93. CRC Press/Taylor and Francis, Boca Raton (2011)
235. Dierks, S.: Nickel telluride: Material safety data sheet. <http://www.espimetals.com/index.php/msds/696-nickel-telluride> (1999). Accessed 23 January 2012
236. Makovetskii, G.I., Vas'kov, D.G., Yanushkevich, K.I.: Structure, density, and microhardness of  $\text{Co}_{1-x}\text{Ni}_x\text{Te}$  ( $0 < x < 1$ ) solid solutions. *Inorg. Mater.* **38**, 108-110 (2002)
237. Hikichi, Y., Ota, T., Daimon, K., Hattori, T., Mizuno, M.: Thermal, mechanical, and chemical properties of sintered xenotime-type  $\text{RPO}_4$  ( $\text{R} = \text{Y}, \text{Er}, \text{Yb}, \text{or Lu}$ ). *J. Am. Ceram. Soc.* **81**, 2216-2218 (1998)

## BIOGRAPHICAL SKETCH

Eric Bucholz was born in 1985 in Greenville, SC. After graduating in the top 10 of his class from Mauldin High School in June 2003, he began his undergraduate studies in the Department of Materials Science and Engineering at Clemson University in Clemson, SC, where he was the recipient of both the Keramos Outstanding Rising Junior Award in May 2005 and the Gilbert Robinson Research Award in May 2006. He received his B.S. in ceramic and materials engineering from Clemson University in May 2007. He started his study for Ph.D. in the Department of Materials Science and Engineering at the University of Florida in August 2007 where he joined the Computational Materials Science Focus Group with Prof. Susan B. Sinnott. His research interests during this time were focused on the mechanical and frictional behaviors of different materials, particularly nanomaterials, from both computational and experimental perspectives. During his doctoral studies, he received his M.S. in materials science and engineering in December 2009, was awarded second place in the materials science poster competition at the 2010 Annual Joint Symposium of the Florida Chapter of the American Vacuum Society and the Florida Society for Microscopy, and was the third place finalist in the Applied Surface Science Division student competition at the American Vacuum Society's 58<sup>th</sup> International Symposium and Exhibition in 2011. He was also a recipient of an international research fellowship from the International Center for Materials Research in 2010 which afforded him the opportunity to spend one month at École Central de Lyon and INSA in Lyon, France, where he was both embedded in French culture and able to perform advanced *in situ* TEM experiments probing the mechanical and tribological responses of individual nanoparticles. In August 2012, he received his Ph.D. in materials science and engineering from the University of Florida.